



National Library  
of Canada

Acquisitions and  
Bibliographic Services Branch

395 Wellington Street  
Ottawa, Ontario  
K1A 0N4

Bibliothèque nationale  
du Canada

Direction des acquisitions et  
des services bibliographiques

395, rue Wellington  
Ottawa (Ontario)  
K1A 0N4

Your library's reference

ou de votre bibliothèque

## NOTICE

The quality of this microform is heavily dependent upon the quality of the original thesis submitted for microfilming. Every effort has been made to ensure the highest quality of reproduction possible.

If pages are missing, contact the university which granted the degree.

Some pages may have indistinct print especially if the original pages were typed with a poor typewriter ribbon or if the university sent us an inferior photocopy.

Reproduction in full or in part of this microform is governed by the Canadian Copyright Act, R.S.C. 1970, c. C-30, and subsequent amendments.

## AVIS

La qualité de cette microforme dépend grandement de la qualité de la thèse soumise au microfilmage. Nous avons tout fait pour assurer une qualité supérieure de reproduction.

S'il manque des pages, veuillez communiquer avec l'université qui a conféré le grade.

La qualité d'impression de certaines pages peut laisser à désirer, surtout si les pages originales ont été dactylographiées à l'aide d'un ruban usé ou si l'université nous a fait parvenir une photocopie de qualité inférieure.

La reproduction, même partielle, de cette microforme est soumise à la Loi canadienne sur le droit d'auteur, SRC 1970, c. C-30, et ses amendements subséquents.

Canada

UNIVERSITY OF ALBERTA

**A THEORETICAL AND EXPERIMENTAL  
STUDY OF MICROMACHINED V-GROOVE  
WAVEGUIDES**

BY

**KWOK-SING CHENG**



**A thesis submitted to the Faculty of Graduate Studies and Research in partial  
fulfilment of the requirements for the degree of MASTER OF SCIENCE.**

**DEPARTMENT OF ELECTRICAL ENGINEERING**

**EDMONTON, ALBERTA**

**SPRING 1996**



National Library  
of Canada

Acquisitions and  
Bibliographic Services Branch

395 Wellington Street  
Ottawa, Ontario  
K1A 0N4

Bibliothèque nationale  
du Canada

Direction des acquisitions et  
des services bibliographiques

395, rue Wellington  
Ottawa (Ontario)  
K1A 0N4

*Your file* *Votre référence*

*Our file* *Notre référence*

**The author has granted an irrevocable non-exclusive licence allowing the National Library of Canada to reproduce, loan, distribute or sell copies of his/her thesis by any means and in any form or format, making this thesis available to interested persons.**

**L'auteur a accordé une licence irrévocable et non exclusive permettant à la Bibliothèque nationale du Canada de reproduire, prêter, distribuer ou vendre des copies de sa thèse de quelque manière et sous quelque forme que ce soit pour mettre des exemplaires de cette thèse à la disposition des personnes intéressées.**

**The author retains ownership of the copyright in his/her thesis. Neither the thesis nor substantial extracts from it may be printed or otherwise reproduced without his/her permission.**

**L'auteur conserve la propriété du droit d'auteur qui protège sa thèse. Ni la thèse ni des extraits substantiels de celle-ci ne doivent être imprimés ou autrement reproduits sans son autorisation.**

ISBN 0-612-10697-7

**Canada**

University of Alberta

Library Release Form

NAME OF AUTHOR: **KWOK-SING CHENG**

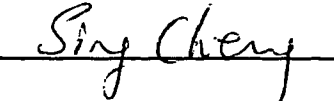
TITLE OF THESIS: **A THEORETICAL AND EXPERIMENTAL  
STUDY OF MICROMACHINED V-  
GROOVE WAVEGUIDES**

DEGREE: **MASTER OF SCIENCE**

YEAR THIS DEGREE GRANTED: **1996**

Permission is hereby granted to the University of Alberta Library to reproduce single copies of this thesis and to lend or sell such copies for private, scholarly or scientific research purposes only.

The author reserves all other publication and other rights in association with the copyright in the thesis, and except as hereinbefore provided neither the thesis nor any substantial portion thereof may be printed or otherwise reproduced in any material form whatever without the author's prior written permission.



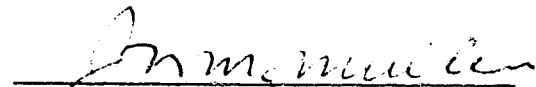
Kwok-sing Cheng  
7C, Block 4,  
Melody Garden,  
Tuen Mun, N. T.  
Hong Kong


Date: Jan 30<sup>th</sup> 1996


UNIVERSITY OF ALBERTA

FACULTY OF GRADUATE STUDIES AND RESEARCH

The undersigned certify that they have read, and recommend to the Faculty of Graduate Studies and Research for acceptance, a thesis entitled "**A THEORETICAL AND EXPERIMENTAL STUDY OF MICROMACHINED V-GROOVE WAVEGUIDES**" submitted by **KWOK-SING CHENG** in partial fulfilment of the requirements for the degree of **MASTER OF SCIENCE**.

  
\_\_\_\_\_  
Dr. J.N. McMullin, Supervisor

  
\_\_\_\_\_  
Dr. J. Conradi

  
\_\_\_\_\_  
Dr. K. Fyfe

Date: Jan. 30, 1996.

## **ABSTRACT**

**This thesis presents a theoretical and experimental study of micromachined v-groove waveguides. The theoretical study involves the calculations of singlemode sizes of several v-groove waveguides with different dielectric material compositions and the simulations of v-groove waveguide amplifiers. The experimental study involves fabrication of v-groove waveguides with polymer cores and the metallization of the end-facets of the waveguides. As well, the feasibility of integrating sidewall taps with singlemode v-groove waveguides was investigated.**

# Acknowledgments

I would like to express my sincere gratitude to my supervisor, Dr. J. N. McMullin, for his support and guidance throughout this project.

I thank the Telecommunications Research Laboratories (TRLabs) for their financial support and the use of their excellent research facilities.

I also thank the Alberta Microelectronics Centre (AMC) for providing all necessary fabrication equipments. The staffs in AMC provided a lot of technical help. In particular, I would like to give my appreciation to the following individuals for their assistance.

*Tran Tran*, for his assistance in operating many clean-room equipments and his instruction in photolithography.

*Yun Loke*, formerly of the AMC, for depositing the PECVD oxide and taking many SEM pictures.

*Dr. Jim Broughton*, for depositing the BPSG and conducting the reflow tests

*Glen Fitzpatrick*, for giving me a lot of technical advice.

I would like to extend my thanks to the members in the Hybrid Photonics Integrated Circuit (HyPIC) project for their support. In particular, I want to acknowledge the following individuals.

*Dr. Barry Keyworth*, for his help in setting up many different devices for optical measurements and providing a lot of valuable advice.

*Dino Corazza*, for his instruction in the polymer dispensing and his technical assistance.

*Madhu Krishnaswamy*, for his assistance in the waveguide measurement and the creation of the amplifier simulation program.

*Rajkumar Nagarajan*, for his assistance in e-beam writing and for his encouragement throughout this project

I would like to express my love and sincere gratitude to my parents for their support and care throughout the past many years. I would never forget their unceasing love and encouragement.

Lastly, I give thanks to the Lord, my God, who 'walked with me' throughout the entire project. "*The LORD is my shepherd; I shall not want.*" (Psalms 23:1, KJV)

## TABLE OF CONTENTS

<b>Chapter 1. Introduction</b>	<b>1</b>
1.1 Background and History of the V-groove waveguide	1
1.2 Other applications for the v-groove waveguide	9
1.3 Research scope	12
1.4 Thesis Outline	13
<b>Chapter 2. Mode Field Calculations using Finite Element Analysis</b>	<b>15</b>
2.1 Introduction	15
2.2 Background Theory for Modal Analysis	15
2.3 The mode-solving procedures	18
2.4 Analysis and Discussion of the SFEM Results.	22
2.4.1 The erbium-doped waveguide amplifier	22
2.4.2 Waveguides with polymer core	33
<b>Chapter 3. Optical Amplifier Simulations</b>	<b>38</b>
3.1 Background Theory for the Optical Amplifier	38
3.2 Brief Description of the Simulation	43
3.3 Simulation Results and Discussion	46
<b>Chapter 4. Fabrication of Polymer Waveguides and Sidewall Taps</b>	<b>56</b>
4.1 Introduction	56
4.2 V-groove waveguides with polymer cores	56
4.2.1 Introduction	56
4.2.2 Lower Cladding layer	58
4.2.3 Dispensed Polymer Core	67
4.2.4 RIE Polymer Core	74
4.3 Metallizing the waveguides for vertical coupling	84
4.4 Sidewall Taps	87
<b>Chapter 5. Conclusion</b>	<b>91</b>
5.1 Summary of Works	91
5.2 Future Work	94



**REFERENCES ..... 96**  
**APPENDIX A Description of the SFEM Program ..... 101**  
**APPENDIX B Amplifier Gain Simulation Program ..... 105**  
**APPENDIX C Procedures for etching V-grooves ..... 108**  
**APPENDIX D Borophosphorus Silicon Glass (BPSG) ..... 110**  
**APPENDIX E Procedures for Direct E-beam Writing ..... 111**

## LIST OF FIGURES

Fig. 1.1.1	Etching Process of a silicon V-groove . . . . .	4
Fig. 1.1.2	The formation of a sidewall tap . . . . .	7
Fig. 1.1.3	Two photolithography masks for making center tap . . . . .	8
Fig. 1.1.4	A center tap in the V-groove . . . . .	8
Fig. 1.2.1	Schematic diagram of a Optical Reader . . . . .	10
Fig. 1.2.2	Schematic diagram of flip-chip interconnections . . . . .	10
Fig. 1.2.3	Schematic Diagram of the V-groove Waveguide Amplifier . . . . .	12
Fig. 2.3.1	Diagram of the V-groove Waveguide Structure . . . . .	18
Fig. 2.3.2	Schematic diagrams of dividing V-groove Waveguide into Finite Elements . . . . .	20
Fig. 2.4.1.1	Intensity Contour Plots at 980 nm and 1550 nm . . . . .	23
Fig. 2.4.1.2	Confinement Factor versus Core Height. . . . .	26
Fig. 2.4.1.3	Intensity Contour Plot of 4 modes in 2 $\mu\text{m}$ core at the 980 nm pump wavelength. . . . .	27
Fig. 2.4.1.4	Confinement Factor versus $N_{\text{clad}}$ . . . . .	28
Fig. 2.4.1.5	Core Height and Conf. Factor versus Refractive Index of the Cladding Layer. . . . .	29
Fig. 2.4.1.6	Conf. Factor versus the ratio of Crescent depth to the Core Height. . . . .	30
Fig. 2.4.1.7	Different structures of the V-groove waveguide . . . . .	31
Fig. 2.4.1.8	Intensity contour plots of various waveguide configurations. . . . .	33
Fig. 2.4.2.1	Thin-film V-groove waveguide . . . . .	35
Fig. 2.4.2.2	Contour Plot of the fundamental mode of the polymer waveguide with upper cladding. . . . .	36
Fig. 2.4.2.3	Five different modes in a 2 $\mu\text{m}$ polymer waveguide without upper cladding. . . . .	37
Fig. 2.4.2.4	3 modes for the overflowed polymer waveguide . . . . .	37
Fig. 3.1.1	Four-level energy model for Optical Amplifier (the symbols in the parentheses corresponds to the variables in the equations that described the amplifier model) . . . . .	39
Fig. 3.2.1	Emission and Absorption cross-section spectra. . . . .	45
Fig. 3.3.1	Signal Gain versus Erbium Concentration at two pump levels. . . . .	47
Fig. 3.3.2	The Output spontaneous emission spectrum at $3 \times 10^{26}$ ions/ $\text{m}^3$ . . . . .	48
Fig. 3.3.3	Signal Gain versus propagating distance at two pump level. . . . .	49
Fig. 3.3.4	Signal and Pump powers and emission and absorption constants in a 4 cm waveguide . . . . .	50
Fig. 3.3.5	Signal Gain versus Pump power . . . . .	52
Fig. 3.3.6	Gain Profiles at different pump levels . . . . .	52
Fig. 3.3.7	Gain Efficiency versus Pump Power . . . . .	53
Fig. 3.3.8	Signal Gain versus Core Height . . . . .	54
Fig. 3.3.9	Signal Gain for three different waveguide structures . . . . .	55
Fig. 4.2.2.1	Fabrication procedures for making V-groove waveguide . . . . .	58
Fig. 4.2.2.2	SEM picture of the Silicon Oxinitride Cladding. . . . .	59
Fig. 4.2.2.3	SEM picture of the cladding layer after wet reflow at 950 $^{\circ}\text{C}$ . . . . .	61
Fig. 4.2.2.4	BPSG Cladding before reflow . . . . .	62

Fig. 4.2.2.5	SEM pictures of various reflow results. . . . .	.66
Fig. 4.2.3.1	Schematic Diagram of the Polymer Dispensing Set-up in TRLabs . . .	.68
Fig. 4.2.3.2	SEM picture of the cross section of the dispensed polymer waveguide.	70
Fig. 4.2.3.3	Optical picture of the dispensed polymer core . . . . .	.71
Fig. 4.2.3.4	Schematic Diagram of the set-up for capturing the output mode field.	.73
Fig. 4.2.3.5	Gray-Scale image of the output light from the waveguide. . . . .	.73
Fig. 4.2.4.1	SEM picture of the RIE polymer waveguide . . . . .	.76
Fig. 4.2.4.2	Gray-Scale Image and the corresponding contour plots of the output modes. . . . .	.77
Fig. 4.2.4.3	Schematic Diagram of the set-up for measuring Scattering Loss. . . . .	.79
Fig. 4.2.4.4	Scattering Loss Measurements for different waveguide sizes . . . . .	.80
Fig. 4.2.4.5	Measurements from cutback methods for 4 4.5 $\mu\text{m}$ core height waveguides. . . . .	.81
Fig. 4.2.4.6	Attenuation Loss versus Core Height . . . . .	.82
Fig. 4.3.1	Procedures of Metallizing the end-facets . . . . .	.86
Fig. 4.4.1	Mask Pattern for Direct E-beam Writing . . . . .	.89
Fig. 4.4.2	SEM Pictures of different sidewall taps . . . . .	.90

## **LIST OF TABLES**

Table 3.2.1 Parameters of the Amplifier Simulation . . . . .	45
Table 4.2.4.1 Coupling losses of different waveguide sizes. . . . .	83

## LIST OF ABBREVIATIONS

<b>AMC</b>	Alberta Microelectronics Center
<b>BOE</b>	Buffered Oxide Etch
<b>BPSG</b>	Borophosphorus Silicon Glass
<b>EDFA</b>	Erbium-Doped Fiber Amplifier
<b>EDP</b>	Ethylenediamine and Pyrocatechol
<b>ESA</b>	Excited-state Absorption
<b>FEM</b>	Finite Element Method
<b>HMDS</b>	Hexamethylene Disilazane
<b>IPA</b>	Isopropyl Alcohol
<b>KOH</b>	Potassium Hydroxide
<b>LPCVD</b>	Low Pressure Chemical Vapor Deposition
<b>NOA</b>	Norland Optical Adhesive
<b>PECVD</b>	Plasma-enhanced Chemical Vapor Deposition
<b>RIE</b>	Reactive Ion Etching
<b>SEM</b>	Scanning Electronic Microscope
<b>SFEM</b>	Scalar Finite Element Method
<b>SNR</b>	Signal-to-noise ratio
<b>TRLabs</b>	Telecommunication Research Laboratories
<b>VFEM</b>	Vectorial Finite Element Method

# **Chapter 1 Introduction**

## **1.1 Background and History of the V-groove waveguide**

In general, an optical waveguide can be defined as a light conduit consisting of a dielectric core material surrounded by another dielectric material of lower refractive index. The light is guided and transported mainly through the core to the destination with only small amount of optical power radiating into the surrounding medium. The structure of an optical waveguide can, in theory, be any shape, but the structure should be designed so that the fabrication can be done without a lot of difficulties. Also, an optical waveguide should be low loss and the light with desired wavelength should be easily coupled into the waveguide.

One type of optical waveguide is the optical fiber, which is now often used in high-speed optical communication system for long-distance signal transmission [1]. Another type of optical waveguide is the integrated optical waveguide used in optoelectronic circuits. In an optoelectronic circuit, the integrated optical waveguide acts like a wire in the electronic circuit, and transmits optical signals at a very high transmission rate. One way of making integrated optical waveguides is by etching grooves in the substrate of the circuit and filling the grooves with several layers of dielectric materials. This fabrication technique is called micromachining. The most often-used substrate material for making the optoelectronic circuits and other semiconductor devices is the silicon wafer which has the crystal structure. The etch rates of different crystallographic planes of the crystal silicon are quite different, which can be utilized for etching waveguide grooves. The v-groove waveguide is fabricated by this preferential etching, in which more details will be

given later.

The micromachined v-groove waveguide has been one of active research topics at TRILabs. In the past, researchers at TRILabs had fabricated very low-loss singlemode v-groove waveguides [2] and had demonstrated the feasibility of using the v-groove waveguide for light distribution applications [3]. These successes demonstrated that the v-groove waveguide is a potential element to be used in the optoelectronic circuit. In 1994, a joint project called HyPIC (Hybrid Photonic Integrated Circuit) was started in TRILabs to develop the integrated optics technology for wavelength division multiplex systems, instrumentation, computers, and switching subsystems. The micromachined v-groove waveguide is one of the optical components to be investigated in this project. This research is a part of the v-groove waveguide investigation in HyPIC, which is intended to provide a theoretical and experimental study of the possible applications and fabrication methods of the v-groove waveguide. The following is a brief description of the background and history of the v-groove waveguide.

The triangular structure of the micromachined v-groove waveguide is defined by the crystallographic planes of silicon. Usually, the crystallographic planes of anisotropic materials are labelled using the Miller Indices. The Miller Indices consist of three integer numbers,  $h$ ,  $k$  and  $l$ , which are usually written as  $\langle hkl \rangle$ . These three integers correspond to the reciprocals of the intercepts of a crystallographic plane with the three crystal axes. If the reciprocals of the intercepts are not all integers, they are multiplied by the least common multiplier of the intercepts. For crystal silicon, the etch rates of the major crystallographic planes generally follow the order  $\langle 100 \rangle > \langle 110 \rangle > \langle 111 \rangle$  [4]-[6]. The silicon v-groove is fabricated by this preferential (anisotropic) etching phenomenon and photoli-

thography. The purpose of the photolithography is to pattern the desired opening shape in the masking layer which is deposited on top of the silicon wafer. One commonly used masking material is thermally grown silicon dioxide which has uniform and defect-free film properties [5]. The anisotropic etchant attacks the bare silicon exposed by the opening in the masking layer. Aqueous potassium hydroxide (KOH) and an aqueous mixture of ethylenediamine and pyrocatechol (EDP) [7] are the most commonly used anisotropic etchants for silicon. For a  $\langle 100 \rangle$  oriented silicon wafer with a rectangular opening in the masking layer properly aligned in the  $\langle 110 \rangle$  direction, the etching process is as illustrated in Fig. 1.1.1. The etch rate in the  $\langle 100 \rangle$  (downward) direction is much faster than in the  $\langle 111 \rangle$  direction. Therefore, the etching is effectively bounded by the  $\langle 111 \rangle$  planes. The  $\langle 111 \rangle$  plane makes an angle of  $54.74^\circ$  with the  $\langle 100 \rangle$  silicon surface. After a sufficient etch time, the four  $\langle 111 \rangle$  planes will meet and the v-groove is formed. If the rectangular opening is misaligned, the sidewalls of the resulting waveguide will have a stair-case appearance. The v-groove etching procedures can be found in Appendix C.



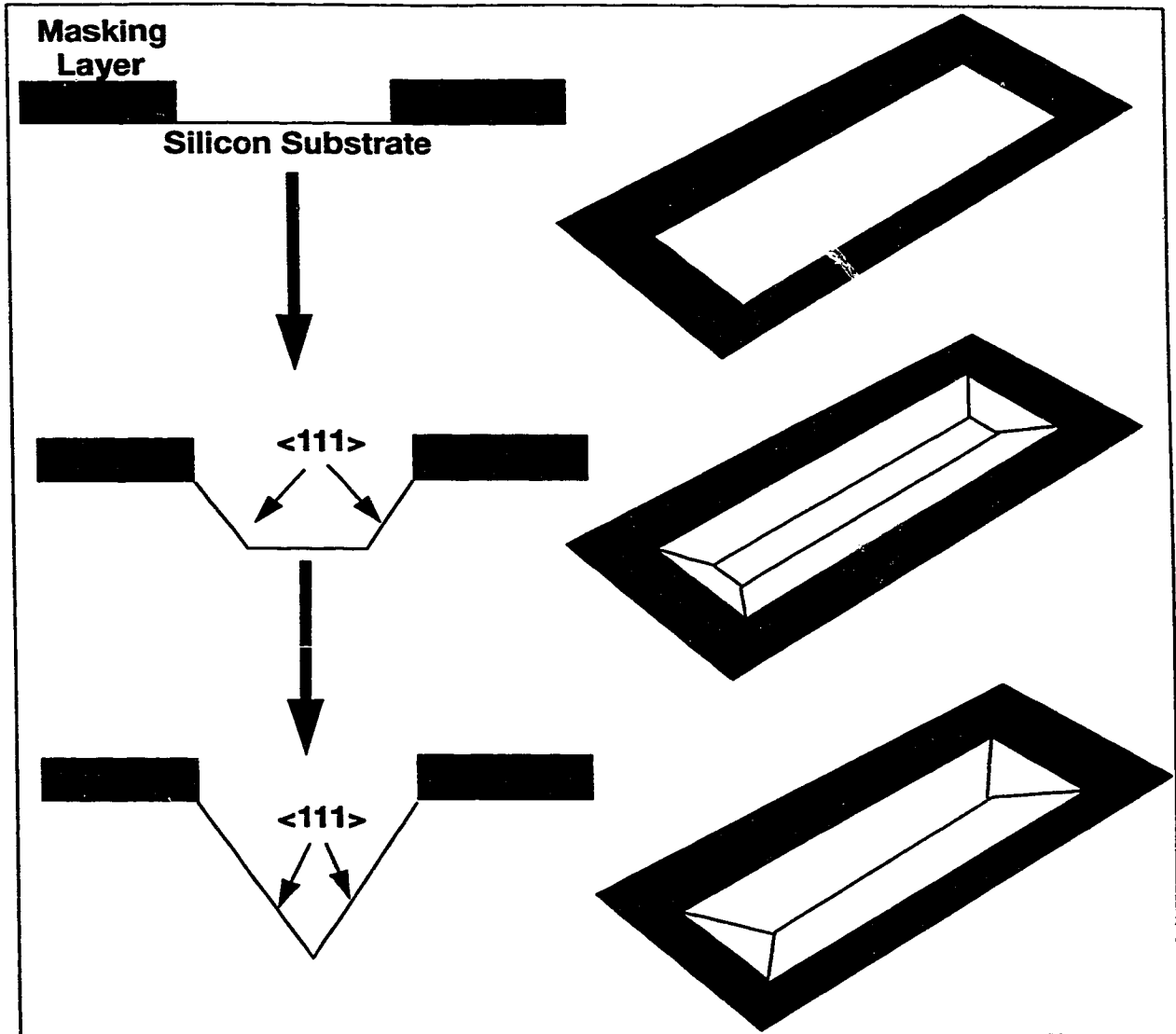


**Fig. 1.1.1 Etching Process of a silicon V-groove**

One advantage of this type of waveguide is that the sidewalls defined by the  $\langle 111 \rangle$  planes are very smooth, and this greatly reduces the propagating loss introduced by the edge roughness. Other types of waveguides such as strip-loaded waveguides, channel waveguides and rib waveguides cannot eliminate this sidewall roughness completely [10], and hence introduce higher attenuation. There are also other attractive features of the v-

groove waveguide such as fabrication compatibility with v-groove fiber alignment [8], vertical coupling to surface-mounted optoelectronics from end-facets or integrated taps formed by micromachining techniques[3], and high precision ensured by the self-limiting geometry obtained during preferential etching [2].

Over the years, much research has been done to investigate various ways of fabricating this type of waveguide. As early as 1975 [10], the successful fabrication of a v-groove waveguide was reported. The v-groove was etched in a mixture of KOH+IPA (isopropyl alcohol). The resulting v-groove had very smooth <111> sidewalls. The width of the waveguide was 4.8  $\mu\text{m}$ . The core was filled by polyurethane after 1 $\mu\text{m}$  of silicon dioxide was deposited into the v-groove. No optical testing was done to the resulting waveguide, and therefore the quality of the waveguide was unknown. However, the experiment demonstrated that the anisotropic etching can provide a rather simple way of making waveguides with smooth sidewalls.

More than a decade later, the fabrication of a very low-loss singlemode phosphorus-doped silica v-groove waveguide was reported by Narendra [2]. The loss of the waveguide was about 0.1 dB/cm, which is very low. The anisotropic etching was done using EDP. The core and cladding layers were both deposited using low pressure chemical vapor deposition (LPCVD). The core of the waveguide was formed by first depositing a thick layer of phosphorus-doped glass which was then etched in buffered oxide etchant (BOE) until the desired shape was obtained. The width of the waveguide was less than 2  $\mu\text{m}$ .

At about the same time, Kumar reported the fabrication of an integrated multi-mode polymer v-groove waveguide [3]. In one such waveguide, 12 sidewall taps were

integrated into the v-groove in an attempt to tap the same amount of optical power at each tap. In general, a waveguide tap can be viewed as a beam splitter in which a portion of the propagating light in the waveguide is reflected by the surface of the tap to another direction (usually in an out-of-plane angle). A sidewall tap is formed by undercutting the two convex corners of an indented rectangular block attached at one side of the rectangular opening in the masking layer. These convex corners are illustrated in Fig. 1.1.2 a. During the anisotropic etching, the etchant attacks the two orthogonal sides of the convex corners and the undercutting occurs. Since the etch rates for both sides of the corner are the same, the undercutting direction follows the 45° diagonal line of the corner as shown by the arrows in Fig. 1.1.2 (b). Fig. 1.1.2 b shows the etching sequence for the sidewall tap. The plane exposed in the undercutting depends on the type of the etchant used. A general shape of the sidewall tap is illustrated in Fig. 1.1.2 c. By metallizing the undercutting planes (shaded in the figure), the sidewall tap can act as a beam splitter, which reflects a portion of the propagating light out of the waveguide. In Kumar's work, the v-groove was etched by EDP, and the undercutting plane was  $\langle 212 \rangle$ . The multimode waveguide was made of a LPCVD oxide lower cladding and a polymer core. The deposition of the polymer core was done by dispensing the polymer using the squeezable container on the v-groove. The excess polymer was removed by a rubber sheet with a sharp edge. The remaining polymer on the surface was removed by soft abrasive paper after curing. The resulting waveguide had a concave surface. At the edges of the waveguide, roughness was seen which was due to the abrasive action. The measured loss of the waveguide was close to 1 dB/cm. The experimental results showed that the tapped power was not uniformly distributed among the taps. However, Kumar's work demonstrated that this integrated

waveguide is a potential light distribution device for a hybrid integrated optoelectronic circuit.

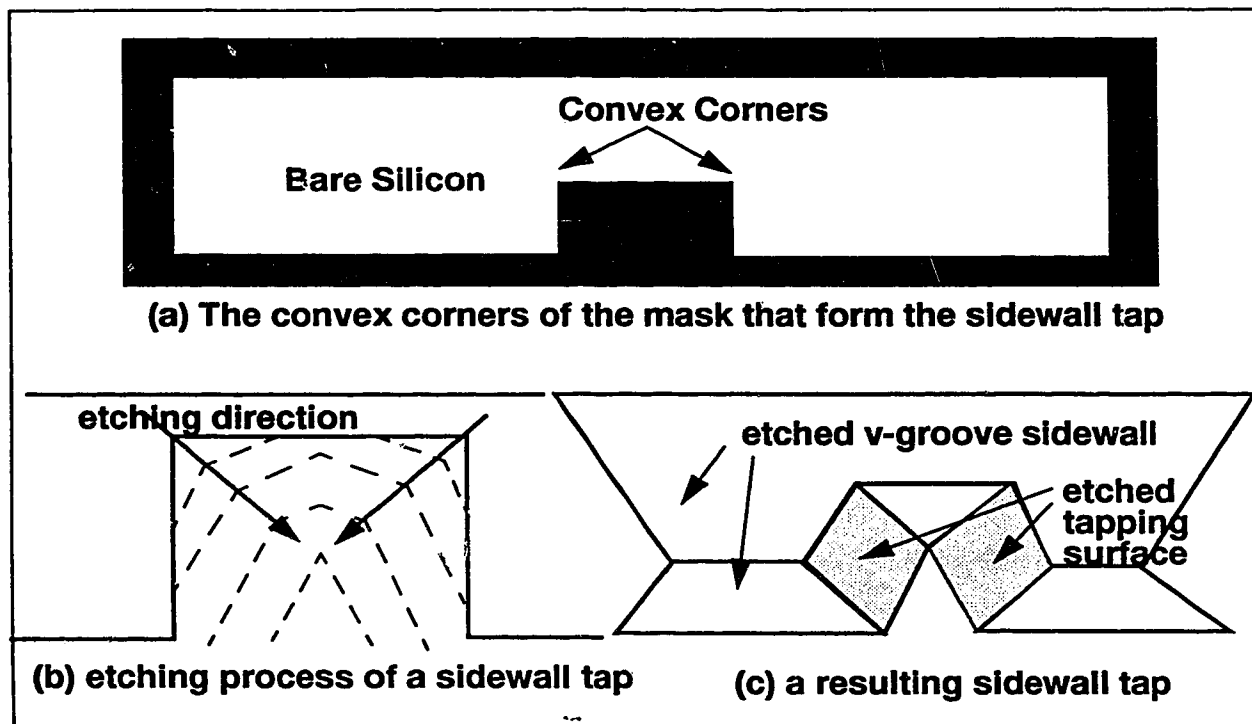


**Fig. 1.1.2 The formation of a sidewall tap**  
**(a) Mask outline before etching**  
**(b) Details of undercutting at convex corners**  
**(c) Overview of etched v-groove with a tap**

Two years later, Fei fabricated another type of integrated multimode v-groove waveguide for optical coupling [40]. Center taps were used for the out-of-plane tapping in this waveguide. The fabrication of a center tap requires two masking steps. The first mask contains a single rectangular opening, which defines the etching area of the waveguide. The second mask is modified from the first mask, with the area intended for forming the center tap blocked; the resulting mask has two rectangular openings of the same width side by side as shown in Fig. 1.1.3. At first, the v-groove is partially etched using the first

mask. Then the area for forming the center tap is covered by a protective layer. This is done by depositing another masking layer and patterning the masking layer with the second mask. The partially etched v-groove then undergoes the second anisotropic etching, and two v-grooves will be formed side by side at the end of the etching. The center tap is formed by removing the masking layer on the center tap region, and the wafer is immersed into the etchant again. After a sufficient amount of etch time, the resulting tap has the shape as illustrated in Fig. 1.1.4. In Fei's work, EDP was used and the two planes that define the center tap were  $\langle 211 \rangle$ . Unfortunately, the optical measurement of the resulting integrated waveguide is inconclusive. The performance of the tapping mechanism is not certain.

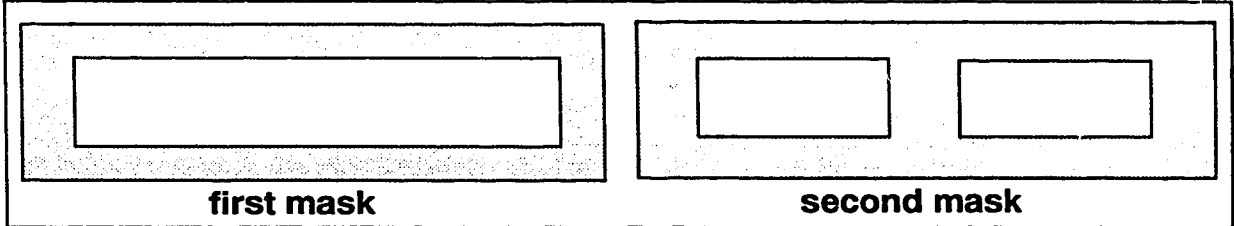


**Fig. 1.1.3 Two photolithography masks for making center tap**

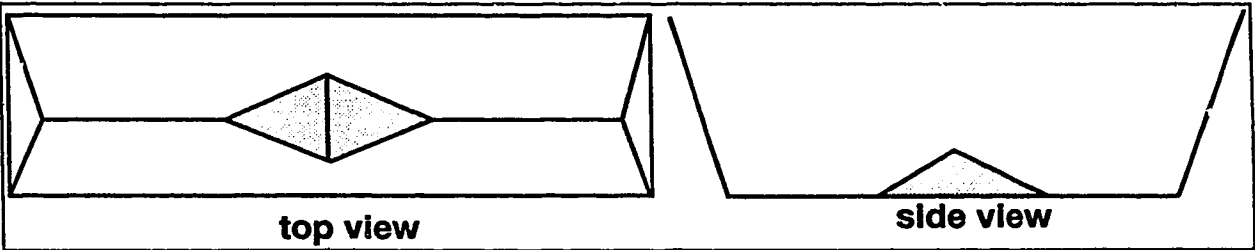


**Fig. 1.1.4 A center tap in the V-groove**

Recently, Macleod [37] attempted to refine the design of multimode v-groove waveguides. In order to accurately design the required dimensions for the center and side-

wall taps, Macleod developed a computer program to simulate the beam propagation in a multimode v-groove waveguide with these taps in place. The simulation results showed that the amount of tapped power is proportional to the ratio of the tap area and the waveguide cross-sectional area. Also the results showed that a 3 mm separation between the taps is sufficient to avoid any shadowing effects. Fabrication methods for both sidewall and center taps were repeated by Macleod. KOH was used in the center tap etching experiment. The planes that define the center tap were found to be  $\langle 411 \rangle$  instead of  $\langle 211 \rangle$ . The  $\langle 411 \rangle$  plane is too shallow for tapping purposes. Therefore, the investigation of the center tap array was terminated. Both KOH and KOH+IPA were tried in etching the sidewall tap. It was found that the undercutting rate of KOH was too rapid to be of use. The KOH+IPA mixture provided the suitable etch rate. A mask was then designed based on the simulation results for the sidewall taps, and an integrated multimode v-groove waveguide with four sidewall taps was fabricated. The results show that the loss of the waveguide was about 1 dB/cm, similar to Kumar's results. The tapped power was quite uniform, except that the tapped power at the end-facet was a few dB lower.

## **1.2 Other applications for the v-groove waveguide**

Vertical light coupling from a v-groove waveguide can also be achieved simply by using the metallized end-facet of the waveguide as the reflective surface. Fig. 1.2.1 and Fig. 1.2.2 illustrate two different applications of this simple light coupling feature. The optical reader shown in Fig. 1.2.1 may provide an alternative way to integrate a discrete optical reading unit with other components in a CD player. The gratings on top of the end-facets would be used to redirect the reflected light to the vertical direction, since the end-

facets do not make an 45o angle with the vertical axis. Flip-chip interconnection shown in Fig. 1.2.2 is a simple and inexpensive way to establish high-speed chip-to-chip communication. Information between chips can be carried by light in v-groove waveguides. Light is coupled in and out of the waveguides by reflective taps under the chips. In this way, the speed of information transmission would not be limited by the medium that guides the signal to the destination.

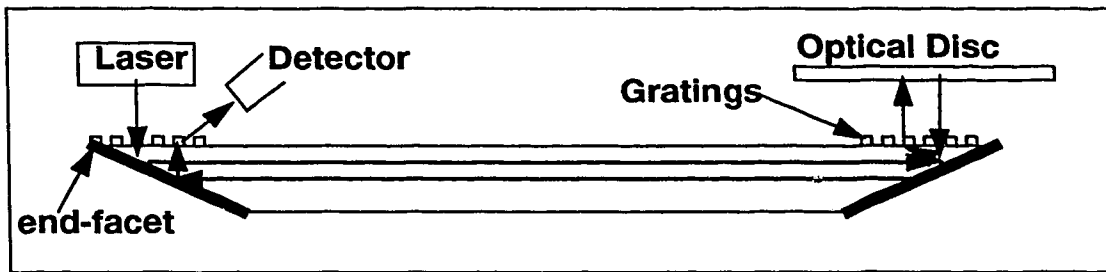


**Fig. 1.2.1 Schematic diagram of a Optical Reader**

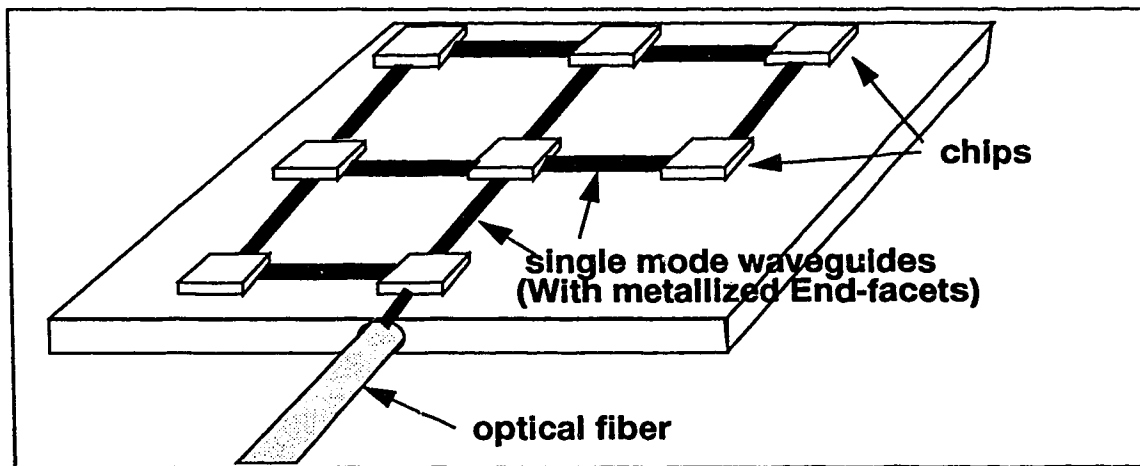


**Fig. 1.2.2 Schematic diagram of flip-chip Interconnections**

Another important application of the waveguide may be in optical amplification.

The first amplification in a fiber laser [12] was demonstrated in 1964 using Nd<sup>3+</sup>-doped

glass. The making of a fiber amplifier by doping rare-earth metal into low-loss singlemode silica fiber was reported two decades later [13]. Among the rare-earth metals, erbium is a widely used material for making fiber amplifiers. Erbium-doped glass has several advantages. It has a relatively long metastable life time which is one of the key factors in producing an efficient amplifier. Also, the erbium glass has an emission spectrum which coincides with the long-wavelength optical communication window around 1550 nm, and it has 5 absorption lines (at around 380 nm, 530 nm, 650 nm, 780nm and 980 nm [20]) which are all practical for pumping purposes. A practical absorption line is referred to as a particular optical frequency region (line) where the optical power of the pump light can be absorbed by the amplifier material and use for increasing the signal power. More theoretical background about the absorption of the pump light is given in Chapter 3. In addition, evidence has shown that the erbium glass is relatively polarization-insensitive [14]. Nowadays, the Erbium-Doped Fiber Amplifier (EDFA) has become a major component in high-speed long-distance fiber communication systems.

In the past few years, many researchers have switched the focus to making a waveguide amplifier. The erbium concentration of the waveguide amplifier must be a few orders of magnitude higher than the conventional EDFA [15]. This reduces the required gain-length to a few centimetres, a suitable length for hybrid integrated optoelectronic circuits. Many different fabrication methods and waveguide structures have been tested in the past decade [15]-[25] and in general the results are promising. However, among these reports, none has investigated the v-groove structure. The advantage of using the v-groove structure is that it has fabrication compatibility with the fiber alignment groove, which is used to align the optical fiber to the optoelectronic circuit board. Fig. 1.2.3 shows a sche-



matic diagram of the possible configuration of a v-groove amplifier.

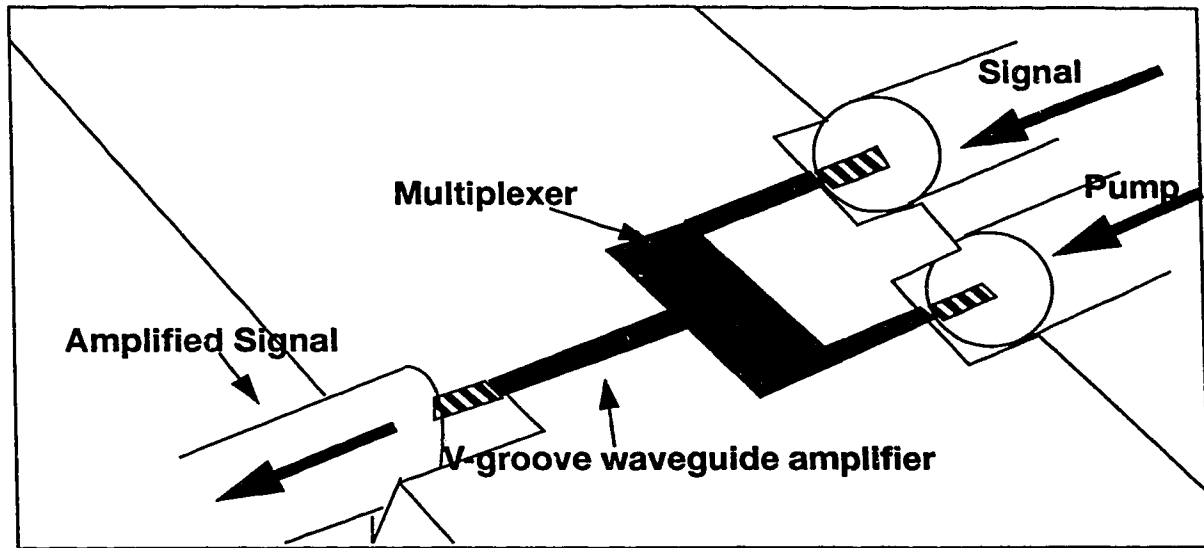


**Fig. 1.2.3 Schematic Diagram of the V-groove Waveguide Amplifier**

### **1.3 Research scope**

As mentioned in the last section, major potential applications of the v-groove waveguide are vertical coupling applications and optical amplification. Previous research has shown some success in multimode light coupling, but not in the singlemode waveguide [37], [39], [40]. Singlemode propagation is an important requirement for high-speed fiber communication; therefore an investigation of the singlemode coupling is interesting. The dimension of a singlemode waveguide is only a few times the wavelength of the propagating light in the communication window (whereas the size of a multimode waveguide is typically greater than 50 times larger). Therefore, the propagation of light can no longer be described by simple ray optics. Also, the problem of light coupling is expected to be more difficult than for multimode waveguides. Thus experiments are required to examine both the coupling efficiency and the mode shape. It is also worthwhile

to investigate the feasibility of integrating sidewall taps into the singlemode v-groove for optical interconnect applications. Since previous research has shown that many metals cannot withstand the high temperature fabrication procedures after the metal has been deposited into the v-groove [36], experiments have to be conducted to determine a suitable candidate for metallizing the tapping plane.

In order to estimate the waveguide amplifier performance before actual fabrication, simulations are required to design the optimum length of the waveguide and to calculate the desired erbium concentration and v-groove dimensions. The simulations consist of two parts. The first part determines the optimal size of the v-groove for singlemode propagation. The second part simulates the gain characteristics of the active waveguide. Moreover, these simulations can also be used for analysing the dispensed singlemode polymer waveguide. The polymer dispensing technology may provide an inexpensive and less time-consuming method of making singlemode waveguides.

## **1.4 Thesis Outline**

This thesis is divided into two parts. The first part involves the theoretical calculations of the singlemode sizes of different type of waveguides and the amplifier simulations. The second part deals with the actual waveguide and tap fabrication experiments and their experimental measurements.

Chapter 2 discusses the modal analysis for both erbium-doped waveguides and polymer waveguides. Various parameters that affect mode field distribution and waveguide performance will be analysed. Chapter 3 discuss the amplifier simulation results. The effect of pump power, waveguide length and erbium concentration will be

analysed. The fabrication of polymer waveguides and sidewall taps will be presented in Chapter 4. The waveguide measurement and the results of metallizing the end-facet will be included in this chapter. Chapter 5 discusses the results obtained from this research and proposes some recommendations for future work.

# **Chapter 2 Mode Field Calculations using Finite Element Analysis**

## **2.1 Introduction**

The Finite Element Method (FEM) is a widely-used numerical tool for solving electromagnetic wave problems [33]. In this method, the problem domain is divided into sub-domains (finite elements), and the solution of the problem is obtained by finding approximated numerical values of the electromagnetic field at the vertices of the finite elements which can closely fit into the approximate problem equation. For two-dimensional problems, the triangular element is the most popular choice.

There are numerous methods to search for the numerical solutions for FEM problems. Most of these methods belong to the two major branches of the FEM, namely the variational method and the weighted residual method. This project uses Galerkin's method which belongs to the weighted residual family. One of the advantages of Galerkin's method is that it can solve many electromagnetism problems directly from second order differential equations, whereas for variational methods, the problem must be expressed as a variational equation before solving it.

In the following sections, the background theory for solving the mode field is given, then the procedures for solving the mode field will be described. The last section analyses the FEM results and the effect of various waveguide parameters.

## **2.2 Background Theory for Modal Analysis**

In general, the mode field of the guided propagating light cannot be computed analytically. In many cases, the mode-field distribution is obtained by numerical methods.

These numerical methods find the best-fit propagating constant and the corresponding field to the wave equation derived from Maxwell's equations. A brief derivation of the wave equation is presented next.

The electric and magnetic fields are assumed to have sinusoidal time dependence, that is,  $\mathbf{E} = \mathbf{E}(x,y,z) e^{j\omega t}$  (electric field),  $\mathbf{H} = \mathbf{H}(x,y,z) e^{j\omega t}$  (magnetic field), and the material is assumed to have zero conductivity ( $\omega$  is the angular frequency of the propagating light). The electric permittivity of the material is assumed to have the form  $\epsilon = n(x,y,\omega)2\epsilon_0$ , where  $n$  is the refractive index of the material and  $\epsilon_0$  is the electric permittivity of the vacuum. Hence, the vector Maxwell's equations can be written as follows,

$$\nabla \times \mathbf{H} = i\omega n^2 \epsilon_0 \mathbf{E} \quad (2.1)$$

$$\nabla \times \mathbf{E} = -i\omega \mu_0 \mathbf{H} \quad (2.2)$$

In these equations,  $\mathbf{E}$  is the electric field intensity (volts/meter),  $\mathbf{H}$  is the magnetic field intensity (amperes/meter);  $\mu_0$  is the magnetic permeability in vacuum. By taking the curl of (2.1) and substituting (2.2) into the resultant equation, the following equation is obtained.

$$\nabla \times (\nabla \times \mathbf{E}) = n^2 k_0^2 \mathbf{E} \quad (2.3)$$

where  $k_0 = \omega \sqrt{\epsilon_0 \mu_0}$ . With the mathematical identity

$$\nabla \times (\nabla \times \mathbf{E}) = \nabla (\nabla \cdot \mathbf{E}) - \nabla^2 \mathbf{E} \quad (2.4)$$

and the third Maxwell's equation in a source-free region,

$$\nabla (\epsilon \mathbf{E}) = 0 = \mathbf{E} \cdot \nabla \epsilon + \epsilon \nabla \cdot \mathbf{E} \quad (2.5)$$

(2.3) can be written as

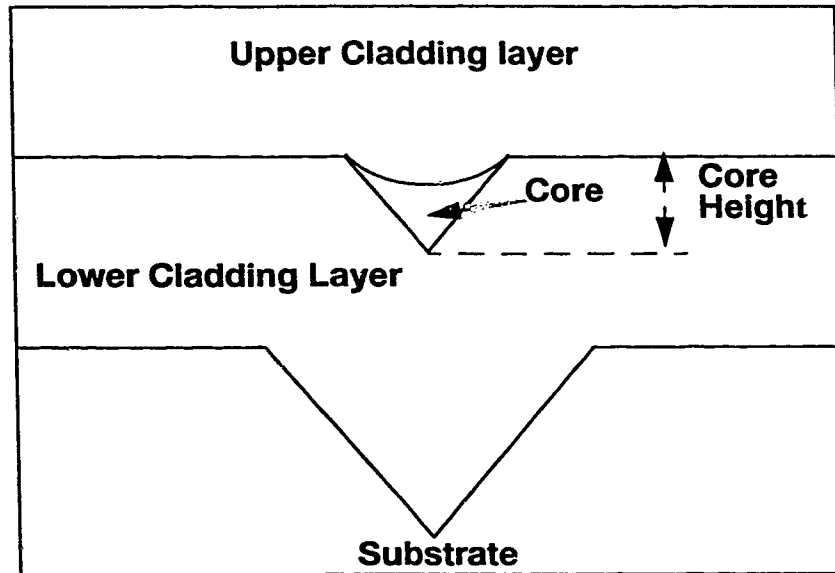
$$\nabla^2 \mathbf{E} + \nabla \left( \frac{1}{\epsilon} \mathbf{E} \nabla \epsilon \right) = -n^2 k_0^2 \mathbf{E} \quad (2.6)$$

The second term on the left side of the equation is assumed negligible to simplify the calculation. This assumption is valid if  $|\nabla \epsilon| \leq \epsilon/\lambda$  [26], which implies that the scale length of the refractive index in the waveguide is large compared to the wavelength of the propagating light. For guided propagating modes, the field solution has a z-dependence which is written as  $e^{-i\beta z}$ , where each mode has a unique  $\beta$ . Thus the Laplace operator assumes the form  $\nabla^2 = \partial^2 / (\partial x^2) + \partial^2 / (\partial y^2) - \beta^2$  and the final wave equation has the form of

$$\frac{\partial^2}{\partial x^2} \mathbf{E} + \frac{\partial^2}{\partial y^2} \mathbf{E} + (n^2 k_0^2 - \beta^2) \mathbf{E} = 0 \quad (2.7)$$

This is a typical differential form for Scalar Finite Element Method (SFEM). The vectorial version of the finite element method (VFEM) usually gives more accurate results, but the major problem is that it might have spurious solutions [27]. Some researchers have shown that SFEM can also provide good estimates of the field even for strongly guided light[27]. The modal analysis in this research has been carried out by the SFEM. The analysis assumes that the electric field distributions of both TE and TM waves are close; thus only the TE wave is analysed. The modal analysis is applicable to both polymer and glass waveguides.

## 2.3 The mode-solving procedures



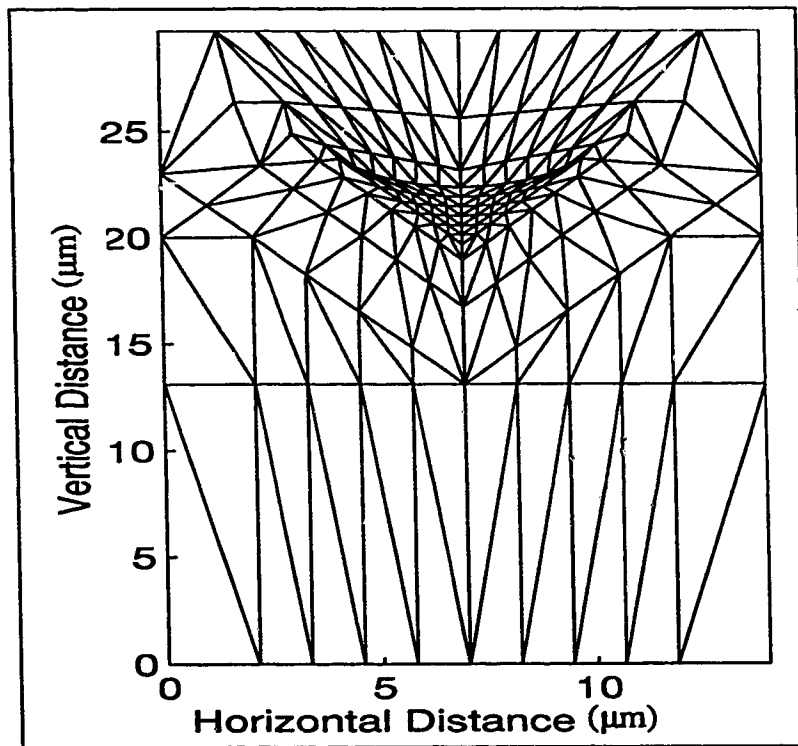
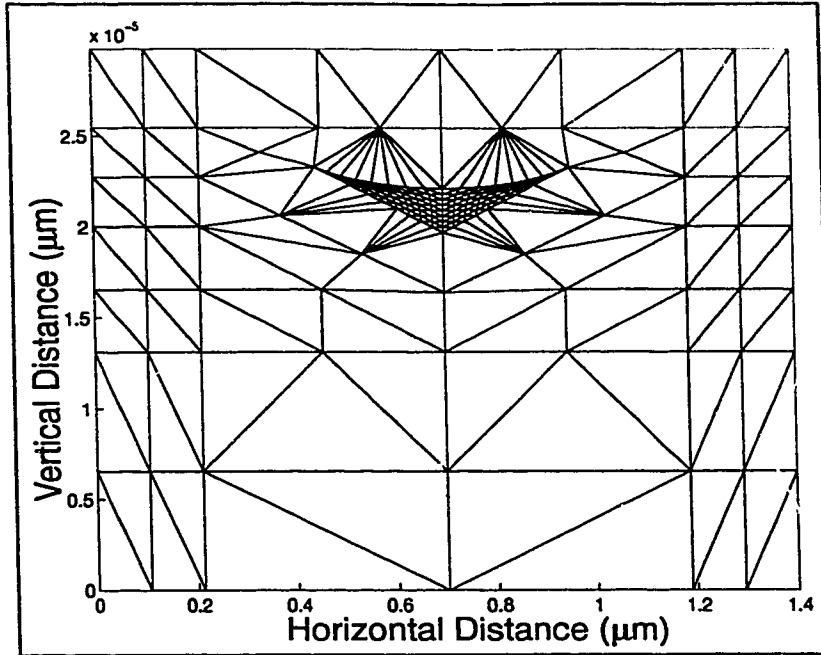
**Fig. 2.3.1 Diagram of the V-groove Waveguide Structure**

Fig. 2.3.1 shows the problem domain for the v-groove waveguide. The problem domain consists of four regions which have different refractive indices. The refractive index of the silicon substrate is fixed at 3.5 [28]. The core and cladding indices can be varied according to the selection of materials.

The first step in solving the mode field of the waveguide is to divide the entire waveguide domain into small triangular finite elements. There are no fixed rules for determining the sizes of the finite elements but the rule of thumb is to avoid having very different neighboring element sizes; that is, the sizes of the elements should change gradually. Also, where more detail is required, more elements should be present. In particular, since the change of the electric field is often more rapid near the corners of the waveguide, more elements may be needed at these regions. Within each element, the refractive index is set

constant; therefore, one finite element cannot cover two different refractive index regions. The optimal number of finite elements required is determined by actually increasing the number of finite elements in the problem domain until the convergence of the calculated solution is obtained, that is, the solution no longer changes. The coordinates of the nodes (vertices of the triangles) and the refractive indices of the elements are stored in matrices. Fig. 2.3.2 shows two ways of dividing a waveguide into finite elements. As shown in the figure, the first dividing scheme does not really follow the rules mentioned. The difference in the sizes of neighboring elements change quite remarkably. The second dividing scheme follows the guidelines more closely. However, the calculations from these two dividing schemes show that the calculated propagation constant,  $\beta$ , agrees to 3 significant figures in many cases. The reason is that in many cases only the fundamental mode is calculated, and the mode field is concentrated inside the core. Therefore, the sizes of the elements outside the core region do not affect the calculated results significantly. In any case, the second dividing scheme was used in the analysis.





**Fig. 2.3.2 Schematic diagrams of dividing V-groove Waveguide into Finite Elements**

After dividing the waveguide into finite elements, the next step is to extract required information from each finite element to construct the approximated equation derived from the wave equation for solving. In the wave equation (2.7) and many other second order differential equations, the right-hand side of the equation is zero. The weighted residual method treats the left-hand side of the problem equation as a residual,  $r$ , which is to be minimized. A weight factor,  $W$ , multiplies to the residual and the weighted residual is minimized in each finite element in a way that  $\int_A W r dA = 0$ . Here,  $A$  is the area of a finite element. Three equations are generated from this weighted residual equation for each finite element. In Galerkin's method,  $W$  is derived from the shape function which approximates the numerical solution in each finite element. In many cases, the shape function has the planar form of  $\phi = a + bx + cy$ ;  $a$ ,  $b$  and  $c$  are constants. Since the nodes (vertices of the triangles) of the elements are interconnected, the equations corresponding to the same nodes can be assembled together. After assembling, the total number of equations for all elements is equal to the number of nodes. There are two unknowns in each approximated equation, the electric field amplitude and the propagation constant. These equations can be put into a matrix form as follows,

$$[A] \{\phi\} = \lambda [B] \{\phi\}$$

where  $A$  and  $B$  are matrices,  $\lambda$  is the eigenvalue (the square of the propagation constant) and  $\phi$  is the eigenvector (the discrete values of the electric field). This is a typical generalized eigenvalue problem. A detailed description of the SFEM procedures can be found in

[33].

After solving for the eigenvalues and eigenvectors, the guided mode fields can be found by examining the eigenvalues. The eigenvalues give the squares of the propagation constants,  $\beta$ , which can be written  $\beta = n_{\text{eff}} k_0$ , where  $n_{\text{eff}}$  is the effective refractive index. Therefore, a list of  $n_{\text{eff}}$ 's can be found from the eigenvalues. For guided propagating modes,  $n_{\text{eff}}$  is bounded between  $n_{\text{clad}}$  and  $n_{\text{core}}$ . In the case of an optical amplifier, the core is filled with erbium-doped glass and the refractive index is labelled as  $n_{\text{erbium}}$ ; therefore  $n_{\text{eff}}$ 's are bounded between  $n_{\text{clad}}$  and  $n_{\text{erbium}}$ . The mode fields of the propagating modes are the corresponding eigenvectors of those valid eigenvalues.

A brief description of the finite element program can be found in Appendix A. The erbium-doped silica waveguide and the polymer waveguide will be analysed in the following section. The parameters determining the singlemode light propagation, such as the size of the waveguide, the refractive indices of different regions, and the wavelength of the propagating light are analysed. Other factors that influence the performance of the waveguides will be discussed.

## **2.4 Analysis and Discussion of the SFEM Results.**

### **2.4.1 The erbium-doped waveguide amplifier**

The refractive indices of the upper and lower cladding are both set to 1.44, which corresponds to that of the undoped silicon dioxide. The index of the erbium-doped core is set to 1.59 which is the value of the erbium-doped silica glass being studied at TRILabs. The lower cladding thickness is set to 4.5  $\mu\text{m}$  to avoid any tunnelling effect. The most important result in the analysis is the size of the core which allows only singlemode prop-

agation. Since the core height and width have a fixed ratio, the value of the core height is used to indicate the core size in the following discussion. The core height is defined as the distance from the upper surface of the lower cladding layer to the lower tip of the core, as shown in Fig. 2.3.1.

Fig. 2.4.1.1 shows the singlemode intensity contour plots at both pump, 980 nm, and signal, 1550 nm, wavelengths. The contour lines represent 10% intervals in intensity. The core height is 1.30  $\mu\text{m}$  which is the maximum for singlemode propagation at 980 nm. The waveguide is always singlemode at 1550 nm if it is singlemode at 980 nm. The confinement factors at this core size are 72.4% and 42.7% for 980 nm and 1550 nm respectively. The confinement factor is defined as the percentage of the optical power confined in the active region and should be as high as possible for a short amplifier. The mode contour lines at both wavelengths are circular near the center of the core, and they gradually become more triangular in shape as the lines draw closer to the core-cladding boundaries. In general, the fundamental mode shape resembles the shape of the core.

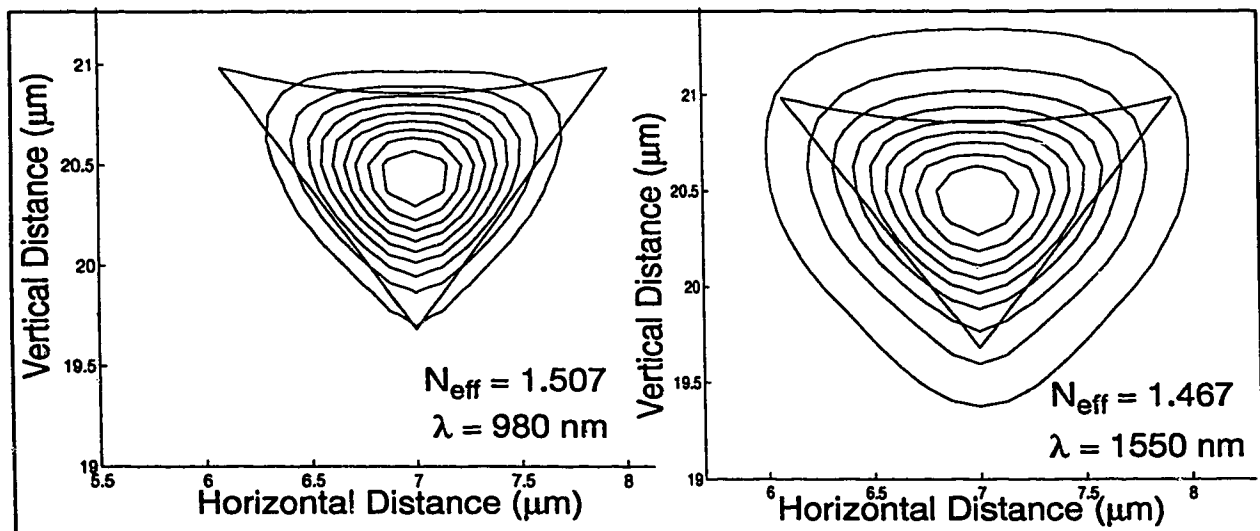


**Fig. 2.4.1.1 Intensity Contour Plots at 980 nm and 1550 nm**

In an optical fiber, the number of guiding modes can be determined by finding the normalized frequency,  $V$ , which can be expressed as  $V = \frac{2\pi}{\lambda} \sqrt{n_1^2 - n_2^2} a$ ; where  $\lambda$  is the wavelength of the propagating light;  $n_1$  and  $n_2$  are the refractive indices of core and cladding; and  $a$  is the radius of the core. The  $V$  number is directly proportional of the radius of the core and the numerical aperture (equal to square root term in the  $V$  expression), and inversely proportional to the wavelength of the propagating light. An optical fiber is singlemode if  $V \leq 2.4$  [1]. For the v-groove waveguide, a similar expression for the  $V$  number can be derived. Instead of being proportional to the radius of the core, the  $V$  number of the v-groove can be made proportional to the core height. The following is a derivation of the  $V$  expression for the v-groove waveguide.

$$\begin{aligned} V &= \frac{2\pi}{\lambda} \sqrt{n_1^2 - n_2^2} a \\ &= \frac{2\sqrt{\pi}\sqrt{\pi a^2}}{\lambda} \sqrt{n_1^2 - n_2^2} \\ &= \frac{2\sqrt{\pi}\sqrt{a_c}}{\lambda} \sqrt{n_1^2 - n_2^2} \end{aligned}$$

where  $a_c = \pi a^2 =$  area of the fiber core

the core area of the v-groove waveguide is proportional to the square of the core height because of the fixed ratio between height and width. Taking into account the curvature at the core surface, the area of the v-groove core equals  $0.6123 h^2$  ( $h =$  core height). If the area of the fiber core is replaced by the area of the v-groove core, the expression for the  $V$  number becomes

$$= \frac{2.774h}{\lambda} \sqrt{n_1^2 - n_2^2}$$

Using this expression and setting  $V = 2.4$ , the estimated maximum core height would be

1.25  $\mu\text{m}$ , which agrees quite well with the calculated value (1.30  $\mu\text{m}$ ) from the modal analysis.

The above calculations provide an estimate of the maximum core size. However, during the fabrication process, the size of the waveguide, the thickness of the deposited material and the etching depth cannot be exactly matched to the specifications. Various factors affect the fabrication precision. Typically, the height of the core varies by  $\pm 0.2$   $\mu\text{m}$ . Thus, even if the SFEM provides an accurate estimation, a design margin must be imposed to guarantee the singlemode propagation in the waveguide. Nevertheless, the size of the waveguide cannot be made too small, because the mode field spreads more into the cladding layer as the core size is reduced. This in turn reduces the optical power confined in the active region. Therefore, an optimal size of the core must be computed to obtain an acceptable power confinement and coupling efficiency.

Taking the  $\pm 0.2$   $\mu\text{m}$  uncertainty into account, the waveguide should have a core height of 1.1  $\mu\text{m}$  to ensure singlemode propagation. Fig. 2.4.1.2 shows how the confinement factor decreases as the core height is reduced. As shown in the figure, if the core is 1.1  $\mu\text{m}$  high, the confinement factors will drop by 10.7% and 14.7% for 980 and 1550 nm respectively. With 0.2  $\mu\text{m}$  tolerance, the actual fabricated waveguide may have a core height of 0.9  $\mu\text{m}$  and the confinement factors will drop to 46.1% and 13.5% respectively. The confinement factor of the signal light may be insufficient to provide a reasonable gain in a short distance. This will be justified in the next chapter.

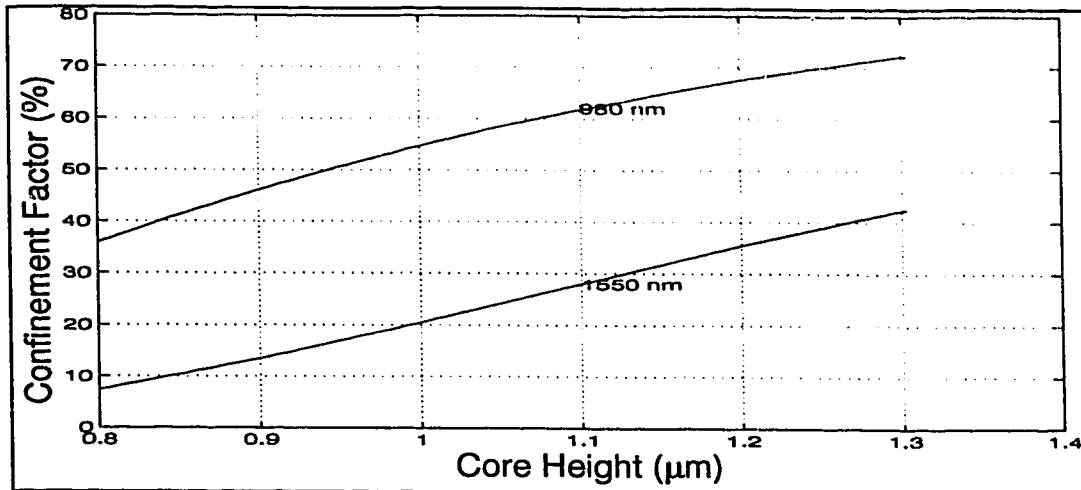


**Fig. 2.4.1.2 Confinement Factor versus Core Height.**

To increase the signal confinement factor, the only simple solution is to increase the core size, but this might result in multimode propagation for the pump light. The optical power distribution of a multimode waveguide is no longer necessarily concentrated around the center of the core, but spreads to the entire core. Also, the distribution will depend on the launching condition. In order to obtain high gain efficiency, the mode shape of the signal must resemble that of the pump. Thus, even if the confinement of the signal is enhanced, the gain efficiency does not necessarily increase accordingly. Fig. 2.4.1.3 shows 4 propagating modes at 980 nm for a singlemode signal propagation. The core height is 2.0 μm which is at maximum for singlemode propagation at 1550 nm. As depicted in Fig. 2.4.1.3, the 4 propagating modes have very different field distributions and the combined field will spread over the entire core area. Simulations and experiments would be required to determine the actual gain efficiency for this core size.

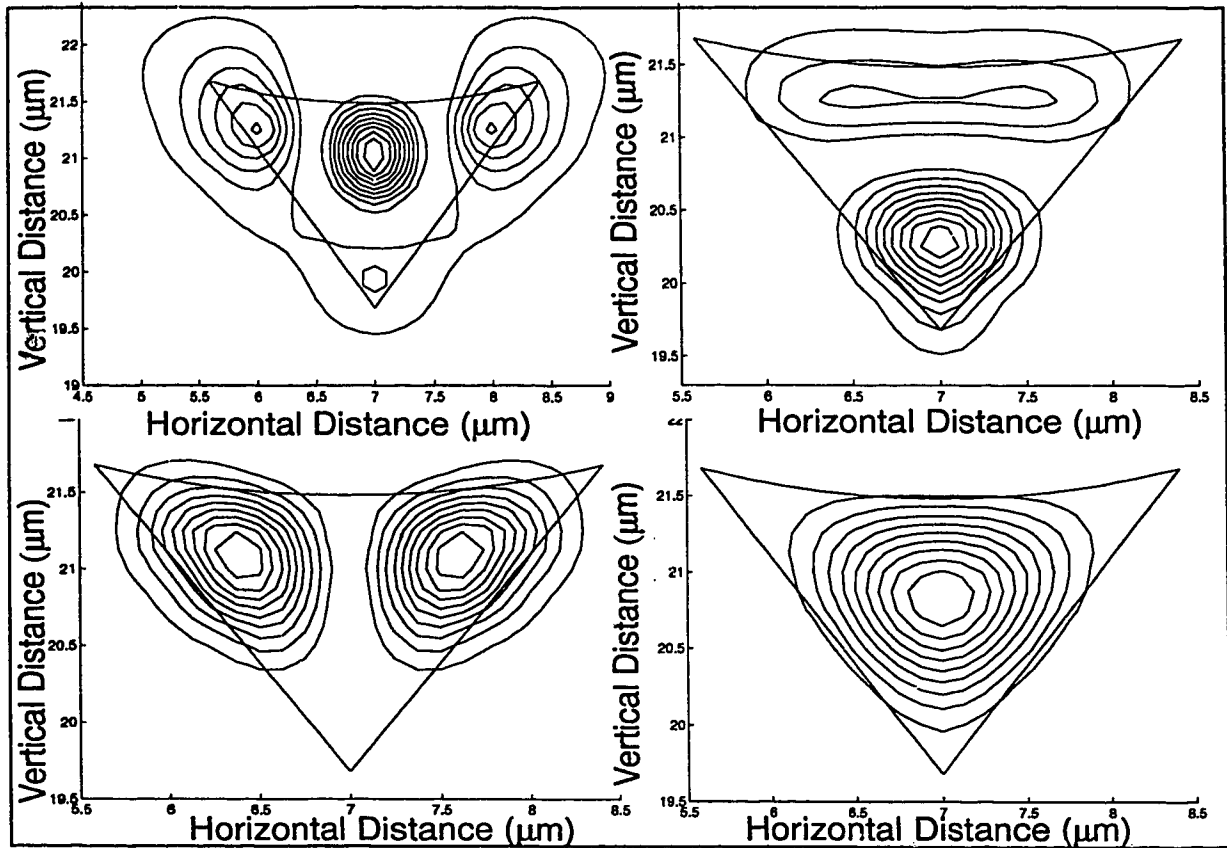


**Fig. 2.4.1.3 Intensity Contour Plot of 4 modes in 2  $\mu\text{m}$  core at the 980 nm pump wavelength**

Other than the size of the core, the index difference between core and cladding may also affect the confinement factor. The index difference may vary due to the slight index change during the deposition. Also, in order to reflow the cladding layer to obtain the desired shape, one may be required to dope the silicon-dioxide with boron and phosphorus to reduce the softening point. The dopant increases the refractive index by an amount proportional to the concentration of the dopant. The index can be increased up to 1.48. With the core height at 1.3  $\mu\text{m}$ , Fig. 2.4.1.4 shows how the confinement factor decreases as the cladding index increases. The confinement factor of the signal is reduced



by 12% as the cladding index increases to 1.48; the change is quite significant. Since the exact index change due to dopant addition is unknown, it is advisable that the doping concentration of silica cladding be minimized.

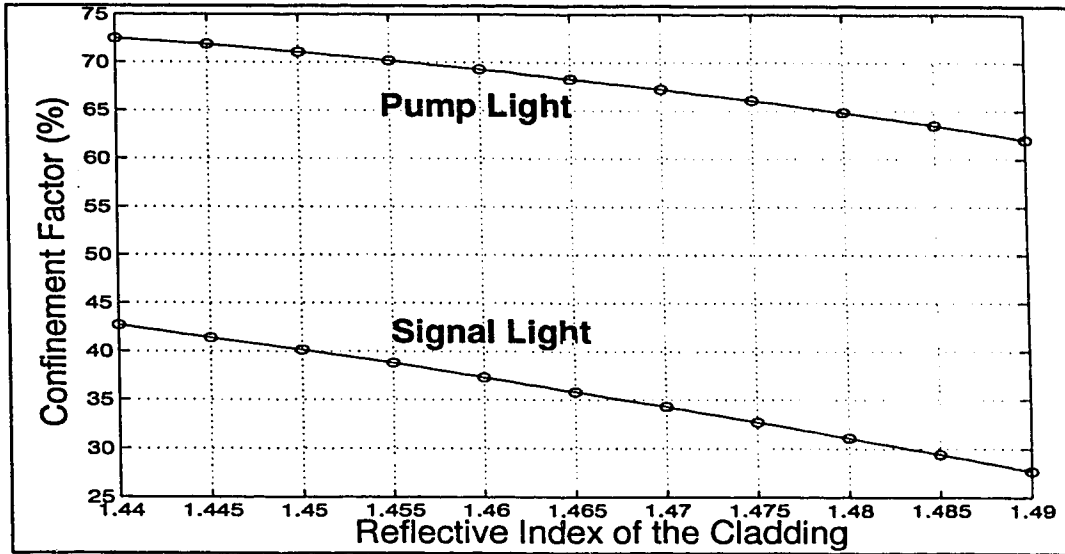


**Fig. 2.4.1.4 Confinement Factor versus  $N_{\text{clad}}$**

Another method of making large increases in the cladding index is by adding nitrogen during the deposition. The refractive index of the oxinitride, in theory, can be as high as the refractive index of the erbium-glass. Although the deposition of the material might be problematic, it is worthwhile to know how this change of cladding material affects both the confinement factor and the maximum core size. The results from SFEM are depicted in Fig. 2.4.1.5. It should be noted that the values of the confinement factors at each refractive index are calculated after the core height is increased to the maximum size for singlemode propagation at 980 nm. The change in confinement factors for both signal and pump light are about equal as the index increases. Only a 3% increase is observed as the index increases over the entire range. However, the maximum singlemode core height

increases rapidly as the cladding index increases. At an index of 1.56, the allowed singlemode core height increases by 115%. The increase in core size will provide more efficient light coupling. Thus, it is worthwhile to investigate the possibility of using silicon oxinitride as the cladding material.

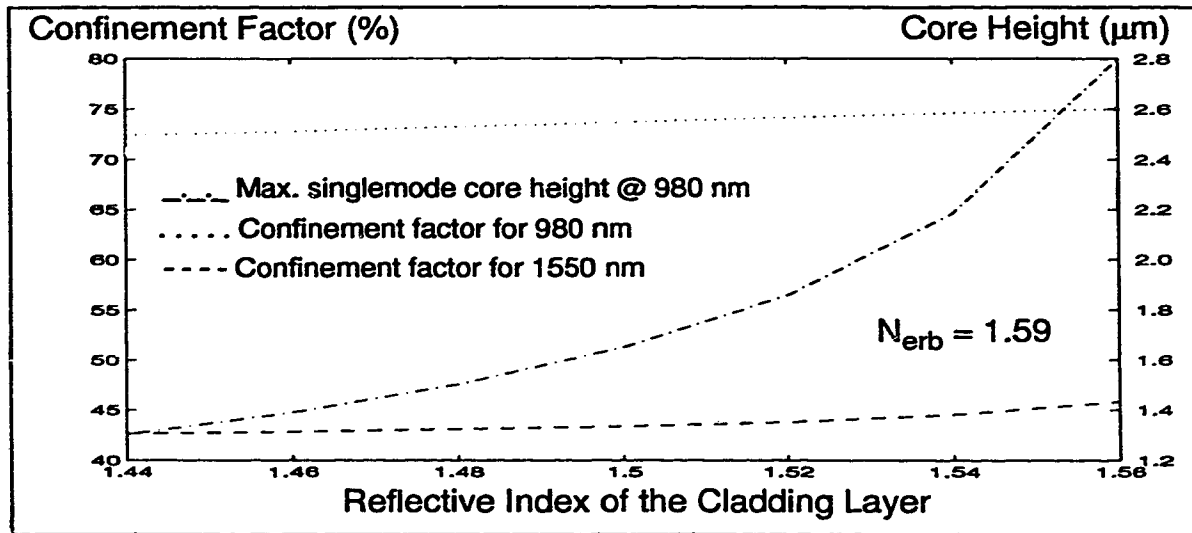


**Fig. 2.4.1.5 Core Height and Conf. Factor versus Refractive Index of the Cladding Layer**

The other factor that influences the performance of a v-groove amplifier is the surface curvature of the core, which for the erbium-doped glass, is mainly determined during the etching of the core. Fig. 2.4.1.6 shows the relation between the confinement factor and the depth of the crescent. The confinement factor drops at an approximate rate of 10% for every 10% increase in crescent depth. This result indicates that the mode is more confined with the flat core surface than with the curved surface. A 0.1 ratio of the crescent to the core height is assumed for all the above calculations to simulate the shape of the most recently fabricated waveguides.

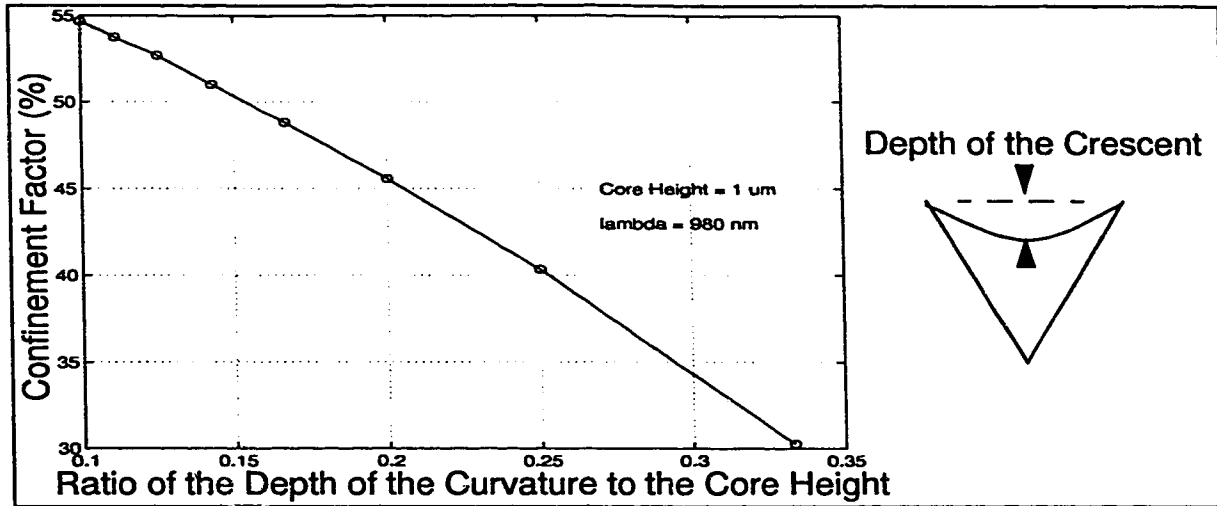


**Fig. 2.4.1.6 Conf. Factor versus the ratio of Crescent depth to the Core Height**

In addition to various fabrication considerations mentioned above, there is one major problem in fabricating erbium-doped waveguides. It is difficult to deposit more than a 2  $\mu\text{m}$  thick erbium-doped glass on the wafer. The fabrication of the erbium-doped core requires, first, the deposition of a thick layer of erbium-doped glass (usually 5  $\mu\text{m}$ ), and second, a reflow to flatten the deposited film. The desired core shape is obtained by etching away the excess material above the cladding surface using either wet or dry etch media. Although the singlemode core height is about 1  $\mu\text{m}$ , 5  $\mu\text{m}$  of material is required to ensure a flat surface for etching after the reflow (as shown in the above calculations). Therefore, the fabrication of the calculated core dimension might not be possible. Thus, other erbium-doped waveguide structures might be required. Fig. 2.4.1.7 shows some proposed waveguide structures.

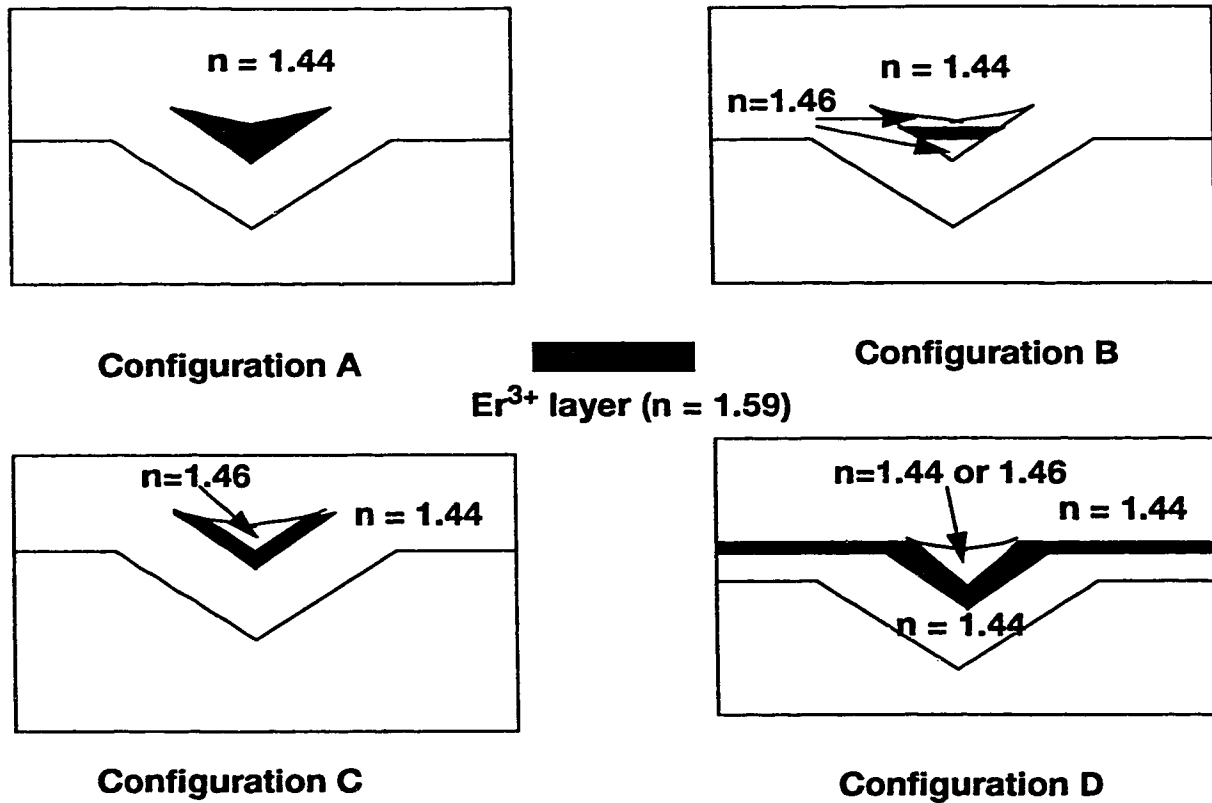


**Fig. 2.4.1.7 Different structures of the V-groove waveguide**

Waveguide A is the originally proposed structure, which in theory should have the highest gain efficiency due to its high confinement factors. Other structures will possibly have smaller confinement factors. In Waveguide B, only a strip of the erbium-doped glass is deposited into the core. The rest of the core is filled with borophosphorus-doped silicon-glass (BPSG) or silicon oxinitride which can have the same or smaller refractive index with the erbium glass. Several more masking procedures are required for this structure. Waveguide C is a modified version of B, which does not require many masking steps. The erbium glass is deposited prior to the core material. In this structure, the power confinement will be reduced even further. The reason is that the mode field is largely concen-

trated at the center of the v-groove, whereas the erbium layer is deposited along the sidewalls of the v-groove. Therefore, only a small amount of light power will overlap the erbium region in this design. Waveguide D is the simplest waveguide to make. The deposited erbium layer does not require the etch-back step. However, the mode shape of this configuration is not easy to predict; the confinement factor might drop even further. Also, if the core material is replaced by the cladding material to further simplify the fabrication process, the existence of the propagating mode is uncertain. The investigation of these configurations is presented in the following.

Fig. 2.4.1.8 shows the intensity contour plots of these designs. The core refractive index is set to 1.46 to simulate a BPSG core. The cladding index remains at 1.44. The wavelength is 980 nm. The core height is set to  $1\mu\text{m}$  to ensure all configurations are singlemode for comparison's sake. The thicknesses of the erbium layers for these waveguides are all  $0.17\mu\text{m}$ . The mode shape of waveguide B depicted in the figure is very similar to A, that is, the mode field is at maximum in the erbium layer. If the erbium layer is shifted in the vertical direction, the mode field would also be shifted accordingly. The mode shape of waveguide C is more triangular because of the erbium glass placement. Similarly, the contour plot of waveguide D shows that the mode field resembles the shape of the erbium layer. For waveguide D, a propagating mode does exist, even without filling in the silicon dioxide into the v-groove; however, the mode field spreads more into the cladding, which reduces the confinement factor further.

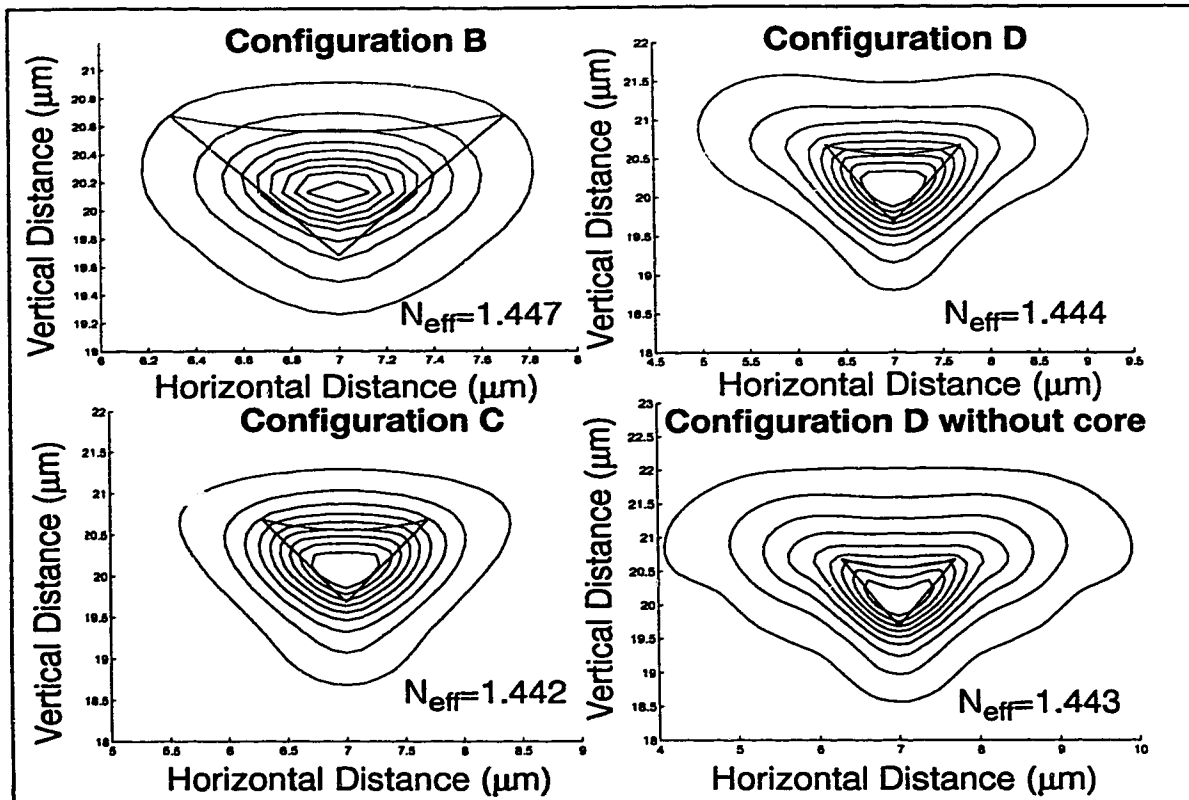


**Fig. 2.4.1.8 Intensity contour plots of various waveguide configurations**

The signal confinement factors of B and C are 13.1% and 4.3% respectively, whereas for D, the confinement factors are 5.6% and 4.5% for with and without the core filled. The confinement factor is still defined as the fraction of optical power confined in the erbium-doped layer. As expected, the confinement factors are reduced significantly in these configurations, especially for C and D. With these low confinement factors, it is questionable whether these waveguide structures can produce any reasonable gain. This will be explored in the next chapter.

### 2.4.2 Waveguides with polymer core

There are two ways of making polymer waveguides, either by direct dispensing

or by reactive ion etching (RIE). The details of these two fabrication methods will be presented in Chapter 4. This section is concerned with the maximum core size that can have singlemode propagation. The confinement factor is less important for the polymer waveguide.

Since the waveguide will be tested with the 632.8 nm helium neon laser, the waveguide will be designed to be singlemode at this wavelength. The available refractive index of the polymer is either 1.54 or 1.56, which can be used as cladding and core material. The proposed polymer waveguide consists of silicon-dioxide lower cladding, polymer core with 1.56 refractive index, and either air or lower index polymer as the upper cladding. From the above discussion of erbium waveguides, it is expected that the singlemode core size of the polymer waveguide with polymer upper cladding is larger than that of the erbium amplifier, since the index difference is smaller. Similarly, the core size is expected to be significantly smaller for the air upper cladding.

In practice, the core height of both dispensed and RIE waveguide cannot be fabricated less than 1  $\mu\text{m}$ . Therefore, it might not be possible to produce a singlemode waveguide with air as the upper cladding. Moreover, for the dispensed waveguide, it is not certain whether a core of a few microns wide can be filled with polymer without overflowing onto the surface of the wafer, since the smallest syringe tip diameter is 19  $\mu\text{m}$ . If overflowing does occur, the resulting waveguide will be similar to an inverted ridge-loaded waveguide as shown in Fig. 2.4.2.1. The thickness of the thin film layer is determined by the viscosity of the polymer. If the film is thin enough, the waveguide can be singlemode with core height bigger than 1  $\mu\text{m}$ . These concerns will be analysed below.

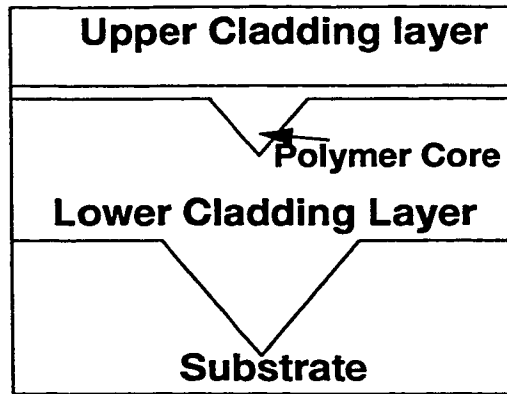


**Fig. 2.4.2.1 Thin-film V-groove waveguide**

With upper cladding filled with 1.54-index polymer and no assumed overflow, the maximum allowed core height is about  $3.0\ \mu\text{m}$ . The mode shape is similar to that of the erbium amplifier except that the mode is slightly shifted toward the upper cladding, as shown in Fig. 2.4.2.2. If the polymer cladding is replaced by air, five propagating modes will exist, as shown in Fig. 2.4.2.3, even if the core height is reduced to  $2\ \mu\text{m}$ . If the core height is reduced to  $1\ \mu\text{m}$ , the first 3 modes will still exist. Even if the lower cladding index increases to 1.46, there still exists more than one mode in the waveguide. This suggests that a singlemode polymer waveguide requires an upper polymer cladding. Nevertheless, the optical power carried in the second and third modes shown in Fig. 2.4.2.3 would possibly be greatly attenuated during the propagation. The attenuation is due to these two modes being located near the interface between the core and the lower cladding which has a rough surface that causes scattering (More details about the cladding roughness are given in Chapter 4). Moreover, the shapes of these two modes are very different from the fiber mode, which is circular and larger. Thus the efficiency of exciting these two modes is much smaller than the fundamental mode. Therefore, the fabricated polymer



waveguide might still be effectively singlemode.

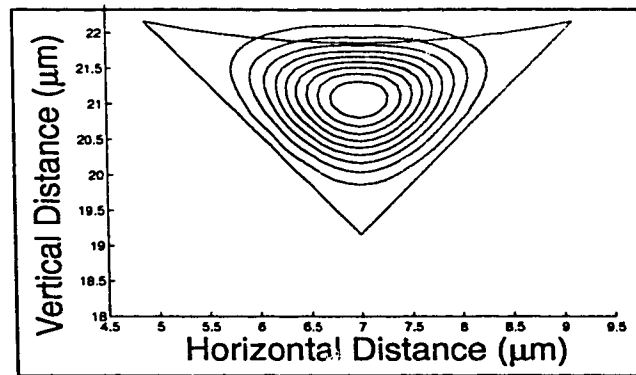


**Fig. 2.4.2.2 Contour Plot of the fundamental mode of the polymer waveguide with upper cladding**

If the overflowing condition is considered, 3 modes will exist for the 3.0 μm core height with upper polymer cladding as shown in Fig. 2.4.2.4, even though the thin film is only 0.1 μm thick. For the limiting case, where the core height is 1 μm, the polymer does become singlemode, with the thin-film thickness of 0.6 μm. However, the number of modes is very sensitive to the thin-film thickness. An increase of 0.1 μm in thickness causes 3 modes to appear. If the polymer upper cladding is not deposited, it will be singlemode only if the thin film is 0.2 μm thick with 1 μm core height. Based on these results, the waveguide cannot tolerate any overflowing. Since this is difficult to avoid, the dispensed waveguide is most likely to be multimode.

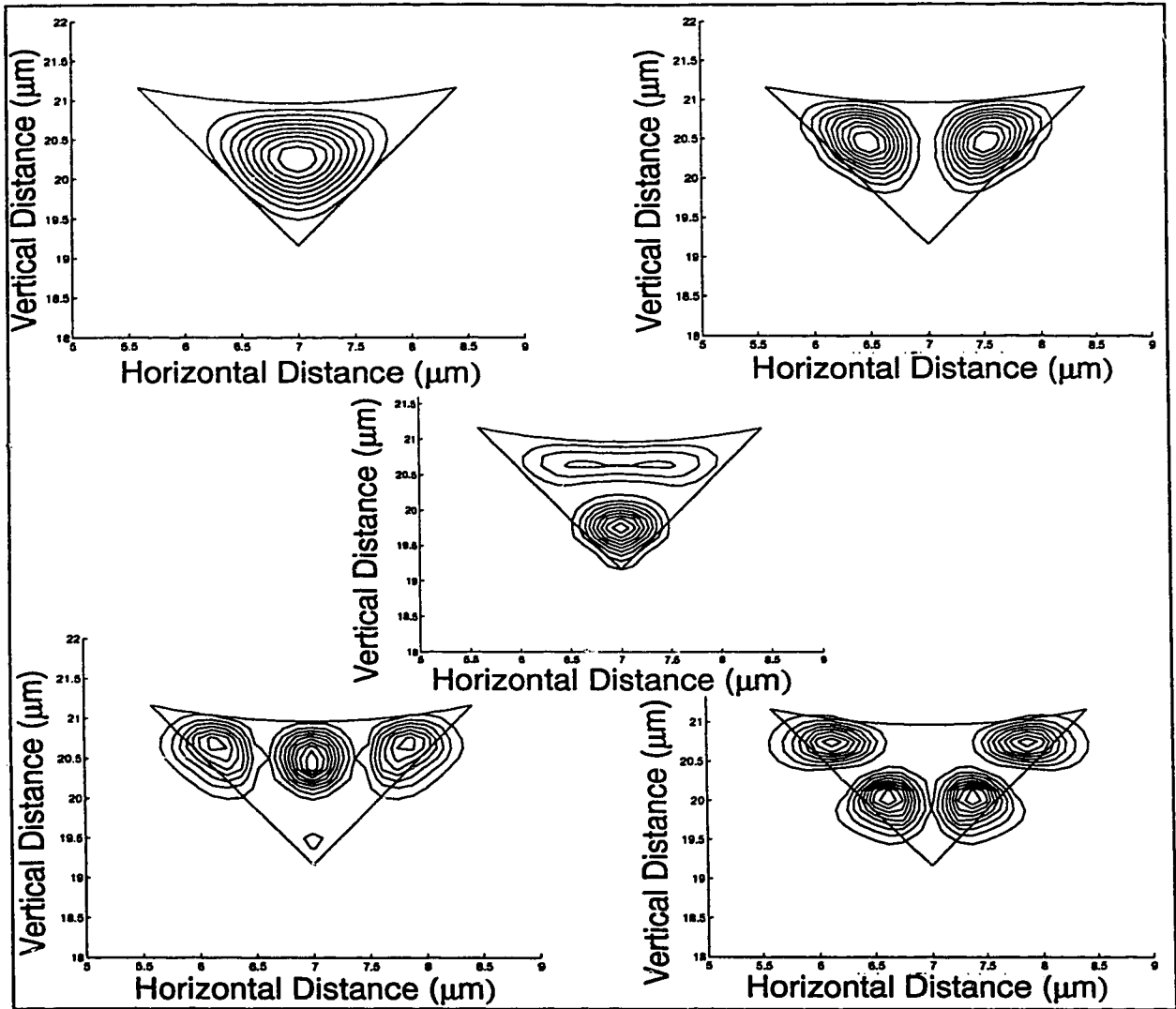


**Fig. 2.4.2.3** Five different modes in a 2  $\mu\text{m}$  polymer waveguide without upper cladding

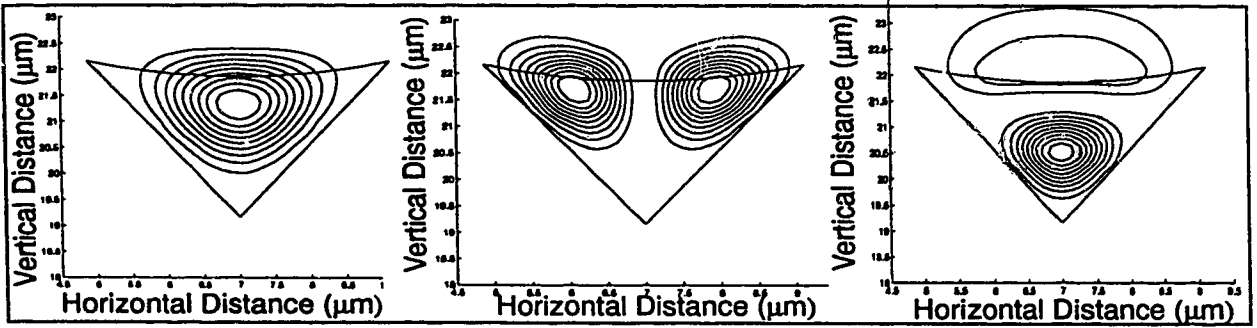


**Fig. 2.4.2.4** 3 modes for the overflowed polymer waveguide

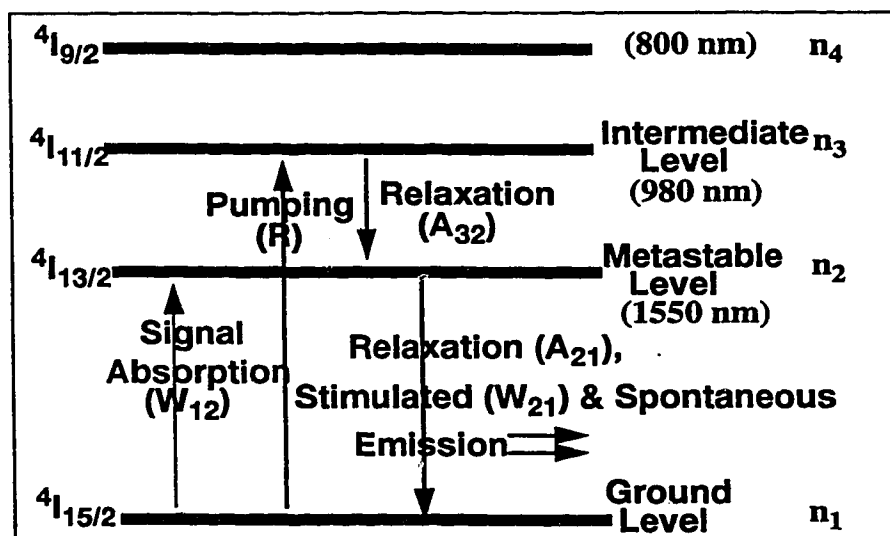
## Chapter 3 Optical Amplifier Simulations

### 3.1 Background Theory for the Optical Amplifier

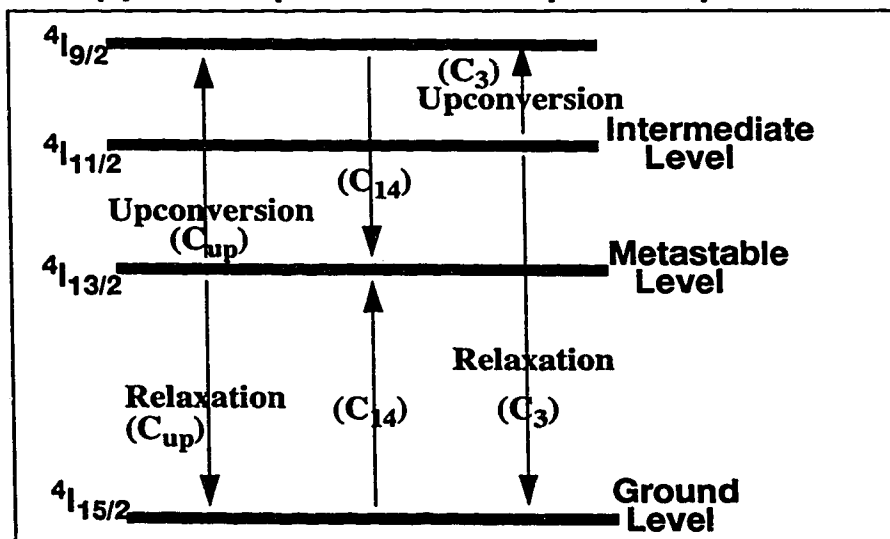
The behavior of the optical amplifier is governed by various optical and electrical characteristics of the active ions, such as transition cross sections, spectral shape of the emission and absorption bands, excited state lifetimes, ion-ion interactions, as well as static and dynamic ion-lattice interactions [20]. The major activities occurring during the operation of the erbium amplifier are illustrated graphically in Fig. 3.1.1.

The basic operations of the amplifier are shown in Fig. 3.1.1 (a). The erbium ions are first pumped from the ground level to the intermediate level by absorbing the photon energy of the pumping light. In the erbium amplifier, the pump wavelength is 980 nm. The activated ions then fall rapidly and nonradiatively into the metastable level, in which the ions will stay for a relatively long period of time (typically on the order of milliseconds). The erbium ions will then return back into the ground level both radiatively and nonradiatively. The nonradiative transition is referred to as relaxation, which is the result of the interaction between the electrons and the dynamic lattice [20]. The radiative transition includes both stimulated and spontaneous emissions. The stimulated emission happens when a photon with energy matching with the energy difference between the two levels stimulates a downward transition of an ion in the metastable level ( ${}^4I_{13/2}$ ) into the ground state, causing the emission of another photon into the same electromagnetic mode [28]. This is the only transition that contributes to the actual gain. The spontaneous emission does not require any external stimulation and the probability of this transition depends on the transition cross section and the metastable lifetime. The spontaneous emission is the

major contributor to the noise of the amplifier. An efficient amplifier requires the erbium ions stay in the metastable level as long as possible, so that a high ion population inversion in the metastable level can be achieved and hence the signal photons can have a higher probability to stimulate the activated ions.



(a) Basic Operation of the optical amplifier



(b) Upconversion Phenomenon

**Fig. 3.1.1 Four-level energy model for Optical Amplifier (the symbols in the parentheses corresponds to the variables in the equations that described the amplifier model)**

There are several mechanisms that may reduce the population inversion. One of them is the nonradiative transition mentioned previously. Another mechanism is known as the excited-state absorption (ESA), in which the metastable ions absorb either signal or pump photons and jump to even higher energy levels. ESA happens only if there exists an energy level in which its energy equals to the sum of the energy in the metastable level and the absorbed photon energy. Even if an ion returns to the metastable level, the absorbed photon energy will be lost through heat or spontaneous emission at an undesired wavelength [20]. The third mechanism is related to ion-ion interactions, which is believed to be the major factor that reduces the amplification efficiency at a high concentration. The ion-ion interactions can be due to the high concentration and the non-uniform distribution of the erbium ions called clustering [15]. In some cases, the ions are close enough to interact in pair, and the energy of one ion is absorbed by the other one. As a result, one ion jumps to the fourth energy level ( $4I9/2$ ) and the other one falls to the ground state. This process is called cooperative upconversion. The promoted ion will eventually return to the metastable level, and the net result is the loss of one photon. Fig. 3.1.1 (b) illustrates this upconversion. Much research [20] has been conducted to seek possible ways to reduce this concentration quenching. One method is to codope the host glass with Al to increase the solubility of the erbium. Since Al is soluble in silica glass and erbium is soluble in Al, the Al acts as a bridge to incorporate the erbium ions into the silica network [18],[20].

In the past few years, many researchers have attempted to accurately model the complex activities in the amplifier [29]-[32]. The model used in this research is based on the latest four-level energy model[32]. In the mechanisms described above that reduce

population inversion, only ESA is not included in this model. The rate equations that describe this model are presented below:

$$\begin{aligned} \frac{\partial n_1}{\partial t} = & -W_{12}n_1 - Rn_1 + A_{21}n_2 + W_{21}n_2 + C_{up}n_2^2 \\ & - C_{14}n_1n_4 + C_3n_3^2 \end{aligned} \quad (3.1)$$

$$\begin{aligned} \frac{\partial n_2}{\partial t} = & W_{12}n_1 - A_{21}n_2 - W_{21}n_2 + A_{32}n_3 + 2C_{14}n_1n_4 \\ & - 2C_{up}n_2^2 \end{aligned} \quad (3.2)$$

$$\frac{\partial n_3}{\partial t} = Rn_1 - A_{32}n_3 + A_{43}n_4 - 2C_3n_3^2 \quad (3.3)$$

$$\frac{\partial n_4}{\partial t} = C_{up}n_2^2 - C_{14}n_1n_4 - A_{43}n_4 + C_3n_3^2 \quad (3.4)$$

where  $n_1$ ,  $n_2$ ,  $n_3$  and  $n_4$  are the ion population densities in the levels  ${}^4I_{15/2}$ ,  ${}^4I_{13/2}$ ,  ${}^4I_{11/2}$  and  ${}^4I_{9/2}$  respectively;  $W_{12}$ ,  $R$  and  $W_{21}$  are the signal absorption, pump absorption, and emission transition rates,  $A_{21}$  is the spontaneous transition rate,  $A_{32}$  and  $A_{43}$  are the nonradiative relaxation rates, and  $C_{up}$ ,  $C_3$  and  $C_{14}$  are the upconversion and cross-relaxation coefficients. It should be noted that in the above equations,  $n$ ,  $W_{12}$ ,  $W_{21}$  and  $R$  are functions of  $x$ ,  $y$  and  $z$ ; they are not shown in the equations for the sake of simplicity. The number of ions that is upconverted to other higher levels such as  ${}^4f_{7/2}$  is assumed to be negligibly small. In the steady-state condition, the population densities  $n_1$ ,  $n_2$ ,  $n_3$  and  $n_4$  are computed by setting the left side of the equations to zero and using the conservation law:

$$n_1 + n_2 + n_3 + n_4 = n_T \quad (3.5)$$

where  $n_T$  is the erbium concentration which is assumed to be spatially independent. The

steady-state profile of the signal, pump and amplified spontaneous emission powers,  $P_p$ ,  $P_s$  and  $P_{ase}$ , are described by the propagation equations.

$$\frac{d}{dz}P_p(z) = -\gamma_p(z)P_p(z) \quad (3.6)$$

$$\frac{d}{dz}P_s(z, \nu_s) = [\gamma_{21}(z, \nu_s) - \gamma_{12}(z, \nu_s)]P_s(z, \nu_s) \quad (3.7)$$

$$\frac{d}{dz}P_{ASE}(z, \nu_j) = \pm[\gamma_{21}(z, \nu_j) - \gamma_{12}(z, \nu_j)]P_{ASE}(z, \nu_j) \pm m h \nu_j \Delta \nu_j \gamma_{21}(z, \nu_j) \quad (3.8)$$

with boundary conditions:

$$P_p(0) = P_{p0} \quad (3.9)$$

$$P_s(0, \nu_s) = P_{s0}(\nu_s) \quad (3.10)$$

$$P_{ASE+}(0, \nu_j) = P_{ASE-}(L, \nu_j) = 0 \quad (3.11)$$

$j=1, M$

where  $M$  is the number of frequency slots used to model the amplified spontaneous emission and  $\nu_j$  is the frequency at the  $j^{\text{th}}$  slot; the coefficient  $m$  in (3.8) represents the number of guided modes propagating at signal wavelength. The absorption and emission coefficients  $\gamma_p, \gamma_{12}$  and  $\gamma_{21}$  in (3.6)-(3.8) are spatially integrated expressions which depend on the normalized pump and signal intensity profiles  $\psi_p(x, y), \psi_s(x, y)$ , and the absorption and emission cross sections,  $\sigma_{a13}, \sigma_{a12}, \sigma_{e21}$  as follows:

$$\gamma_p(z) = \iint_A \psi_p(x, y) \sigma_{a13} n_1(x, y, z) dx dy \quad (3.12)$$

$$\gamma_{12}(z, \nu_i) = \iint_A \psi_s(x, y) \sigma_{a12}(\nu_i) n_1(x, y, z) dx dy \quad (3.13)$$

$$\gamma_{21}(z, \nu_i) = \iint_A \psi_s(x, y) \sigma_{e21}(\nu_i) n_2(x, y, z) dx dy \quad (3.14)$$

where  $A$  is the cross-sectional area of the active region. As shown in the above equations, the value of the  $\gamma$ 's depend on the normalized intensity, which in turn depend on the opti-

cal power. The normalized pump and signal intensity can be obtained from the mode field intensity calculated from the modal analysis.

In this model, the output pump and signal power can be calculated. Also the amplified spontaneous emission power spectrum can be obtained. The input signal and pump light is assumed to be polarized in x-direction.

### 3.2 Brief Description of the Simulation

A C program was written to simulate the gain profile of the erbium waveguide. This program is based on the four-energy-level model described in the previous section. The simulation is divided into three main parts. The first part of the simulation calculates the erbium ion densities at all four energy levels for each finite element by solving (3.1) to (3.4), with each  $\frac{dn}{dt} = 0$ . In order to solve these equations, the program is required to first calculate  $W_{12}, W_{21}$  and  $R$ . To calculate these three parameters, the program is required to know the mode field distribution and input optical power at both pump and signal wavelengths. The input mode fields are calculated from the modal analysis presented in the last chapter. The optical power is specified by the user. Once these parameters are calculated, (3.1) to (3.4) are solved by the multi-variable Newton-Raphson method [41]. The second part of the simulation calculates the absorption and emission coefficients according to (3.12)-(3.14). The integrations in these equations are calculated numerically. The  $\sigma$ 's and ion densities (calculated in the first part) are assumed constant in each finite element. To reduce the computation time, the normalized intensity is also assumed constant in each element, the value being calculated by taking the average of the values at the three vertices of the element. The integration for each element is simply  $(\psi\sigma n)\Delta A$ , where  $\Delta A$  is the area



of the element. Once  $\gamma$ 's are obtained, the program proceeds to the last part of the simulation which calculates the optical power for signal, pump and amplified spontaneous emission at the next position in the propagation direction according to (3.6)-(3.8). These first-order differential equations are approximated by the 4th order Runge-Kutta method [41] but assuming the  $\gamma$ 's are constant. Once the optical power of the next position is calculated, the program can repeat the three-part simulation for each point in the entire waveguide. The program then checks if the boundary conditions in (3.11) are satisfied. If not, the program adjust initial values of the antipropagant ASE spectrum at the input end of the waveguide and repeats the entire simulation until the boundary conditions are met. The ASE boundary conditions are adjusted using the bisection method; therefore the user is required to specify both an upper limit (used in the first iteration) and a lower limit (second iteration) for the bisection method. A brief description of the program can be found in Appendix B.

The values of the parameters used in the program are listed in Table 3.2.1. These values are taken from [31,32]. It should be noted that although the upconversion coefficients depend on the concentration of the erbium [34], some experiments have shown that the energy transfer rates are constant [35]; thus all C's are assumed constant. Also, because of the lack of any experimental values,  $C_3$  and  $C_{14}$  are theoretically calculated. Moreover, the chosen emission and absorption cross-section spectra are typical for the erbium-doped silica materials as shown in Fig. 3.2.1 [31]. The spectrum considered ranges from 1.419  $\mu\text{m}$  to 1.654  $\mu\text{m}$ . The spectrum is divided into 64 wavelength slots of width  $\Delta\lambda$

of 3.67 nm to perform the simulation.

**Table 3.2.1 Parameters of the Amplifier Simulation**

Parameter	value
$A_{21}$	90.0/s
$A_{32}$	1.0e9/s
$A_{43}$	1.0e9/s
$C_{up}$	5.0e-23m <sup>3</sup> /s
$C3$	5.0e-23m <sup>3</sup> /s
$C_{14}$	3.5e-23m <sup>3</sup> /s
$\sigma_{e21}(1.531 \mu\text{m})$	5.41e-25m <sup>2</sup>
$\sigma_{a12}(1.531 \mu\text{m})$	5.36e-25m <sup>2</sup>
$\sigma_{a13}(0.98 \mu\text{m})$	2.58e-25m <sup>2</sup>

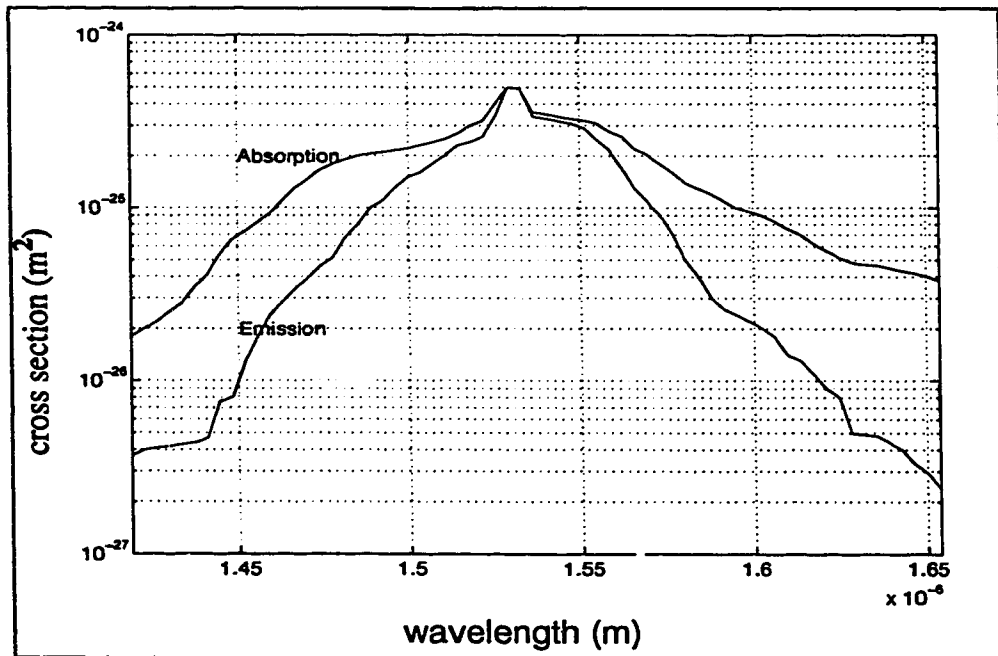


**Fig. 3.2.1 Emission and Absorption cross-section spectra.**

### 3.3 Simulation Results and Discussion

The core height of the waveguide is set to  $1.30\ \mu\text{m}$  and the entire core is filled with erbium glass to estimate the maximum performance of the amplifier. The refractive indices of the core and cladding layer are 1.59 and 1.44 respectively. Fig. 3.3.1 shows the gain characteristics of the amplifier as a function of the erbium concentration for a waveguide length of 4 cm. The signal power is set at  $1\ \mu\text{W}$  for the entire analysis. The signal gain curves at two pump power levels, with and without upconversion, are plotted on the graph. The simulation results show that if upconversion is not considered, the signal gain would increase directly proportional to the waveguide length at both pump levels. Also, the graph shows that the 10 mW pump power already saturates the signal gain. With the upconversion considered, at 10 mW pump power, the gain peaks at  $1 \times 10^{26}$  ions/ $\text{m}^3$  concentration and declines beyond this concentration, and loss appears as the concentration reaches  $2.4 \times 10^{26}$  ions/ $\text{m}^3$ . More signal photons are absorbed by the erbium than are produced from the stimulated emission. This shows that the upconversion has a strong effect at high concentration at this pump level. Large numbers of metastable erbium ions are being upconverted and cross-relaxed to higher levels and the ground state level respectively. As a consequence, the population inversion in the metastable level is reduced significantly.

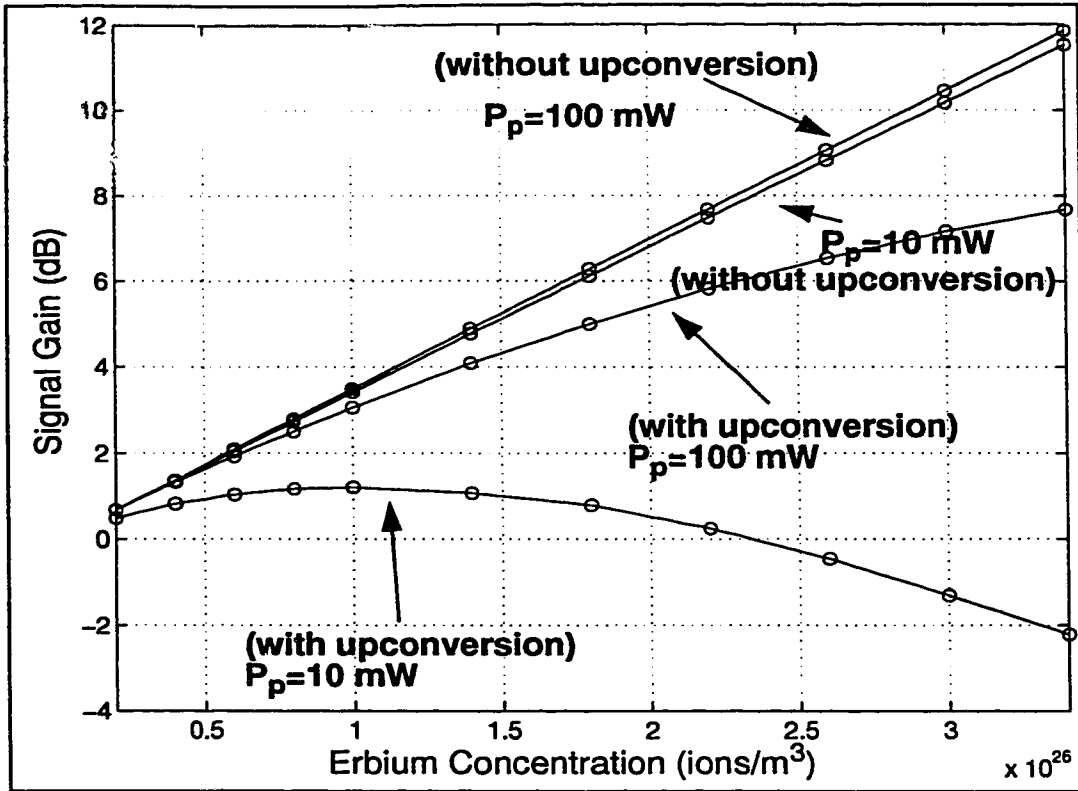


**Fig. 3.3.1 Signal Gain versus Erbium Concentration at two pump levels.**

The effect of upconversion can be compensated by increasing the pump level, which increases the number of ions in the metastable level. At 100 mW, the curve in Fig. 3.3.1 shows that the effect of the upconversion is suppressed at even  $3.4 \times 10^{26}$  ion/m<sup>3</sup> for which a detailed explanation will be presented later. At  $3.0 \times 10^{26}$  ions/m<sup>3</sup>, the signal gain is about 7.2 dB. This shows that the  $3.0 \times 10^{26}$  ions/m<sup>3</sup> erbium glass being used in the amplifier fabrication is adequate for the 100 mW laser pumping.

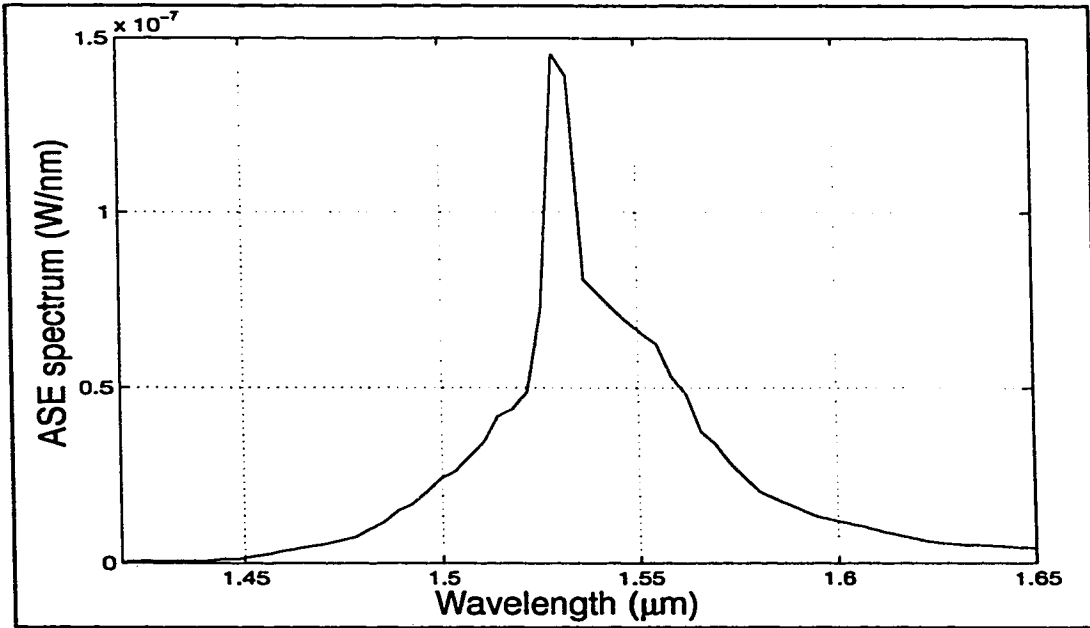


**Fig. 3.3.2 The Output spontaneous emission spectrum at  $3 \times 10^{26}$  ions/m<sup>3</sup>**

The corresponding output amplified spontaneous emission noise power (Pase) spectrum is shown in Fig. 3.3.2. The total spontaneous noise power equals the area under this spectrum and is about 5.7 μW (close to the signal power). This noise power can be reduced by filtering at the output of the amplifier. Using the Pase spectral density value at 1.531 μm and a reasonable optical bandwidth of 1 nm [42], the actual output spontaneous noise would be approximately 0.15 μW. This corresponds to an optical signal-to-noise ratio (SNR) at the output of the amplifier of 15 dB. This optical SNR value does not really reflect the actual SNR at the receiver, because the SNR at the receiver would be affected by other noise as well; therefore, it is more important to know how the ASE noise actually contributes to the total noise at the receiver. Olsson has theoretically calculated the noise power at the receiver of a 5 Gbit/s transmission system with an optical amplifier acting as a preamplifier [42]. His simulation results show that for signal gain less than 15 dB, the

dominant noise at the receiver is the thermal noise, and the receiver sensitivity increases proportionally to the signal gain. For the erbium-doped v-groove waveguide, the signal gain appeared at the receiver would be about 7.2 dB assuming 100% signal coupling efficiency at both input and output ends. Thus, the thermal noise would dominant and the ASE noise would not contribute significantly to the total noise power at the receiver.

Fig. 3.3.4 shows the signal gain profile along the waveguide at two different pump levels; the erbium concentration is set at  $30 \times 10^{25}$  ions/m<sup>3</sup>. At 100 mW pump level, the signal power increases almost linearly as it propagates. The signal gain is about 1.8 dB/cm. At 10 mW, the gain curve has a concave shape, the signal has a little gain at the beginning then it starts to decline. This behaviour is explained in Fig. 3.3.5.

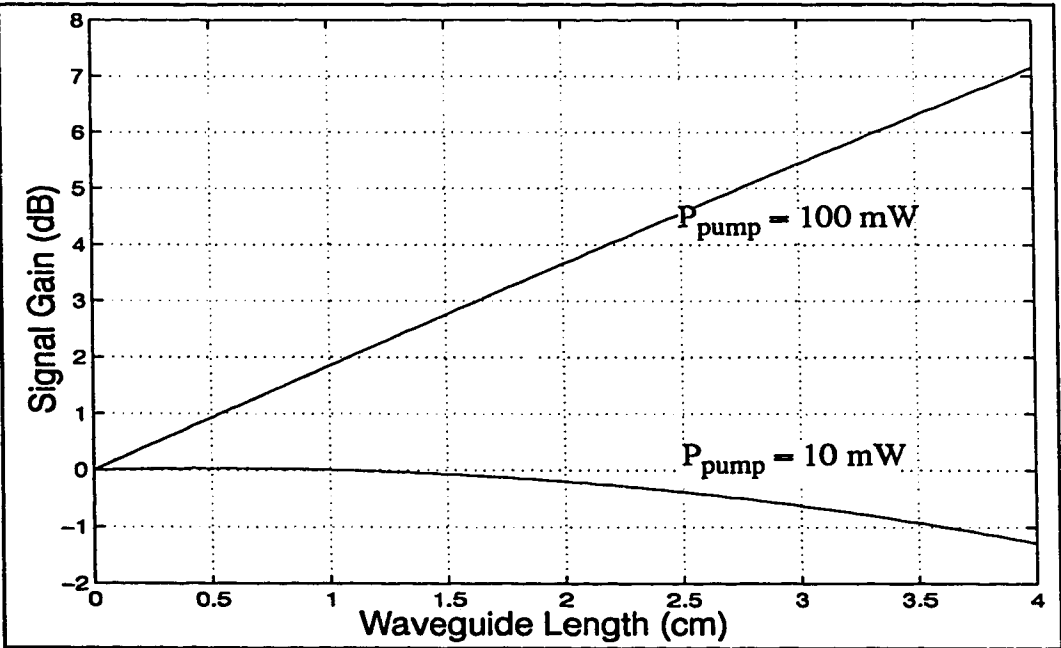


**Fig. 3.3.3 Signal Gain versus propagating distance at two pump level.**

It is evident from Fig. 3.3.5 that the pump power is depleted significantly as it propagates through the waveguide. At about 0.6 cm, the graph shows that  $\gamma_{12}$  equals  $\gamma_{21}$ ,

which indicates that the number of ions in the metastable level almost equals the number of ions in the ground level. The signal gain can be obtained only if  $\gamma_{21}$  is larger than  $\gamma_{12}$ . At 0.6 cm, the pump photons can barely pump enough ions into the metastable level to yield sufficient population inversion to produce stimulated emission which compensates for the loss of photons due to upconversion and spontaneous emission. Further from the input end, the pump power can no longer compensate the loss. The signal loss starts to appear at about 1 cm. In order to obtain signal gain throughout the waveguide, the pump power must be increased to a level that the depletion will not be very significant. In other words, with the energy loss from the upconversion and relaxation, the pump light must still provide enough energy to achieve sufficient or excess amount of population inversion so that the number of photons produced by stimulated emission can increase as the number of signal photons increases along the entire waveguide. The minimum value of this required pump power is found from Fig. 3.3.6.

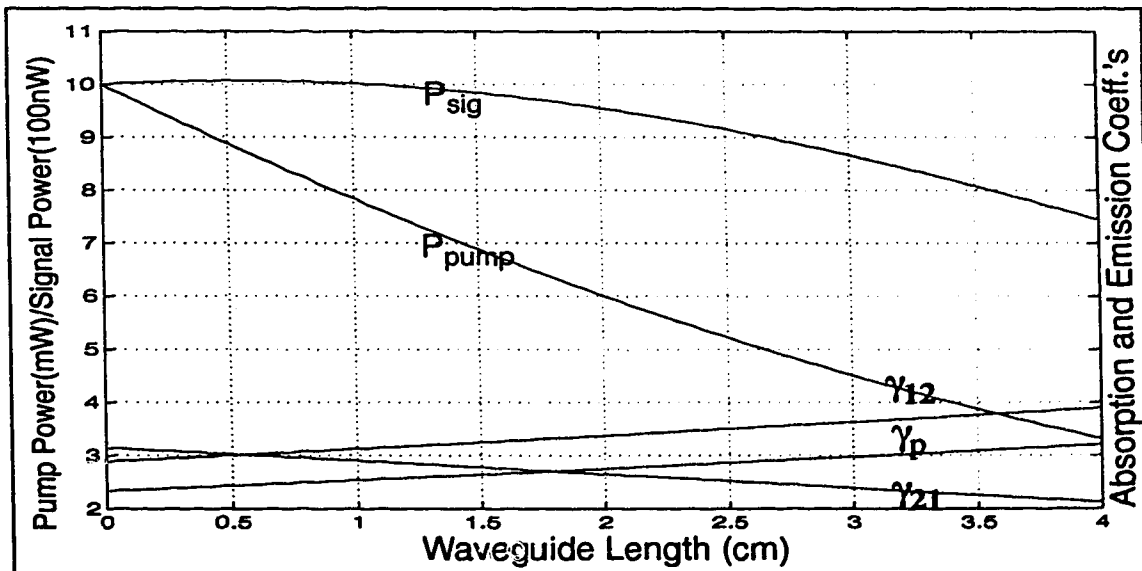


**Fig. 3.3.4 Signal and Pump powers and emission and absorption constants in a 4 cm waveguide**

Fig. 3.3.6 shows the signal gain of a 4 cm long waveguide at different pump levels. The erbium concentration is set at  $30 \times 10^{25}$  ions/m<sup>3</sup> and will be fixed at this value for the rest of the analysis. It can be seen from the figure that the gain curve rises rapidly at the beginning, then levels off and approaches a limit value. Clearly at low pump power, the number of ions in the metastable level is not enough to produce a sufficient number of stimulated emissions to compensate the number of signal photons loss in the absorption. This implies that a good number of metastable-level ions pumped by the pump power are lost in the upconversion, and population inversion is insufficient. The upconversion effect becomes less significant as the pump power increases beyond 100 mW. This shows that the upconverted ions from the metastable level do not affect the population inversion significantly. It should be mentioned at this point that if the waveguide length is allowed to be sufficiently long, the signal gain at any pump power will climb to a maximum point before declining as the signal propagates through the waveguide. For an optimal fixed-length waveguide amplifier, the pump power should be set at a level such that at the end of the waveguide the signal gain is at the maximum point. Fig. 3.3.7 shows the gain profile at various pump levels. The optimal pump power appears to be about 20 mW at this waveguide length. Nevertheless, this optimal pump power does not provide the maximum achievable gain but rather the maximum gain efficiency, defined as the gain in dB per mW of pump power. The maximum achievable gain is close to 9.5 dB. If the pump power can be increased without limit, it should be increased until the change of the achievable gain is very close to saturation as shown in Fig. 3.3.7. This particular pump level should be at the knee of the gain curve in Fig. 3.3.6, which is about 100 mW. The shortcoming of this large pump power is that the gain efficiency is relatively low as shown in Fig. 3.3.8. At the opti-



mal 20 mW pump power, the efficiency is about 0.11 dB/mW; at 100 mW, the efficiency drops to about 0.05 dB/mW.

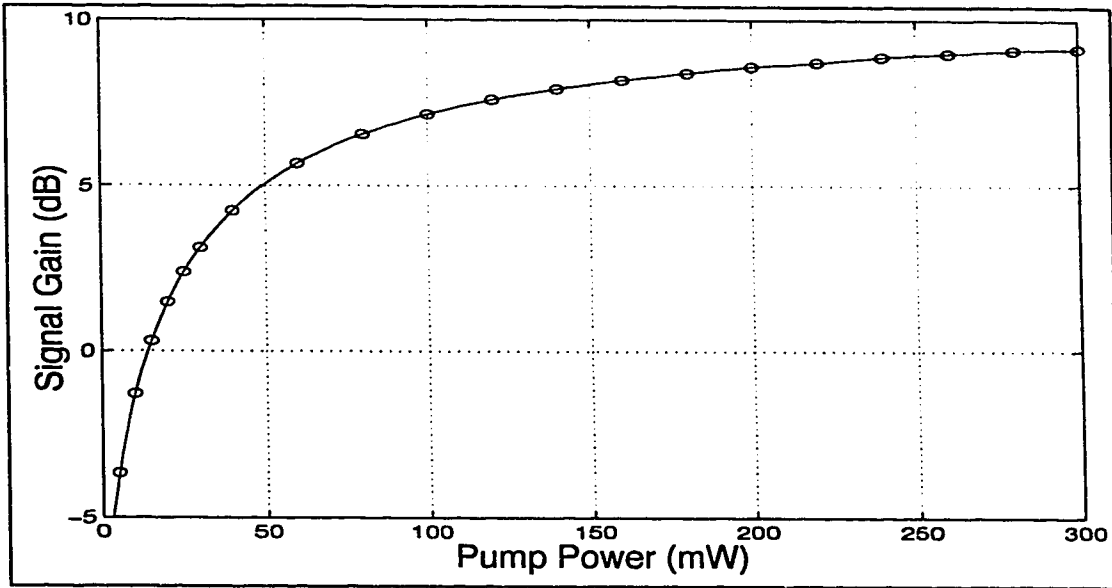


**Fig. 3.3.5 Signal Gain versus Pump power**

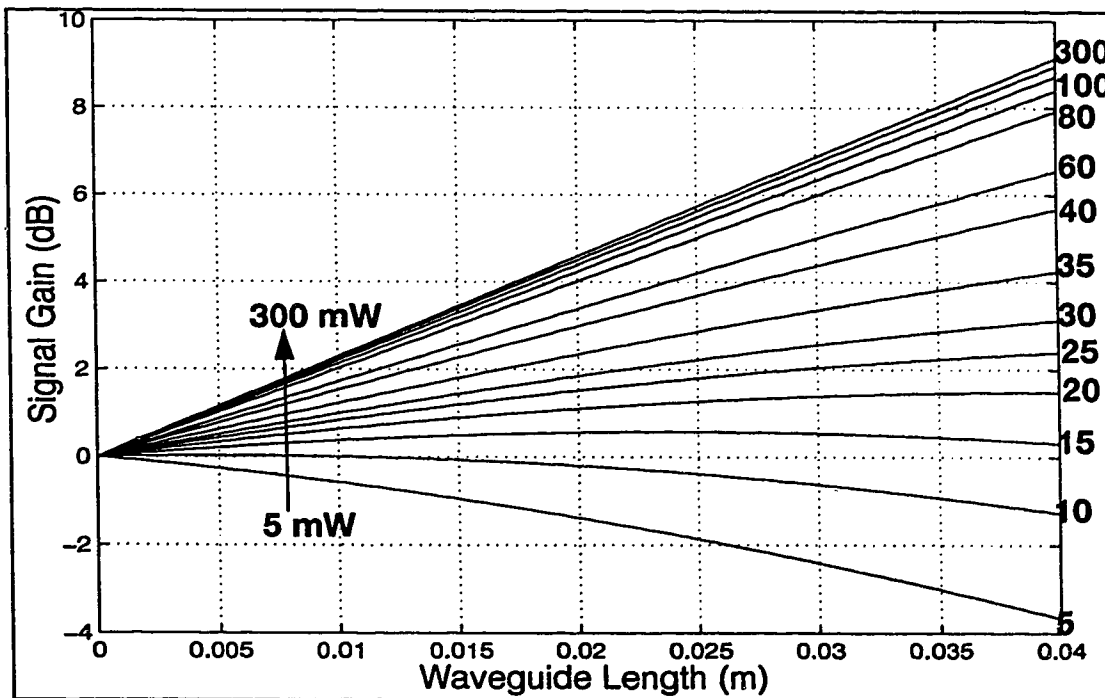


**Fig. 3.3.6 Gain Profiles at different pump levels**

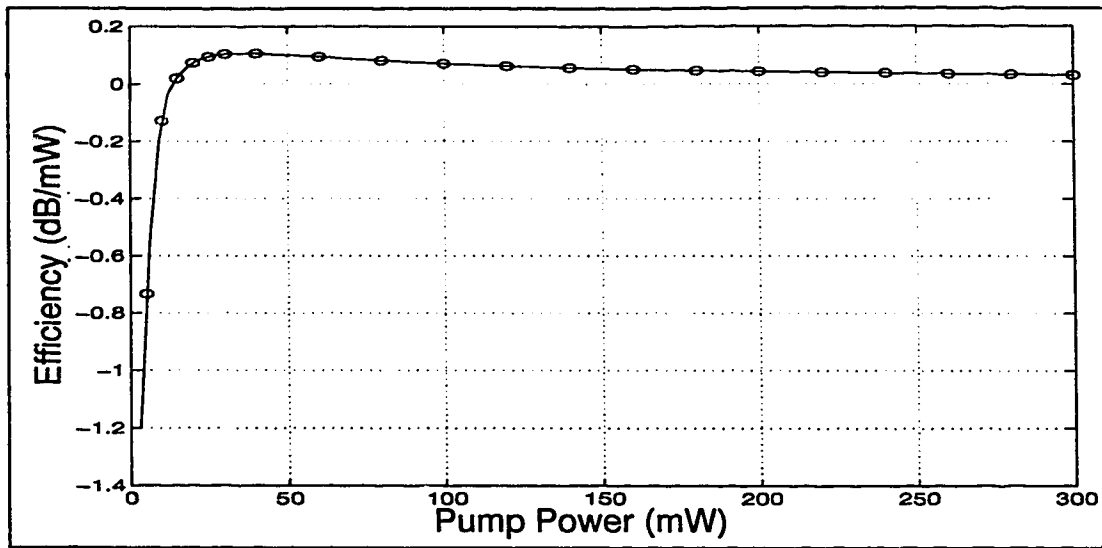


**Fig. 3.3.7 Gain Efficiency versus Pump Power**

In addition to the erbium concentration and the pump power, a crucial parameter that affects the signal gain is the core size. Fig. 3.3.9 shows how the change of the core height affects the signal gain. Evidently, the signal gain decreases dramatically as the core size is reduced. The gain at 1.1  $\mu\text{m}$  core height is reduced by about 32% from the maximum value. This large gain decrement is expected because the confinement factors of both signal and pump light decrease rapidly as the core height decreases. Also, the smaller core area contains fewer erbium ions. Since the width and the height of the core have a fixed ratio, the cross-sectional area of the core would be proportional to the square of the core height. The area of the core with 1.1  $\mu\text{m}$  core height is 72% of the area of the core with 1.3  $\mu\text{m}$  core height; this implies that the number of erbium ions in the core are also decreased by 28%. If the core height is reduced to 0.9  $\mu\text{m}$ , the gain is about 2.5 dB in a 4 cm long waveguide. In practice, the coupling and waveguide losses can easily add up to 2.5 dB; therefore, at this core size, the active waveguide acts more like a transparent waveguide. A

longer waveguide length is required in order to obtain any reasonable gain. If the core height varies between 0.9 to 1.3  $\mu\text{m}$  during the fabrication, the signal gain will range from 2.5 dB to 7.2 dB.

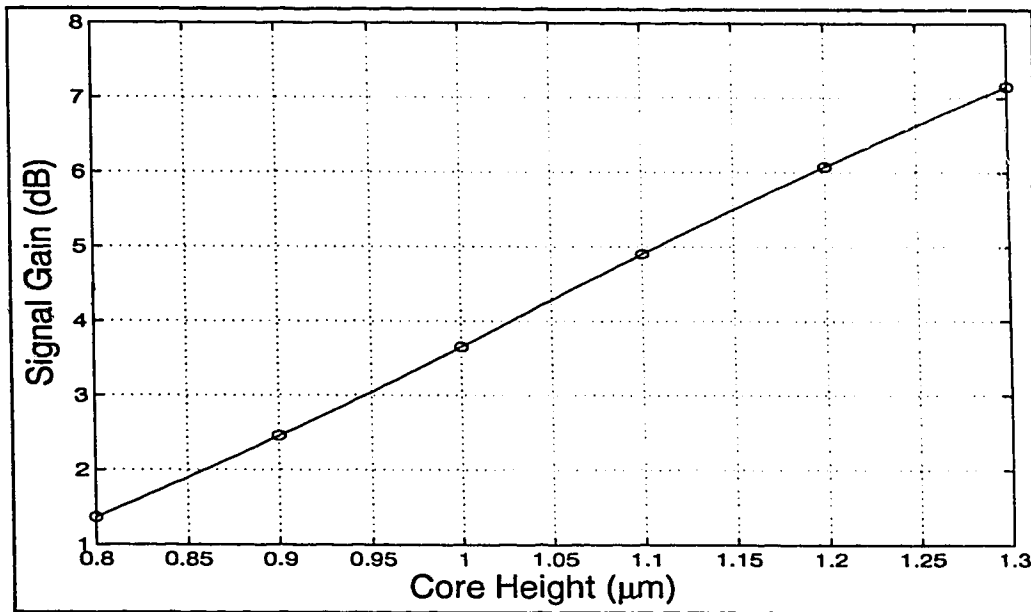


**Fig. 3.3.8 Signal Gain versus Core Height**

Fig. 3.3.10 shows the gain profile of the other three waveguide structures. The core height of these waveguides is set at 1.5  $\mu\text{m}$ . The thickness of the erbium layer is set at 0.25  $\mu\text{m}$ . The pump level is 100 mW. The achievable gains are 2.9 dB, 0.45 dB and 0.20 dB for structures B,C and D respectively (assuming Waveguide D has the v-groove filled with BPSG of 1.46 refractive index). All three curves display a linear profile, indicating that the waveguide length is not optimum; higher gain can be obtained by increasing the length. The low gain of waveguides C and D suggests that they are not practical for making waveguide amplifiers. The increase in pump power will not enhance the performance of these waveguides significantly, as suggested in Fig. 3.3.6 and Fig. 3.3.7. A very long

length is required to achieve any reasonable gain. Although the gain is considerably higher in waveguide B than the other two structures, it still requires a long length to achieve the same amount of gain as with the pure erbium-glass core.

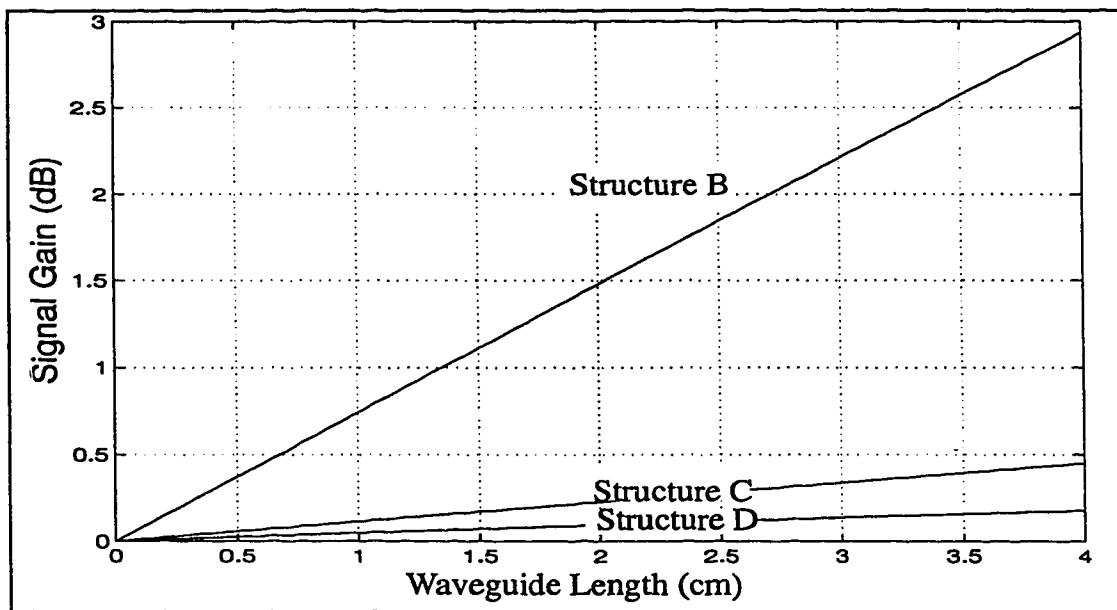


**Fig. 3.3.9 Signal Gain for three different waveguide structures**

# **Chapter 4 Fabrication of Polymer Waveguides and Sidewall Taps**

## **4.1 Introduction**

It was concluded in the last chapter that it is required to fill the entire v-groove core with erbium-doped glass to obtain sufficient gain over a short distance. However, the deposition of more than 2  $\mu\text{m}$  of erbium-doped glass is difficult, and hence the fabrication of a 1.1  $\mu\text{m}$  erbium-glass core is not yet possible. Therefore, it was decided that the waveguide amplifier would not be fabricated. The polymer waveguide with the metallized end-facets was fabricated in this research. Also, an investigation was conducted to determine the feasibility of integrating the sidewall tap into the singlemode v-groove waveguide.

The next section describes the fabrication and measurement of waveguides with polymer cores. Section 4.3 presents the methods for metallizing the end-facets of the waveguide. The investigation of integrating the sidewall taps into the singlemode v-groove waveguide will be presented in the last section of this chapter.

## **4.2 V-groove waveguides with polymer cores**

### **4.2.1 Introduction**

The fabrication of a polymer waveguide consists of two major steps. The first step deals with the etching of the v-grooves in the silicon wafer. The second step deals with the deposition of different layers of materials into the v-groove. The etching procedures can be found in Appendix C. A mixture of KOH+IPA was used in the anisotropic

etching. The mixture is highly corrosive, but it is safer to humans than EDP [37]. Also, the etch rate of the mixture does not vary significantly with time. 30% (by weight) KOH solution was used in this research. An excess amount of IPA solution was poured into KOH to ensure that the IPA was always saturated in the KOH solution. The function of the IPA in the KOH solution seems to produce smoother etching, more details of which will be discussed below. The etching temperature was set at 76° C. The downward <100> etch rate is about 0.6 μm/min.

To examine the function of the IPA in the KOH solution, several wafers were etched in pure 30% KOH solution. The side walls of the etched v-grooves were quite rough. It was initially thought that the solution was contaminated. Therefore, a fresh KOH solution was prepared and was allowed to settle for 2 days. However, the v-grooves etched by the new solution showed similar roughness. To ensure that this was not due to insufficient etch time, wafer was immersed into the solution for another 30 minutes. No apparent change was observed after the extra etching. An excess amount of IPA solution was then added into the KOH, and the wafers were put into the mixture for 5 minutes. The roughness was removed. The result is quite different from that obtained by other researchers [37,39], who claimed that the addition of IPA makes the sidewall surface rougher. The difference in the etching results maybe due to the difference in waveguide size, which affects the actual chemical reaction.

The remaining discussion in this section concentrates on the deposition of different layers of materials into the v-grooves. The polymer waveguide consists of the silicon-dioxide lower cladding, the polymer core, and the optional polymer upper cladding. A very persistent problem occurred in the deposition of the lower cladding which caused the

delay of the entire fabrication for a fair amount of time. The following subsection focuses on the discussion of the lower cladding layer and the associated problem. The description of two different ways of making polymer cores follows in the subsections 4.2.2 and 4.2.3. The waveguide measurements will be included along with the effects of depositing an upper cladding.

#### 4.2.2 Lower Cladding layer

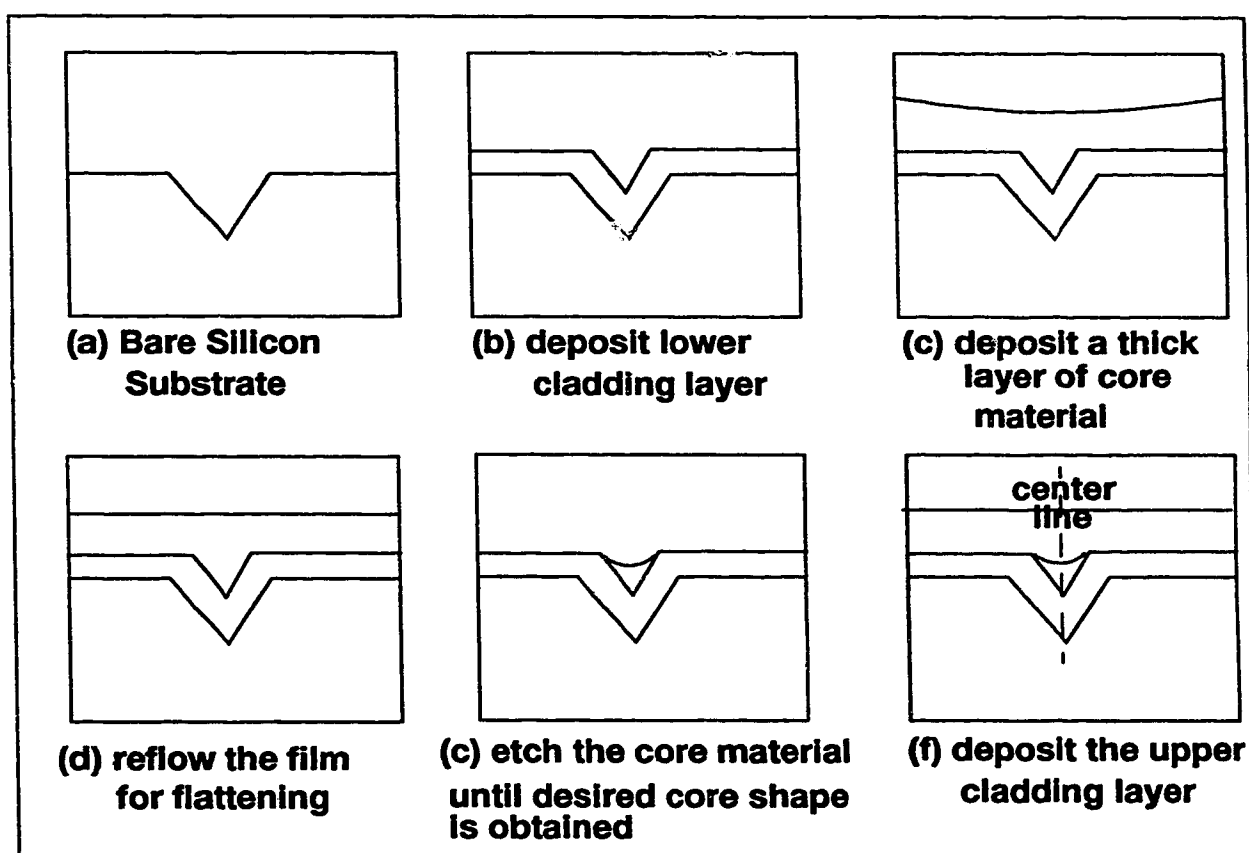


**Fig. 4.2.2.1 Fabrication procedures for making V-groove waveguide**

Usually, a v-groove waveguide is fabricated by depositing three layers of materials after the v-groove has been etched. The fabrication procedures are shown in Fig.

4.2.2.1. First a lower cladding layer is deposited, then another layer of material with higher refractive index is deposited. In order to obtain the triangular core shape, an etch-back step of the second layer (procedure (d) in the diagram) is required. Either wet or dry etching can be used. The dry etch can be performed using RIE. The wet etch of silica glass is usually performed by using buffered oxide etchant (BOE). Before the etch-back step, the deposited core material must be reflowed to flatten the material. Without this step, the curvature on the top of the etched core would be very deep. After the desired shape of the core is obtained from etching, an upper cladding layer is then deposited on top.

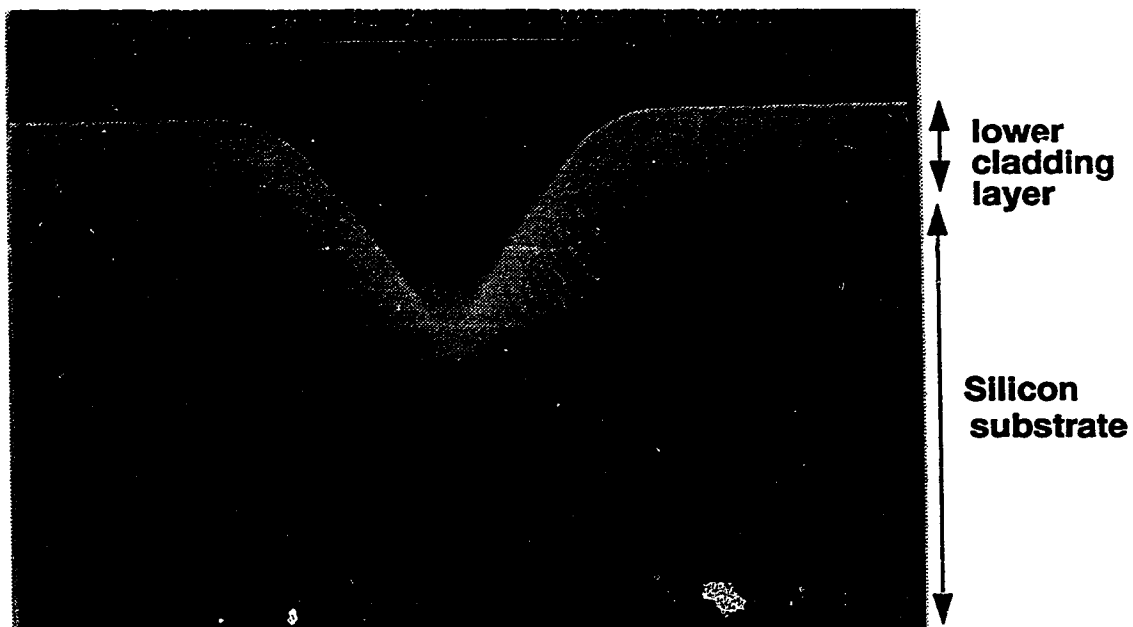


**Fig. 4.2.2.2 SEM picture of the Silicon Oxynitride Cladding**

According to the modal analysis, the maximum core size for which the waveguide is still singlemode is inversely proportional to the refractive index difference between the core and cladding (see Fig. 2.4.1.5). Therefore, the silicon oxynitride which can produce smaller index difference than by using the silicon dioxide was first used as the



cladding material. Fig. 4.2.2.2 shows a SEM shot of the 5  $\mu\text{m}$  oxinitride cladding layer. The cladding appeared to have good uniformity. Another layer of oxinitride with slightly higher index was then deposited on the top in an attempt to make an oxinitride waveguide.

In making the oxinitride waveguide, a big hole was observed at the tip of the groove after the BOE etch-back step, indicating that there is a weakness at the centre line of the v-groove. More SEM pictures were then taken, which revealed that a seam was formed along the centre line of the v-groove. One possible reason for the seam formation may be due to the chemical reactions occurring in the PECVD chamber as explained below.

The actual reaction chain in the PECVD is complicated and goes through a series of radical formation branches catalysed by surfaces. The silane diffuses from the gas to the surface of the wafer where it is adsorbed. The molecule then diffuses on the surface of the wafer until it reacts to  $\text{O}_2$  or else it desorbs. The diffusion length of the  $\text{SiH}_4$  molecule is small and this is part of the explanation of the seam formation. The growth rate of the film at any point is proportional to the number of silane molecules which land there. Because fewer silane molecules land at the bottom of the v-groove the deposition rate is slowest there. The reason that fewer molecules land at the bottom is because the diffusion from the gas phase to the surface is isotropic but the bottom of the v-groove only sees a limited angular section of this isotropic distribution. This results in a minimum growth rate at the bottom. As the film grows this situation will get worse as the bottom is left behind in the growth process. The result is seam formation [43].

To solve the seam problem, the deposition rate was reduced in the belief that the diffusion of silane can be improved. But the experimental results indicate no significant

effect, even when the deposition time was increased to more than 7 hours. Another attempt to solve the problem was to reflow the cladding layer. The wafer was put inside the 1000 °C furnace in a steady nitrogen flow for 90 minutes, but no change in the cladding shape was observed; the seam was still visible. It is believed that the softening point of the oxinitride is above 1100 °C. Because of the lack of any possible solution at the moment, the attempt to use the oxinitride as the cladding material dropped.

The LPCVD silicon dioxide was then used. Nevertheless, the same LPCVD device used by Narendra [36] was not available and thus a deposition process using her recipe [36] was not possible. The oxide layer obtained from the LPCVD device available in Alberta Microelectronics Center (AMC) showed the similar seam formation. After the reflow, the cladding layer was pulled laterally apart and a wider crack was resulted as shown in Fig. 4.2.2.3.

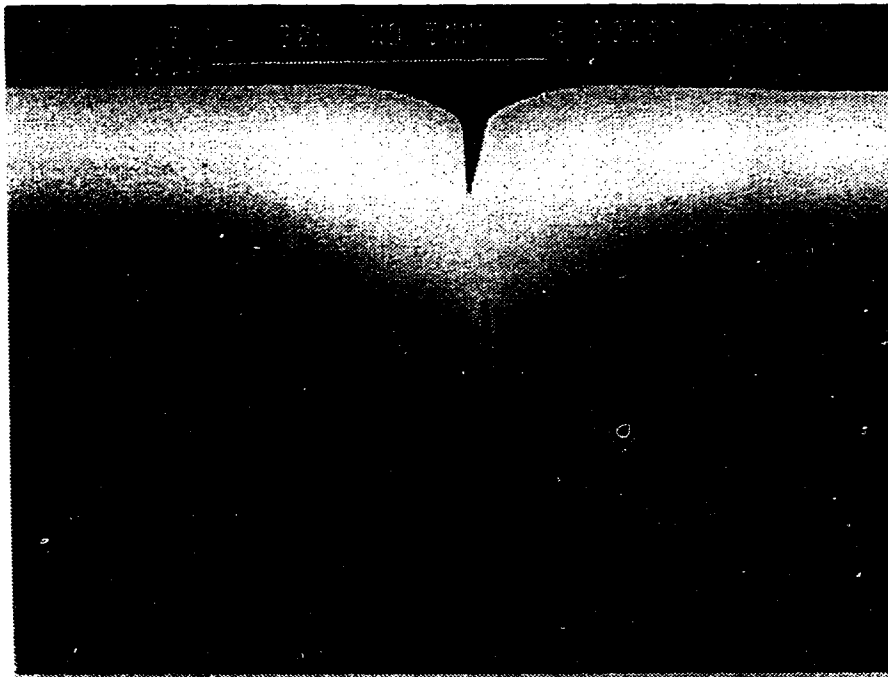


**Fig. 4.2.2.3 SEM picture of the cladding layer after wet reflow at 950 °C**

A series of reflow experiments were then conducted in attempt to remove these air bubbles and smooth out the surface. The reflow results are shown in Fig. 4.2.2.5. Most of the results shown in the SEM picture were reflowed in steady water-vapor flowing condition (wet reflow), except one picture that is specified 'dry reflow', which was reflow in steady nitrogen flow. It turns out that the wet reflow yielded slightly better results. According to Fig. 4.2.2.5, the BPSG begins to reflow properly above 1000 °C. At lower temperature, no significant reflow was observed. Even if the reflow time was doubled (2 hours), the seam was still apparent. At 1100 °C, it seems that the reflow time was too long, which causes the original v-shape to disappear. Nevertheless, we observe from the last SEM picture which displays the same waveguide with slightly tilted angle, the profile is quite non-uniform; the air trapped in the cladding layer has not been fully released. This implies that it requires to reflow the cladding for a longer time. Based on these observations, it can be deduced that the optimal reflow temperature should be between 1000°C and 1100°C, and the reflow time should be more than 1 hour.

Unfortunately, the problem of the seam formation was not solved and more experiments are required to fine-tune the reflow condition. Instead of spending more time to develop the deposition process, this BPSG cladding was used for making the polymer waveguide. It should be reminded that due to the roughness of the cladding, the waveguide will have a higher loss.

### 4.2.3 Dispensed Polymer Core

One way to deposit the polymer core is by direct dispensing. In this research, the direct dispensing was done by utilizing the computer-controlled dispensing setup at TRILabs. To dispense the polymer into the v-groove, the computer program requires the user to specify the starting and end points of the dispensing course, and the dispensing speed. The polymer is released from the syringe by forcing compressed air into the syringe. The pressure of the compressed air is pre-set by the user. Once these parameters are set, the computer will perform the dispensing automatically. The schematic diagram of the set-up is shown in Fig. 4.2.3.1. In the past, this dispensing set-up has been successfully used to fill the core and upper cladding of multimode v-groove waveguides [37].

One major difficulty in dispensing the polymer into the singlemode v-groove is that the size of the syringe tip is larger than the width of the waveguide. The available capillary tips for the syringe have diameters of 12  $\mu\text{m}$ , 19  $\mu\text{m}$ , 30  $\mu\text{m}$  and 50  $\mu\text{m}$ , but the compressed air does not provide enough pressure to release the polymer out of the 12  $\mu\text{m}$  tip consistently. Therefore the smallest usable tip size is 19  $\mu\text{m}$  which is much larger than the width of the singlemode v-groove. Because of this, it seems that an overflow of the polymer onto the wafer surface cannot be avoided, and a convex waveguide top will result. To minimize the thickness of the overflow, NOA (Norland Optical Adhesive) 81 polymer was used, which has the lowest available viscosity. Also, the dispensing speed and the pressure of the compressed air was adjusted so that the minimum amount of polymer was dispensed.

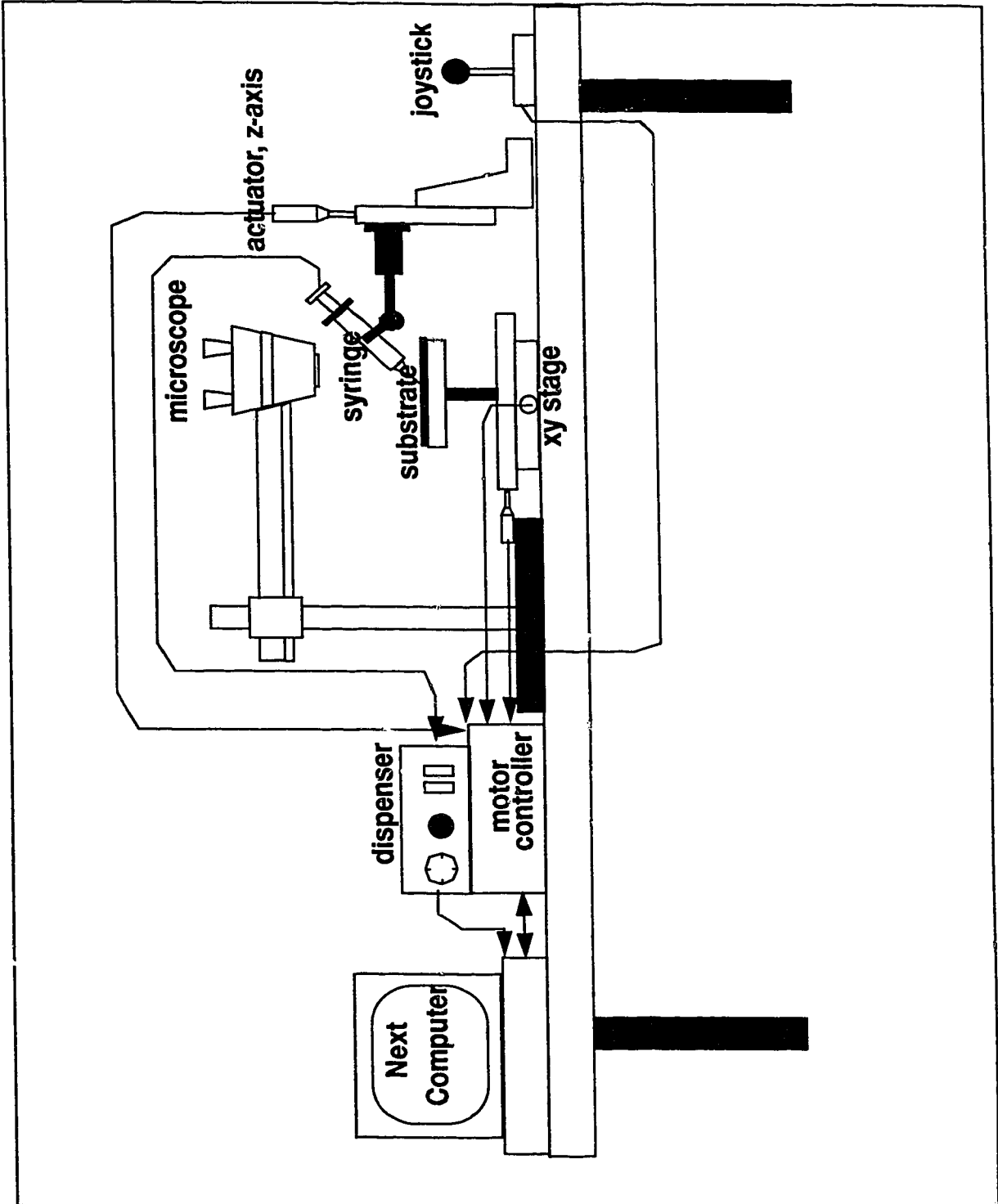
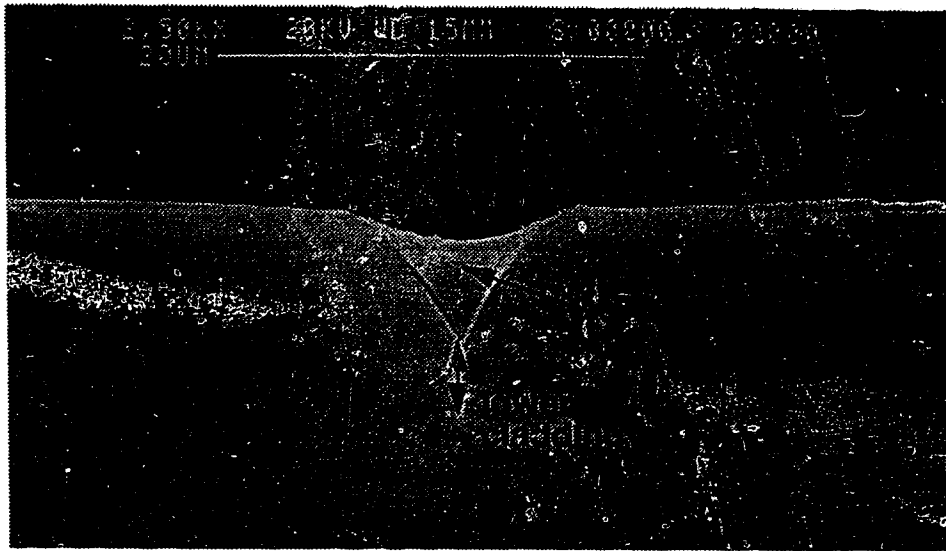


Fig. 4.2.3.1 Schematic Diagram of the Polymer Dispensing Set-up in TRLabs

During the dispensing, the syringe was tilted at about  $45^{\circ}$  and the tip touched the surface of the wafers. The result of the dispensed waveguide is shown in Fig. 4.2.3.2. The SEM picture shows that only a thin layer of the polymer is seen on the neighboring surface. The core itself has a concave top surface, but the predicted overflow did not appear. The cross-section of the waveguide appears to have good uniformity. However, for most of the dispensed waveguides, the polymer core was separated into one or a few segments, due to occasional beading during the dispensing. It was initially thought that the beading was due to the high dispensing speed. More trials with slower speed were done, but the beading problem still occurred, which demonstrated that the beading was not caused by the high dispensing speed. Another possible cause is the presence of dust particles inside or near the waveguides, which causes the syringe tip to leave the wafer surface and hence yield the discontinuity. The dust problem was indeed observed, but only in a few occasions. It is not quite certain which is the main cause of the beading, but it seems that the beading is possibly related to the contact between the syringe tip and the v-groove. For a perfectly smooth wafer surface, the syringe tip would slide along the wafer surface. If instead some roughness is present on the wafer surface, the tip would possibly be bumped up as it moves. However, as observed from Fig. 4.2.2.4, the surface of the cladding layer is quite smooth, the roughness is only seen on the surface of the sidewalls. The syringe tip has little contact with the sidewalls because of the large tip diameter; therefore it is still not certain whether this is the main cause of the beading.

To eliminate the beading, the only solution seems to be to avoid touching the wafer surface with the syringe. This requires one to bring the syringe very close to the surface without touching it. The polymer hanging at the tip of the syringe still needs to touch

the wafer surface. To increase the contacting surface between the polymer and the wafer, the syringe is placed vertically above the wafer surface. The maximum separation between the tip and the surface must be less than or equal to the thickness of the polymer hanging at the tip. The approach is difficult because the 3" wafer, which initially is very flat, warps due to stress exerted from the lower cladding after the wafer is cooled off from the LPCVD process. By touching different points on the wafer surface with the tip of the syringe, it is confirmed that the wafer has a height variation of at least 20  $\mu\text{m}$  with the center being highest. Because of the convex surface, the tip may touch the surface at one point, but may be too distant at another point. The wafer is held on a vacuum chuck when dispensing the polymer, but this does not improve the flatness of the wafer. Details of this approach are described below.



**Fig. 4.2.3.2 SEM picture of the cross section of the dispensed polymer waveguide**

For the new trials, the tip of the syringe was polished. The capillary tip was cut to about 5 mm long to provide higher pressure. The dispensing speed in both x and y direc-

tions were set to 5 (the actual speed =  $5 \times 0.0205 \text{ mm/sec} = 0.1025 \text{ mm/sec}$ ), because higher speeds than this caused the beading to occur. The pressure of the compressed air was set at 60 psi. Before the dispensing procedures, the stage that holds the wafer was levelled. The dispensing procedures started by bringing the syringe to the middle of the waveguide which was believed to have the maximum bowing, and setting the distance between the tip and the surface to less than or equal to  $10 \mu\text{m}$ . The syringe was then allowed to travel the entire waveguide length prior to dispensing to ensure that the syringe did not touch the surface at any point within the dispense course.

The results show that it is difficult to dispense a continuous polymer core along the entire v-groove length (about 6 cm). Very often, the polymer started to fill the grooves after the syringe had been travelling for 1 cm and ceased a few centimetre before the designated end-point. Also, the thickness of the dispensed polymer line varied from one waveguide to another even though the material was dispensed at a constant rate. This was caused by the difference in distance between the tip and the surface from one waveguide to another.





Finally the distance between the tip and surface was manually adjusted during the dispensing. This is not an ideal solution because the z-axis positioner is very sensitive to manual adjustment on this scale. Sometimes, the adjustment was too extreme, which caused the tip to either touch the surface or to rise too far away from the surface. Very often, the dispensing had to be stopped at some point in the waveguide and then resumed after adjusting the height of the syringe. This affected the quality of the waveguides. An optical picture of the cross-section of the dispensed polymer waveguide is shown in Fig. 4.2.3.3. An overflow layer can be clearly observed, and its thickness is about 1  $\mu\text{m}$ .

The resulting waveguides were then tested. The output light distribution of the waveguides was captured using the set-up shown in Fig. 4.2.3.4. One of the distributions is shown in Fig. 4.2.3.5. In the figure, the core height of the waveguide is about 5  $\mu\text{m}$ . The output light distribution of the other waveguides with different widths is similar. The optical picture reveals that the light coupled into the waveguide excited the modes both in the v-groove and the overflow layer. At 1  $\mu\text{m}$  thick, the overflow layer can support many guiding modes. There was an attempt to change the launching condition to excite solely the modes in the v-groove. But it seemed that the modes in the overflow layer were always excited as well.

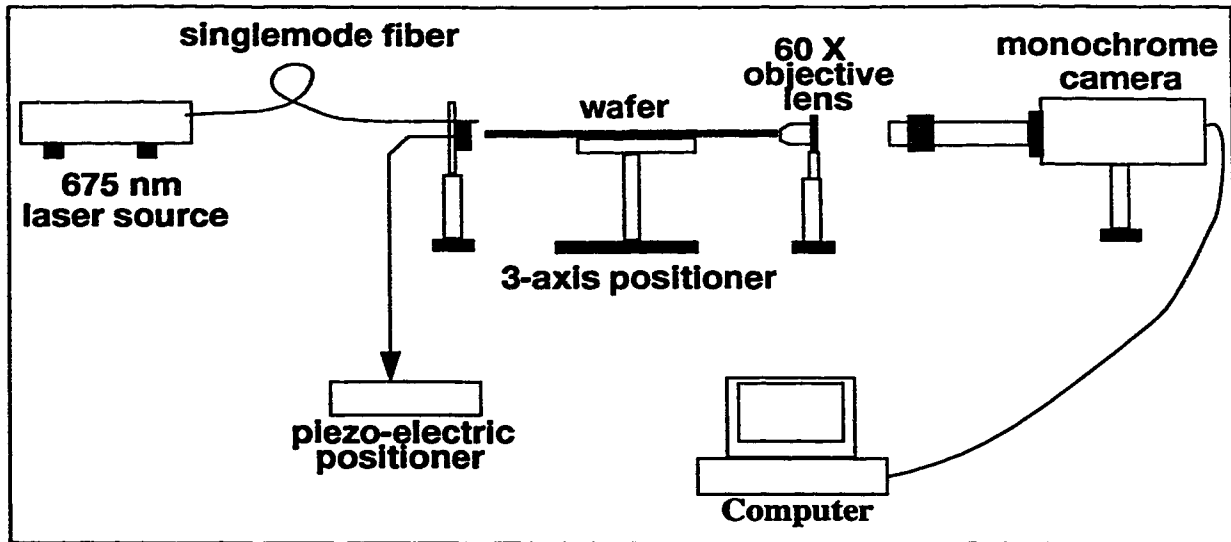


**Fig. 4.2.3.4 Schematic Diagram of the set-up for capturing the output mode field.**

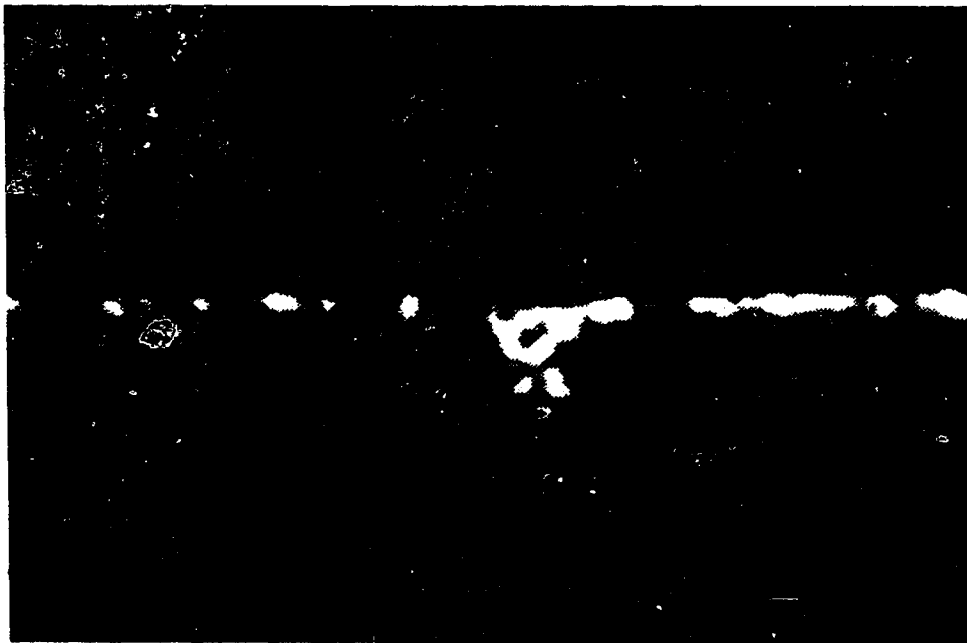


**Fig. 4.2.3.5 Gray-Scale Image of the output light from the waveguide**

The waveguide loss was not measured since it is not possible to isolate the light that propagates in the overflow layer. Also, the upper cladding was not deposited. An

additional upper cladding layer would cause the modes in the v-groove to shift toward the overflow layer. This would make it harder to isolate the modes in the v-groove from the modes in the overflow layer.

In conclusion, the dispensed waveguide seems always to be multimode because of the relatively thick overflow layer.

#### 4.2.4 RIE Polymer Core

The second way to fill the core with polymer is by spinning a layer of polymer on the silicon wafer and then etching off the excess. The fabrication procedures are very similar to those shown in Fig. 4.2.2.1, except that no reflow is performed. In this method, the beading problem can be totally eliminated, and the overflow can be avoided. The major disadvantage of this approach is that the etched surface is not as smooth as the dispensed core. It is difficult to polish the core surface, since the polymer is soft compared to the glass, and it requires some mechanism to hold the wafer stable for polishing.

NOA 81 polymer was used, which gives the thinnest spin-on polymer layer. Prior to the spinning procedure, the wafer was immersed into a Piranha solution for about 20 minutes to remove any organic substance from the wafer. After the cleansing, a sufficient amount of the polymer was put on the wafer. Any visible air bubbles trapped in the polymer layer were removed. The wafer was then spun at 7000 rpm, which yielded a thickness of about 4.5  $\mu\text{m}$ . The polymer was cured for 450 seconds under the 245 W ultra-violet source of the mask aligner. After the exposure, the wafer was put into the RIE device for etching. The gas composition included 80%  $\text{CHF}_3$ , 15% nitrogen and 5% Oxygen. The power and pressure was set at 140 W and 40 mtorr respectively. The etch rate of the polymer for this recipe is 0.04  $\mu\text{m}/\text{minute}$ . The cross-section of the resulting polymer

waveguide is shown in Fig. 4.2.4.1. No defect is observed in the SEM picture, and the profile of the waveguide is fairly uniform.

The output modes of the waveguides were captured using a set-up similar to the one in Fig. 4.2.3.4. A 632 nm HeNe laser source was used, and the light was free-space coupled into the waveguide using a 60 X objective lens. The output mode fields for different waveguides are shown in Fig. 4.2.4.2. As shown in the figure, the mode field was first magnified by the 60 X objective lens, then the image of the field was captured by a camera with zooming capability. The exact magnification ratio is not certain; therefore the dimensions of the captured mode fields was not determined. It is evident from the figure that as the waveguide core size reduces, the number of propagating modes reduces accordingly. With the core height reduced to 1.5  $\mu\text{m}$ , the waveguide seems to become singlemode. Different launching conditions were tried to observe any change in output mode shape for this waveguide size. No significant change was observed. According to the modal analysis, at this core size the waveguide can support 3 modes. But, as mentioned earlier, because of the cladding roughness, the optical power carried in the second and third modes might be significantly attenuated after 3 cm of propagation. Also, the chance of exciting these two modes by the input light is smaller than that of exciting the fundamental mode, because of the difference in mode shape. Therefore, it is very likely that the waveguide is effectively singlemode.

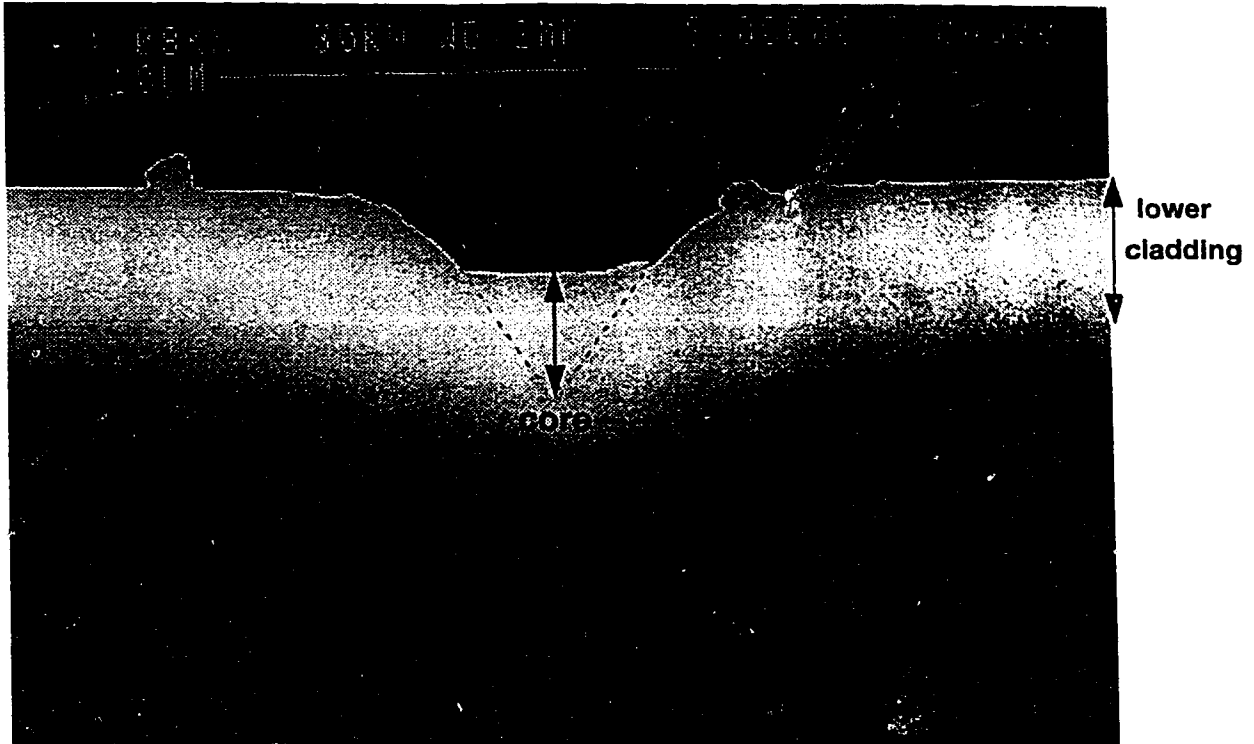
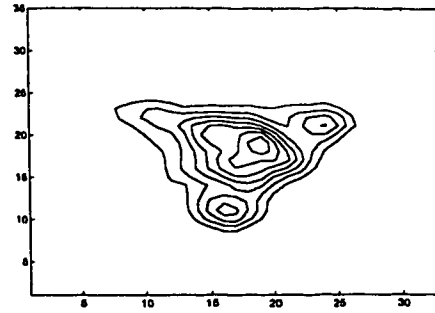
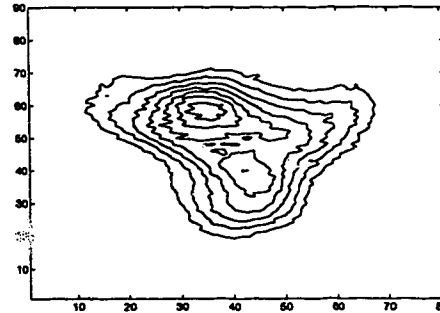
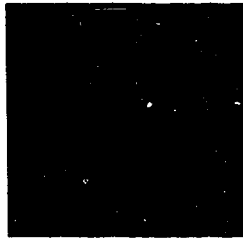


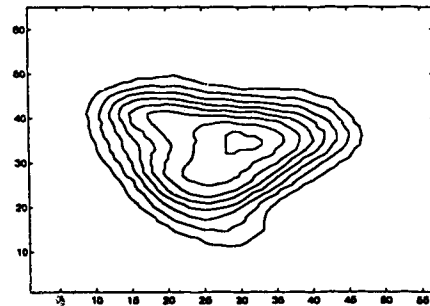
**Fig. 4.2.4.1 SEM picture of the RIE polymer waveguide**



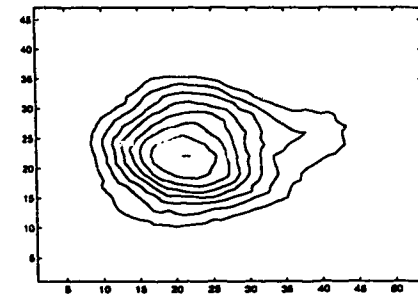
**core height = 6.0  $\mu\text{m}$**



**core height = 4.5  $\mu\text{m}$**



**core height = 3.0  $\mu\text{m}$**



**core height = 1.5  $\mu\text{m}$**

**Gray-Scale Images**

**Contour Plots**

**Fig. 4.2.4.2 Gray-Scale Image and the corresponding contour plots of the output modes**

The scattering loss measurement was carried out using the set-up shown in Fig. 4.2.4.3. The measured results are presented in Fig. 4.2.4.4. From the linear curve-fit, the propagation loss seems to increase as the core size decreases. The loss increases from 1.8 dB/cm to 3.8 dB/cm. One source of the waveguide loss is the roughness of the cladding layer. As the size of the waveguide decreases, the roughness occupies a relatively larger volume of the waveguide and hence more light is scattered out of the waveguide and the propagation loss increases. The other cause of loss would be the roughness of the core surface due to the RIE process. For the smallest waveguides, the attenuation is so high that the scattering power cannot be measured. Therefore the cutback method was used. In the cutback method, the waveguide is cleaved a number of times from the output end of the waveguide. After each cleaving, the output power is remeasured. From these output power measurements, the attenuation loss can be estimated. In order to obtain a precise estimate of the loss, the width of the cleaved-off piece of the waveguide should be kept small. Also, the input optical power should be kept constant. One way to keep the input power constant is to pigtail the input fiber to the waveguide. The difficulty of this approach is to hold the fiber steady without bending after the fiber is pigtailed to the waveguide. One way to hold the fiber is to use a separate piece of wafer which contains some large v-grooves to fix the fiber. The fiber can be put inside one of these large alignment grooves and then a layer of silicone can be pasted on top to fix the fiber in the groove. However, this makes the cleaving of the waveguide very difficult because the two separate pieces of wafers are required to be levelled at all times. Therefore, in this research, the fiber was butt-coupled to the waveguide without any fixation. The accuracy of the measured output power would depend heavily on the realignment of the input fiber to the waveguide after each cleaving.

The accuracy of the estimated attenuation loss can be improved by performing the cutback to several waveguides with the same size.

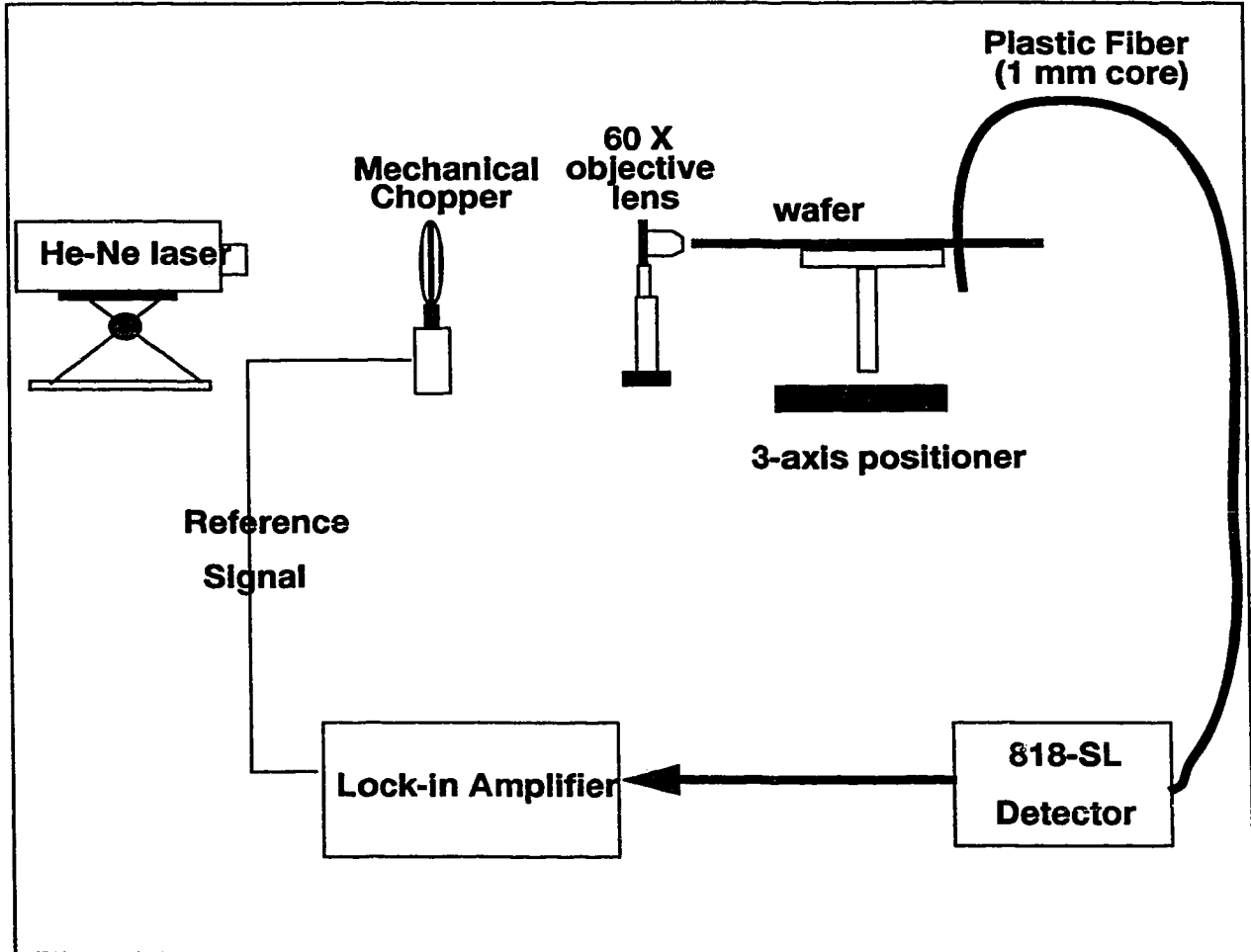


**Fig. 4.2.4.3 Schematic Diagram of the set-up for measuring Scattering Loss.**



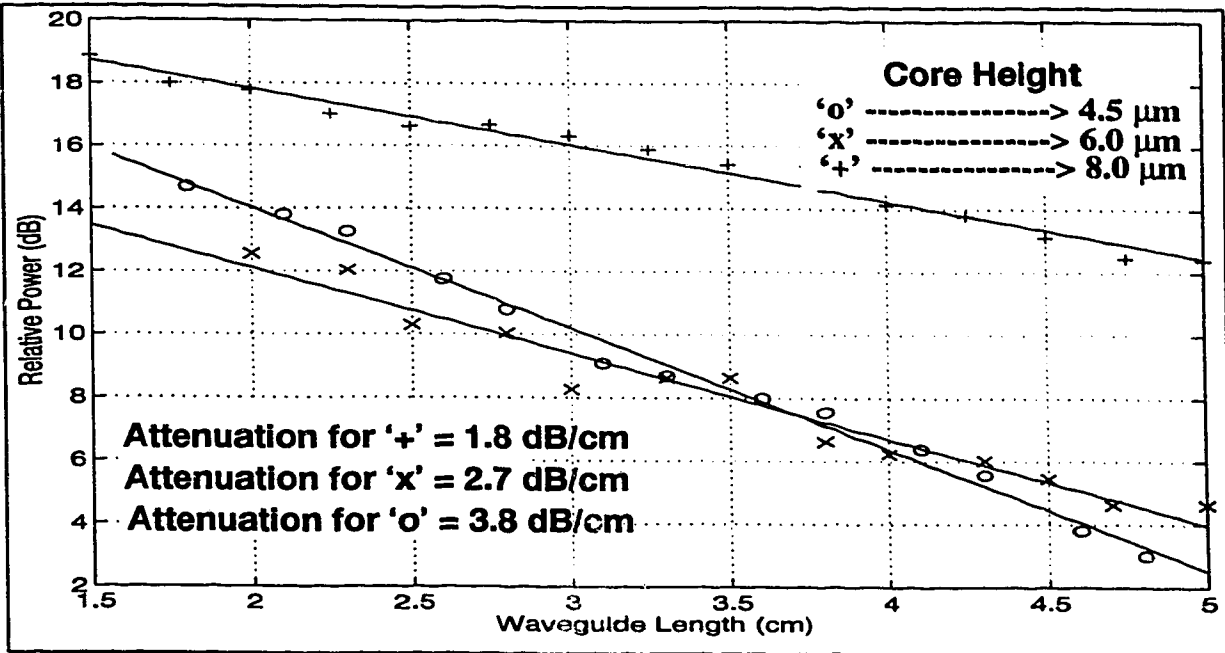


**Fig. 4.2.4.4 Scattering Loss Measurements for different waveguide sizes**

The light was coupled into the waveguides from a singlemode fiber of 3.5  $\mu\text{m}$  core diameter. As estimated from the measurement, the propagation losses of four waveguides with 4.5  $\mu\text{m}$  core height are well matched to the values obtained from the scattering loss measurement. The plots of the measured results are shown in Fig. 4.2.4.5. For the waveguides with 3  $\mu\text{m}$  core height, the propagation losses of three waveguides are 9.6 dB/cm, 11.2 dB/cm and 8.8 dB/cm respectively. These values are not quite accurate, because the output power of a 5 cm long waveguide is less than 1 nW, which yields a relatively high uncertainty as to the measured value. The attenuation losses of different waveguides are plotted as a function of the core height as shown in Fig. 4.2.4.6. There is some evidence which shows that as the core height is increased to a very large size (> 100  $\mu\text{m}$ ), the attenuation levels off at about 1.0 dB/cm [37],[39]. On the other hand, as the core

height is decreased, the attenuation would be increased greatly because the roughness of the cladding becomes relatively bigger compared to the size of the waveguide core. In Fig. 4.2.4.6, a curve is fitted to estimated attenuation losses which shows that the attenuation indeed levels off as the core height is increased and approaches a large value as the core height is decreased; therefore, it is reasonable to believe that the attenuation loss of 3.0  $\mu\text{m}$  core is about 9.5dB/cm.

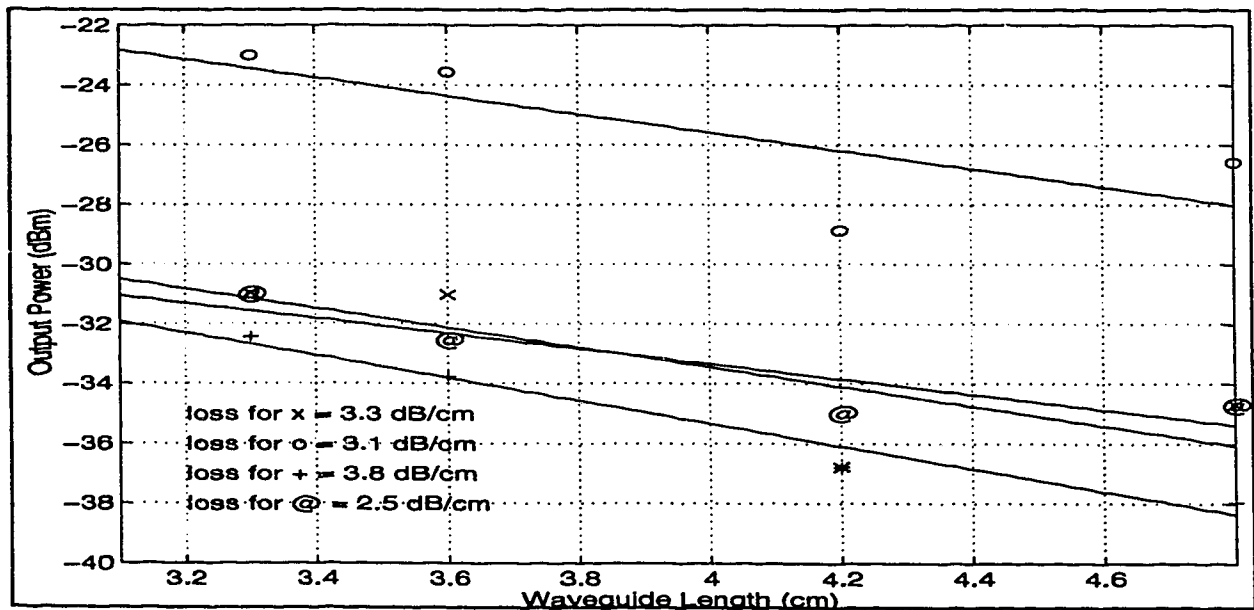


**Fig. 4.2.4.5** Measurements from cutback methods for 4 4.5  $\mu\text{m}$  core height waveguides.

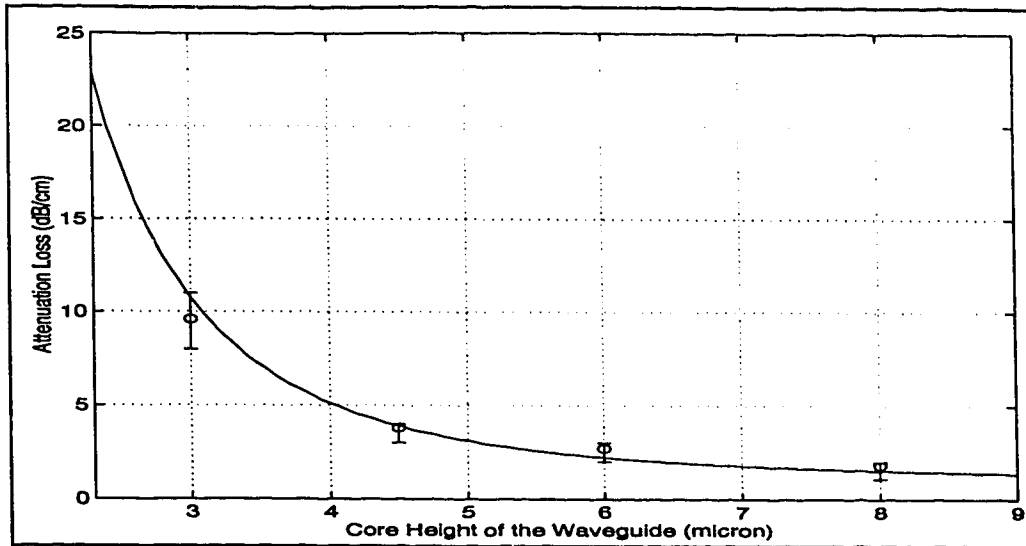


**Fig. 4.2.4.6 Attenuation Loss versus Core Height**

The coupling losses of different waveguides are calculated using (4.1). Table 4.2.4.1 shows the estimated coupling losses of some of the waveguides whose attenuation losses are shown in Fig. 4.2.4.4 and Fig. 4.2.4.5. The output power of the waveguides was measured several times, the measured values vary about  $\pm 3$  dB; therefore the estimated coupling losses are not quite accurate. But it is certain that the coupling losses of the waveguides are more than 10 dB. Possible reasons are that the modes in the fiber are quite mismatched with the waveguide modes, and the ends of the polymer waveguides are not cleaved well. The experience of our research group has been that polymer does not cleave as cleanly as glass.

$$\text{Loss}_{\text{coupling}} = \text{Power}_{\text{input}} - \text{Power}_{\text{output}} - \text{Length}_{\text{waveguide}} * \text{Loss}_{\text{attenuation}} \quad (4.1)$$

**Table 4.2.4.1 Coupling losses of different waveguide sizes**

Core Height ( $\mu\text{m}$ )	Input Power (dBm)	Output Power (dBm)	Attenuation Loss (dB/cm)	Waveguide Length (cm)	Coupling Loss (dB)
4.5	2.8	-32.8	3.1	4.8	20.7
6.0	6.0	-23.0	2.7	5.0	15.5
8.0	6.0	-18.9	1.8	5.0	15.9

A layer of NOA 68 polymer (refractive index = 1.54) was then spun on the polymer waveguide to form an upper cladding. When light was launched into the input end of this waveguide by free-space coupling, a large amount was coupled into the upper cladding layer. The coupled light was seen to fan out in a wide angle and it was not possible to distinguish the propagating light in the waveguide core from the light in the cladding. Therefore, the scattering loss measurement could not be performed. To reduce the amount of light coupled into the upper cladding, the polymer layer was deposited on another wafer using the direct dispensing technique. The resulting upper cladding layer has a width of about 150  $\mu\text{m}$  and height of 1  $\mu\text{m}$ , and the cross-section of the cladding has a convex shape. A laser was then launched to this new waveguide. The output light distribution was similar to that in Fig. 4.2.3.5. The scattering light in the upper cladding was guided because the cladding layer is laterally confined. There was an attempt to lower the input fiber to reduce the amount of light coupled into the upper cladding, but the scattering light was always seen in different launching conditions. Therefore, both scattering loss and cut-back measurements could not be performed. It seems that the mode mismatching between

the fiber and the waveguide causes a significant amount of light to be coupled into the upper cladding in any launching condition.

### **4.3 Metallizing the waveguides for vertical coupling**

Two ways of metallizing the end-facets of the waveguides have been tried. The simple way is to metallize the entire wafer before putting on the cladding layer, but this would probably introduce higher attenuation. Another problem associated with this method is that, due to the high temperature CVD process, the reflectivity of many metals is reduced significantly as mentioned in [36]. The reason is that at an elevated temperature, the metal melts and recrystallizes when it cools. As a result, the metal surface has small bubble formations which reduce reflectivity.

To discover the metal that could withstand the high temperature CVD process, several different metals were deposited on the smooth silicon wafers and covered with the CVD oxide. The reflectivity of these metal-glass surfaces was measured. The measurements show that the gold and titanium metal surfaces yield higher reflectivity after the CVD process. The reflectivity of both gold and titanium surfaces was close to 55% at a 45° incident angle for non-polarized light of 632 nm wavelength. Several trials were conducted to deposit the titanium into the  $v$ -grooves. Unfortunately most of the time smudges were observed on the wafers. To investigate the cause of these smudges, the oxide layer was stripped off. It was observed that some parts of the titanium layer had changed its color to brown, which indicated that the metal was oxidized. The causes of the oxidation are unknown. It was decided not to pursue the causes.

The second method is to metallize solely the end-facets surface after the cladding

layer is deposited. This requires extra lift-off procedures as illustrated in Fig. 4.3.1. A layer of HPR-506 positive photoresist was spun on the cladding layer at a speed of 5000 rpm for 20 seconds to yield a 2  $\mu\text{m}$  thick layer. The wafer was pre-baked at 110  $^{\circ}\text{C}$  in vacuum for 50 seconds using the Solitec hot plate to vaporize the solvents completely and to enhance adhesion to the cladding. Then the wafer was put under the microscope for objective lens exposure. A 100 X objective lens was used, which exposes a spot of 150  $\mu\text{m}$  in diameter. The exposure time was set at 60 seconds. The exposed wafer was developed using Microposit developer 354. The wafer was post-baked at 120 $^{\circ}$  C for 60 seconds. A 0.1  $\mu\text{m}$  thick of titanium was then deposited on the wafer. After the metal deposition, the unwanted metal layer along with the photoresist was lifted off using acetone. Several wafers were tested with this technique. The results show that the titanium bonds strongly on the end-facets and the surface appears to be quite smooth.

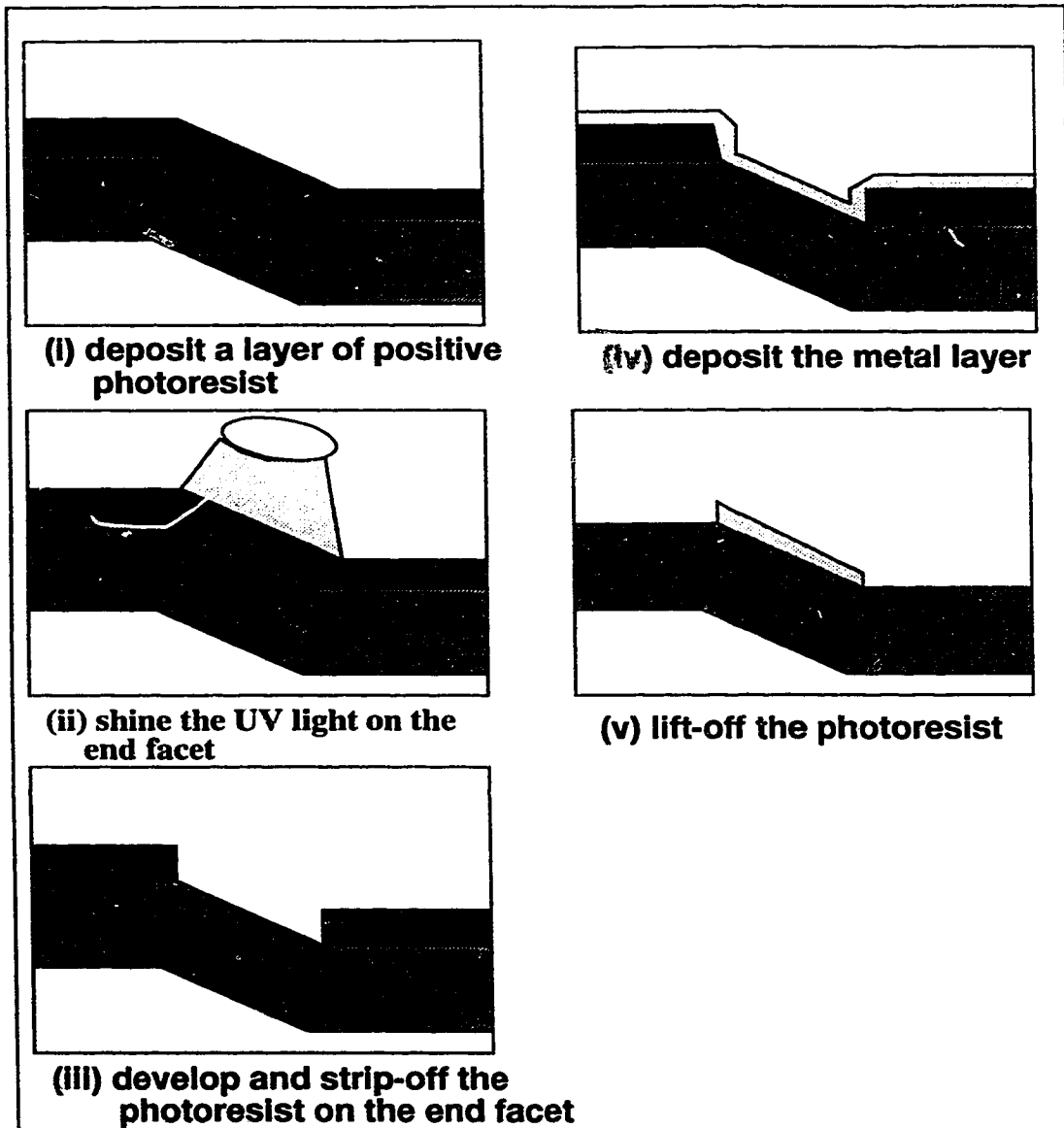


**Fig. 4.3.1 Procedures of Metallizing the end-facets**

NOA 81 polymer was then used to make waveguides using the RIE method. The optical power reflected from the end-facets was measured at 675 nm wavelength. The input power was 1.34 mW, and the reflected power from the end-facets for 9, 6, and 4  $\mu\text{m}$  waveguides was 1.6  $\mu\text{W}$ , 0.28  $\mu\text{W}$  and 0.86 nW respectively. To estimate the excess loss

in the tapping, the 1.45 cm long waveguide was cut 3 mm before the end-facets, and the throughput power was measured. The values of the power were 19.7  $\mu$ W, 2  $\mu$ W and 47 nW for 9, 6 and 4  $\mu$ m waveguides respectively. The excess losses at the end-facets, calculated by dividing the reflected power by the throughput power, were 8.3 dB, 8.5 dB and 17.4 dB for 9, 6 and 4  $\mu$ m waveguides. Due to the low measured power for the 4  $\mu$ m waveguide, the estimated power loss may not be accurate. It should also be noted that the actual loss from the end-facet would be lower because a portion of the reflected power was not picked up by the plastic fiber. It had been estimated that this waveguide-to-fiber coupling loss is approximately 3 dB [37]. Since the light was not reflected at a right angle, it was required to tilt the fiber at an angle to the surface in order to properly capture the light. The actual excess loss is around 5 dB.

One source of the loss is the placement of the metal layer. Because the end-facet was metallized after the cladding layer was deposited, only the light that propagated in the core would be reflected. Another source of loss is the titanium metal surface, which has lower reflectivity. Also, the throughput power was measured 3 mm before the end-facets; therefore the actual power arriving at the end-facet would be about 1 dB less.

#### **4.4 Sidewall Taps**

In this part of the research, the main objective is to investigate the feasibility of integrating the sidewall taps into singlemode waveguides for interconnection application.

According to Macleod's simulation [37] for the multimode waveguides, the amount of power reflected by the sidewall taps is proportional to the cross-sectional area of the waveguide and the area of the tap. To make an array of taps that can tap equal



amounts of light out of the waveguide, the last sidewall tap must cover 50% of the waveguide cross-sectional area. The analysis might not apply to the singlemode waveguide, but at least the analysis provides a coarse estimation. In order to make a 50% tap, Macleod calculated that the undercutting rate along the 45° diagonal line of the convex corner should be less than  $\sqrt{2}$  of the downward (<100>) etch rate.

To integrate the sidewall taps into the v-groove, the size of the taps must also be controllable. The etch rate must therefore be slow enough so that both large and small taps can be formed in the same waveguide.

To conduct the investigation, direct e-beam writing was utilized to pattern the masking layer. The procedures of the e-beam writing can be found in Appendix D. The advantage of using the direct e-beam writing is that the mask pattern can be easily modified. The final mask pattern used in the experiments is shown in Fig. 4.4.1. The wafer was etched in a 76° C KOH+IPA solution.

According to the etching results, the diagonal etch rate is about 0.3  $\mu\text{m}/\text{min.}$ , compared to the downward etch rate of 0.6  $\mu\text{m}/\text{min.}$  This satisfies the  $\sqrt{2}$  criteria for making the 50% tap. The SEM pictures of some of the sidewall taps are shown in Fig. 4.4.2. Due to some error in e-beam writing, the width of the waveguides is slightly different at the two sides of the taps, as shown in the figure. For most of the sidewall taps, the measured angles between the sidewall of the waveguide and the tapping plane of the sidewall tap are between 110° and 115°. This indicates that tapping plane is possibly the intermediate plane between <212> and <313>, which would have made angles of 116.6° and 108.4° with the sidewalls. This matches the results obtained by Macleod [37].

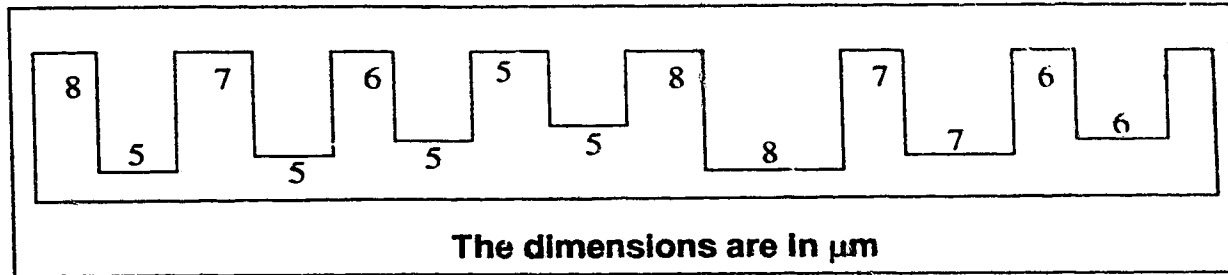
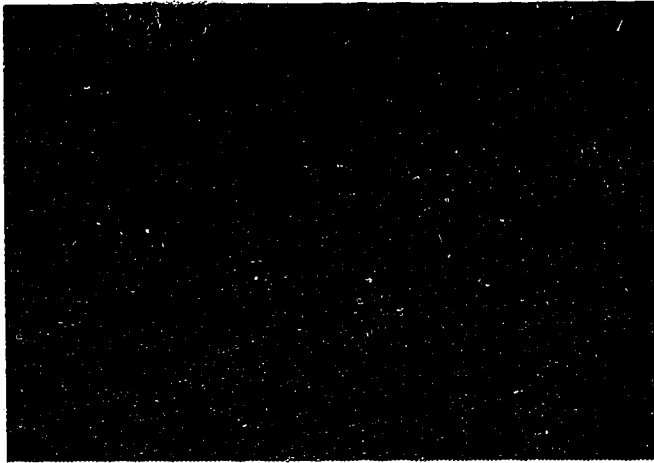


**Fig. 4.4.1 Mask Pattern for Direct E-beam Writing**

The SEM pictures show that taps with different sizes can be formed in the same waveguide. The tapping planes are very smooth, and no other crystal planes were observed. Also the diagonal etch rate is slow enough to form a 50% tap. Therefore, integrating the sidewall taps into the singlemode waveguide should be feasible.



**6 μm X 6 μm**



**7 μm X 5 μm**



**8 μm X 5 μm**



**8 μm X 8 μm**

**Fig. 4.4.2 SEM Pictures of different sidewall taps**

# Chapter 5 Conclusion

## 5.1 Summary of Works

Several tasks were accomplished during this research. First, a modal analysis program was written to estimate the required sizes for several types of singlemode v-groove waveguides. The program is based on the scalar finite element method (SFEM), which is a popular numerical method for solving second order differential equations. At the present, it is capable of analysing five different waveguide structures at any wavelength. Both erbium-doped silica waveguides and waveguides with polymer cores were analysed. In the case of erbium-doped waveguides, four different waveguide structures were analysed. For an erbium-doped waveguide with triangular core, It was found that with a 1.44 cladding index and a 1.59 core index, the maximum singlemode core height at 980 nm is 1.3  $\mu\text{m}$ . The corresponding confinement factors for signal(1550 nm) and pump wavelength are 42.7% and 72.4% respectively. For the other three waveguide structures, the confinement factors are a few times smaller. Also, it was found that by reducing the refractive index difference between core and cladding, the maximum singlemode core height can be greatly increased, while the confinement factors remain about the same. Another result obtained from the analysis is that the confinement factor drops rapidly as the core height decreases. At the signal wavelength, the confinement factor is decreased by about 8% for every 0.1  $\mu\text{m}$  of core height reduction. For waveguides with polymer cores, it was found that with a 1.56 core index, even without the polymer upper cladding, the waveguide can be effectively singlemode if the core height is less than 2  $\mu\text{m}$ . Also, it was found that if overflow occurred, the waveguide is most likely multimode.

To estimate the amplification performance of the erbium-doped silica waveguide,

a computer program was written based on a four-energy level model, which takes into account the upconversion phenomenon. The program is capable of simulating the gain profile and computing the output noise spectrum of the amplified spontaneous emission. The simulation program uses the mode field data calculated from the modal analysis for input conditions. It was found that only the waveguide with a pure erbium-doped core can obtain a reasonable gain in a few centimetres of propagation. Therefore, other erbium-doped waveguide structures are not practical for optical amplification purposes. For an erbium concentration of  $3 \times 10^{26}$  ions/m<sup>3</sup>, the maximum achievable gain for a 4 cm long waveguide with 1.3  $\mu\text{m}$  core height is about 9.5 dB, but this requires 300 mW of pump power. If the pump power is optimized at 100 mW, the gain is close to 7.2 dB. The signal gain decreases rapidly as the core height is reduced. For a waveguide with 0.9  $\mu\text{m}$  core height, the gain drops to 2.5 dB, and this would virtually be a transparent waveguide instead of a waveguide amplifier.

Knowing that it is not yet possible to fabricate a waveguide with a pure erbium-doped core, only the waveguides with polymer cores were fabricated. Both the direct dispensing method and the RIE method were used to form the polymer core. The experimental results show that when using the direct dispensing technique, the resulting waveguide would always be multimode because of the thick overflow layer. It was also found that although no very sophisticated device is needed in the direct dispensing, this approach of depositing the polymer core is not easy because it requires a high degree of precision in manipulating the device and the fabrication time is rather long (total of 5 hours for 1 wafer). In contrast, the waveguide with a RIE polymer core has fairly good uniformity and the core height can be etched to as low as 1.5  $\mu\text{m}$ . The loss measurement shows that the

propagation loss of the waveguides is inversely proportional to the core height. By reducing the core height from 9  $\mu\text{m}$  to 4.5  $\mu\text{m}$ , the propagation loss increases from 1.8 dB/cm to 3.5 dB/cm. The effect of depositing a layer of polymer upper cladding is inconclusive, because a large amount of light was scattered in this cladding layer and consequently the loss measurement could not be performed. One source of the propagation loss is the surface roughness of the cladding layer. Unfortunately, the lower cladding has a seam along the centre line of the groove and a rough surface, which is possibly due to the short diffusion length of the silane gas during the LPCVD process. Many attempts had been made to improve the cladding quality, but the solution has not yet been obtained. Moreover, from the captured output mode field, it was found that the RIE waveguide becomes effectively singlemode at 1.5  $\mu\text{m}$  core height. This agrees with the results of the modal analysis.

Another part of this research was the metallization of the end-facets of the v-groove waveguides for optical coupling purposes. A lift-off technique was used to deposit the metal solely on the end-facets. The results show that the metal bonds strongly to the lower cladding layer and the metal surface is quite smooth. The measured excess loss in the tapping is about 8.5 dB, but the actual loss value is probably closer to 5 dB due to the fact that not all the reflected light was captured by the detector.

The last part of this research was the investigation of integrating the sidewall taps into the singlemode v-groove for optical interconnect applications. A mixture of KOH+IPA solution was used for the anisotropic etching. The experimental results show that the undercutting rate of the convex corner along the 45° diagonal line is 0.3  $\mu\text{m}/\text{min}.$ , compared to the 0.6  $\mu\text{m}/\text{min}.$  downward (<100>) etch rate, which satisfies the criteria for making a 50% tap. Also, the tapping plane of the sidewall tap was found to be the interme-

diate plane between  $\langle 212 \rangle$  and  $\langle 313 \rangle$ . No other crystallographic plane was observed on the sidewall tap. It can be concluded that integrating the sidewall taps into the singlemode v-groove waveguide is feasible.

## 5.2 Future Work

To obtain better waveguide quality, the most important future project is to solve the seam problem in the lower cladding layer. In Chapter 4, it was mentioned that the problem could be solved by fine-tuning the reflow process. An alternate approach may be to increase the diffusion length of the silane during the deposition. This could be done by replacing the silane gas source by a liquid source of silicon, which has larger molecules and possibly has a longer diffusion length. The major disadvantage of using the liquid source is that much longer deposition times are required.

The propagation loss of the RIE waveguide can be reduced by etching the polymer in a wet etchant. The resulting core surface should then be smoother. A KOH solution could be used for wet etching, but previous experiments showed that the etch rate is quite fast. Some experimentation would be required to discover the proper etching temperature to obtain an acceptable etch rate.

The optical coupling efficiency of the metallized end-facet might be increased by depositing the metal before putting on the lower cladding layer. Although the reflectivity of the metal might decrease significantly, the attempt is worthwhile. The second option might be to use gold for metallization although this might only improve the efficiency by less than 1 dB.

Another future investigation would be the fabrication of a singlemode v-groove

waveguide with integrated sidewall taps. A 3-dimensional beam propagation is required to simulate the tapping mechanism. The SFEM program used in this research can be modified to handle the 3-dimensional beam propagation problem. However, a huge amount of computing power is necessary to perform the required calculations.



## REFERENCES

- 1 L. B. Jeunhomme, Single-Mode Fiber Optics, Marcel Dekker, INC., 1983.
- 2 R. Narendra and J. N. McMullin, "Single-mode, Phosphorus-doped Silica Waveguides in Silicon V-grooves", IEEE Photonics Technology Letters, vol. 5, no. 1, pp. 43-46, Jan. 1993.
- 3 S. Kumar, R. I. MacDonald, and J. N. McMullin, "Low-loss multimode polymer waveguides with serial out-of-plane taps", Dig. Conf. Opt. Fiber Commun., 1992 OSA Tech. Dig., vol.5 (OSA, Washington, Dc, 1992), pp. 267.
- 4 Y. Backlund and L. Rosengren, "New shapes in <100> Si using KOH and EDP etches", Microelectronic Engineering, no.2, pp. 75-79, 1992.
- 5 E. Bassous, "Fabrication of Novel Three-Dimensional Microstructures by the Anisotropic Etching of <100> and <110> Silicon", IEEE Transaction Electron Device, vol. ED-25, no. 10, pp. 1178-1184, Oct. 1978.
- 6 E. Bassous and A. C. Lamberti, "Highly selective KOH-based etchant for boron-doped silicon structures", Microelectronic Engineering, no. 9, pp. 167-170, 1989.
- 7 K. Bean, "Anisotropic etching of Silicon", IEEE Transactions on Electron Devices, vol. ED-25, no. 10, pp. 1185-1193, 1978.
- 8 J. T. Boyd and S. Sriram, "Optical coupling from fibers to channel waveguides formed on silicon", Applied Optics, vol. 17, no. 6, pp. 895-898, March 1978.
- 9 C. R. Giles, E. Desurvire, "Modelling Erbium-Doped Fiber Amplifiers", Journal of Lightwave Technology, vol. 9, no. 2, Feb. 1991
- 10 W.T. Tsang, C. C. Tseng, and S. Wang, "Optical Waveguides Fabricated by Preferential Etching", Applied Optics, vol. 14, no. 5, pp.1200-1206, May 1975.
- 11 E. Snitzer, "Neodymium glass laser", Proc. 3rd Intl. Conf. Quantum Electron (Paris, France), pp. 999-1019, 1963.
- 12 C. J. Koester and E. Snitzer, "Amplification in a fiber laser", Applied Optics, vol.

- 3, pp. 1182-1186, 1964.
- 13 S. B. Poole, D. N. Payne, and M. E. Fermann, "Fabrication of low-loss optical fibres containing rare-earth ions", *Electronic Letters*, vol. 21, p. 737, 1985.
- 14 R. J. Mears, L. Reekie, I. M. Jauncey and D. N. Payne, "Low noise erbium-doped fibre amplifier operating at 1.54  $\mu\text{m}$ ", *Electronics Letters*, vol. 23, pp. 1026-1028, 1987.
- 15 G. Nykolak, P. C. Becker, J. Shmulovich, Y. H. Wong, D. J. DiGiovanni and A. J. Bruce, "Concentration-Dependent  $^4I_{13/2}$  Lifetimes in Er<sup>3+</sup>-Doped fibers and Er<sup>3+</sup>-Doped Planar Waveguides", *IEEE Photonics technology Letters*, vol. 5, no. 9, pp. 1014-1016, Sept. 1993.
- 16 W. J. Wang, S. I. Najafi, S. Honkanen, Q. He, C. Wu and J. Glinski, "Erbium-doped composite glass waveguide amplifier", *Electronics Letters*, vol. 28, no. 20, pp. 1872-1873, Sept. 1992.
- 17 K. Hattori, T. Kitagawa, M. Oguma, M. Wada, J. Temmyo and M. Horiguchi, "Erbium-doped silica-based planar waveguide amplifier pumped by 0.98  $\mu\text{m}$  laser diodes", *Electronics Letters*, vol. 29, no. 4, Feb. 1993
- 18 M. Federighi, I. Massarek and P. F. Trwoga, "Optical amplification in thin optical waveguides with high Er concentration", *IEEE Photonics Technology Letters*, vol. 5, no. 2, pp. 227-229, Feb. 1993.
- 19 G. Nykolak, M. Haner, P. C. Becker, J. Shmulovich and Y. H. Wong, "Systems evaluation of an Er<sup>3+</sup>-doped planar waveguide amplifier", *IEEE Photonics Technology Letters*, vol. 5, no. 10, Oct. 1993.
- 20 W. J. Miniscalco, "Erbium-doped glasses for fiber amplifiers at 1500 nm", *Journal of Lightwave Technology*, vol. 9, no. 2, pp. 234-249, Feb. 1991.
- 21 J. Shmulovich, A. Wong, Y. H. Wong, P. C. Becker, A. J. Bruce and R. Adar, "Er<sup>3+</sup> Glass waveguide amplifier at 1.5  $\mu\text{m}$  on silicon", *Electronics Letters*, vol. 28, no. 13, pp. 1181-1182, June 1992.

- 22 S. I. Najafi, S. Honkanen and W. J. Wang, "Composite Ion-Exchanged Glass Waveguides for Active Applications", The 2nd IEEE Intl. Workshop on Photonic, Networks, Components and Applications, March 1992.
- 23 E. Lallier, "Rare-earth-doped glass and  $\text{LiNbO}_3$  waveguide lasers and optical amplifiers", *Appl. Opt.*, vol. 31, no. 25, pp. 5276-5281, Sept. 1992.
- 24 M. Nakazawa and Y. Kimura, "Electron-beam vapour-deposited erbium-doped glass waveguide laser at  $1.53 \mu\text{m}$ ", *Electronics Letters*, vol. 28, no. 22, pp. 2054-2056, Oct. 1992.
- 25 K. Shuto, K. Hattori, T. Kitagawa, Y. Ohmori and M. Horiguchi, "Erbium-doped phosphosilicate glass waveguide amplifier fabricated by PECVD", *Electronics Letters*, vol. 29, no. 2, pp. 139-141, Jan. 1993.
- 26 K. J. Ebeling, Integrated Optoelectronics, Springer-Verlag Berlin Heidelberg, 1993.
- 27 M. Koshihara, H. Saitoh, M. Eguchi, K. Hirayama, "Simple scalar finite element approach to optical rib waveguides", *IEE Pro. J.*, vol139, no. 2, April 1992.
- 28 B. E. A. Saleh, M. C. Teich, Fundamentals of Photonics, A Wiley-Interscience Publication, John Wiley & Sons, INC., 1991.
- 29 A. A. M. Saleh, R. M. Jopson, J. D. Evankow and J. Aspell, "Modelling of Gain in Erbium-Doped fiber Amplifiers", *IEEE Photonics Technology Letters*, vol. 2, no. 10, pp. 714-716, Oct. 1990
- 30 F. D. Pasquale and M. Federighi, "Finite-Element Analysis of Single-Frequency Silica-Based  $\text{Er}^{3+}$ - $\text{Yb}^{3+}$  Co-Doped Waveguide Lasers", *IEEE Photonics Technology Letters*, vol. 7, no. 6, pp. 623-625, June 1995.
- 31 F. D. Pasquale and M. Zoboli, "Analysis of Erbium-Doped Waveguide Amplifiers by a Full-Vectorial Finite-Element Method", *Journal of Lightwave Technology*, vol. 11, no. 10, pp. 1565-1573, Oct. 1993.
- 32 F. D. Pasquale, M. Zoboli, M. Federighi and I. Massarek, "Finite-Element Mode-

- ling of Silica Waveguide Amplifiers with High Erbium Concentration", IEEE Journal of Quantum Electronics, vol. 30, no. 5, May 1994.
- 33 J. M. Jin, The finite element method in electromagnetics, New York: Wiley, 1993.
- 34 C. Y. Chen, R. R. Petrin, D. C. Yeh, and W. A. Sibley, "Concentration-dependence energy-transfer processes in  $\text{Er}^{3+}$  and  $\text{Tm}^{3+}$ -doped heavy-metal fluoride glass", Optics Letters, vol. 14, no. 9, pp. 432-434, May 1989.
- 35 W. Q. Shi, M. Bass, and M. Birnbaum, "Effects of energy transfer among  $\text{Er}^{3+}$  ions on the fluorescence decay and lasing properties of heavily doped  $\text{Er}:\text{Y}_3\text{Al}_5\text{O}_{12}$ ", Journal of Optics Society America B, vol. 7, no. 8, pp. 1456-1462, August 1990.
- 36 N. Rajeshree, Phosphorus-Doped Glass Waveguides on Silicon Substrates, Master of Science Thesis, Department of Electrical Engineering, University of Alberta, 1992.
- 37 K. J. MacLeod, Micromachined Serial Taps in Si Waveguides, Master of Science Thesis, Department of Electrical Engineering, University of Alberta, 1995.
- 38 B. Block and M. Sierakowsky, "The Use of a Certain Fluorocarbon Surfactant and Fluorocarbon Conformal Coating Improves KOH Silicon Etching Quality", Micromachining and Micropackaging of Transducers, Ed. by C. D. Fung, P. w. Cheung, W. H. Ko, and D. G. Fleming, Elsevier Science Publishing Company, pp. 125-133, 1985.
- 39 S. Kumar, Polymer Waveguides with Taps, Master of Science Thesis, Department of Electrical Engineering, University of Alberta, 1992.
- 40 M. Fei, Micromachined Center Taps for Silicon V-groove, Master of Science Thesis, Department of Electrical Engineering, University of Alberta, 1993.
- 41 Y. Jaluria, Computer Methods for Engineering, Allyn and Bacon, Inc., 1988.
- 42 N. A. Olsson, "Lightwave Systmes With Optical Amplifiers", Journal of Lightwave Technology, vol. 7, no. 7, July 1989

**43 Jim Broughton, AMC, private communication**

## APPENDIX A Description of the SFEM Program

The main program for the SFEM calculation is called `vcupdate.c`. It is written in standard C language. It can be compiled by both `'cc'` and `'gcc'`. The program reads the required parameters from an input file called `'Vinput.dat'`. A sample of the input file is shown below.

<b>0.632e-6</b>	<b>wavelength</b>
<b>2.0e-5</b>	<b>height_of_the_substrate</b>
<b>6.9e-6</b>	<b>height_of_the_cladding</b>
<b>3.0e-6</b>	<b>height_of_the_core</b>
<b>3.8e-6</b>	<b>distance_between_core_and_cladding</b>
<b>6.0e-6</b>	<b>covering_layer</b>
<b>3.5</b>	<b>substrate_index</b>
<b>1.44</b>	<b>lower_cladding_index</b>
<b>1.44</b>	<b>upper_cladding_index</b>
<b>1.54</b>	<b>core_index</b>
<b>1.56</b>	<b>erbium_index</b>
<b>6</b>	<b>core_divide_layer</b>
<b>1</b>	<b>starting_layer_of_erbium</b>
<b>6</b>	<b>ending_layer_of_erbium</b>
<b>4</b>	<b>dope_format</b>
<b>1</b>	<b>fill_layer</b>
<b>0.2e-6</b>	<b>erbium_thickness</b>
<b>0.1e-6</b>	<b>overflow</b>
<b>10.0</b>	<b>curve</b>

The definitions of some of the above parameters are graphically illustrated in Fig.

- A.1. The parameter `'core_divide_layer'` specifies the number of equally-spaced layers that the core is to be divided into. Usually, this parameter is set at 6 and the core is divided into 72 elements in 6 equally-spaced layers. A smaller core size may require more layers in order to find the mode. The `starting_ and ending_ layer_of_erbium` specifies which core layers are to be filled with erbium. The numbering of the layers starts at the bottom of the v-groove. These two parameters are used to simulate Waveguide B mentioned in Chapter 2. The parameter `'dope_format'` specifies which type of waveguide structure is to be cal-

culated. The waveguide structures are specified as follows,

1. Waveguide A or B, depends on how many layers are filled with erbium.
2. Waveguide D
3. Waveguide C
4. This is used to simulate the overflow condition for polymer waveguide.

Since the core is divided into a specified number of layers, the thickness of the erbium layer for waveguide C and D can only be specified in terms of number of layers. The number of erbium-filled layers is specified in the parameter 'fill\_layer'. The overflow layer of the polymer waveguide can be arbitrarily specified by the parameter 'overflow'. When the overflow condition is to be simulated, the parameter 'fill-layer' must be set to 1. The last parameter 'curve' specifies the curvature of the crescent on the core surface. The value corresponds to the ratio between the core height and the depth of the crescent.

The program starts by computing the overall dimensions of the problem domain, and the required coordinates in different regions, from the input parameters. Then the program divides the problem domain into finite elements. The vertices of the triangular elements form the grid points of the entire mesh. Each vertex is given a particular number and the number is usually called the global number. The assignment of the global numbers to the vertices are arbitrary. Two vertices of an element are not required to be numbered consecutively. The global numbers of the three vertices of each element are stored in a matrix called NI. The matrix has  $N \times 3$  dimensions, and N corresponds to the number of finite elements. It does not matter which vertex is assigned to which one of the 3 columns of the matrix, as long as the global number is stored in the matrix consistently in either a clockwise or counter-clockwise fashion. The coordinates of the vertices are stored in two

different matrices. The first matrix is called 'coord', which stores the vertices according to the N1 matrix; the matrix has 6 X N dimensions (3 pairs of (x,y)). The second matrix stores the coords of the vertices according to the ascending order of the global numbers; therefore the matrix has 2 X N1 dimensions, and N1 corresponds to the number of total vertices. The refractive index of each element is stored in a vector called INDEX. Once all these matrices are ready, the program then calculates the A and B matrices mentioned in Chapter 2. The derivation of the approximated equations for forming the A and B matrix is found in [33]. Since the subroutine for solving the eigenvalues and eigenvectors is written in Fortran, the A and B matrices and other related matrices are exported to files in order to be read by the Fortran program, and this is the final task of the program. The names of the files are identical to the names of the matrices. Some other useful parameters are exported to a file called 'counter'. In order to view how the problem domain is divided into finite elements, a MATLAB called 'di.m' is used.

The Fortran eigenvalue solver is called 'rsg'. It is compiled using standard Fortran 77 (f77). The program reads in all the required matrices and performs the eigenvalue solving. The desired eigenvalues are then selected and exported to a file called 'eigen', and the corresponding eigenvectors are stored in a file called 'evector'.

The calculated mode fields can be viewed graphically in MATLAB by running a script called 'out1.m'. To calculate the confinement factor of the calculated mode field, another MATLAB script was written: 'conf.m'. The script is written only for singlemode calculation. The script reads in the values from 'evector' and performs the calculation.

It should be kept in mind that since this SFEM program deals with 5 different configurations, there would be some cases in which the program divides the problem



domain incorrectly. To ensure that proper division is obtained, the user is advised to view the resulting mesh using 'di.m' before beginning to solve.

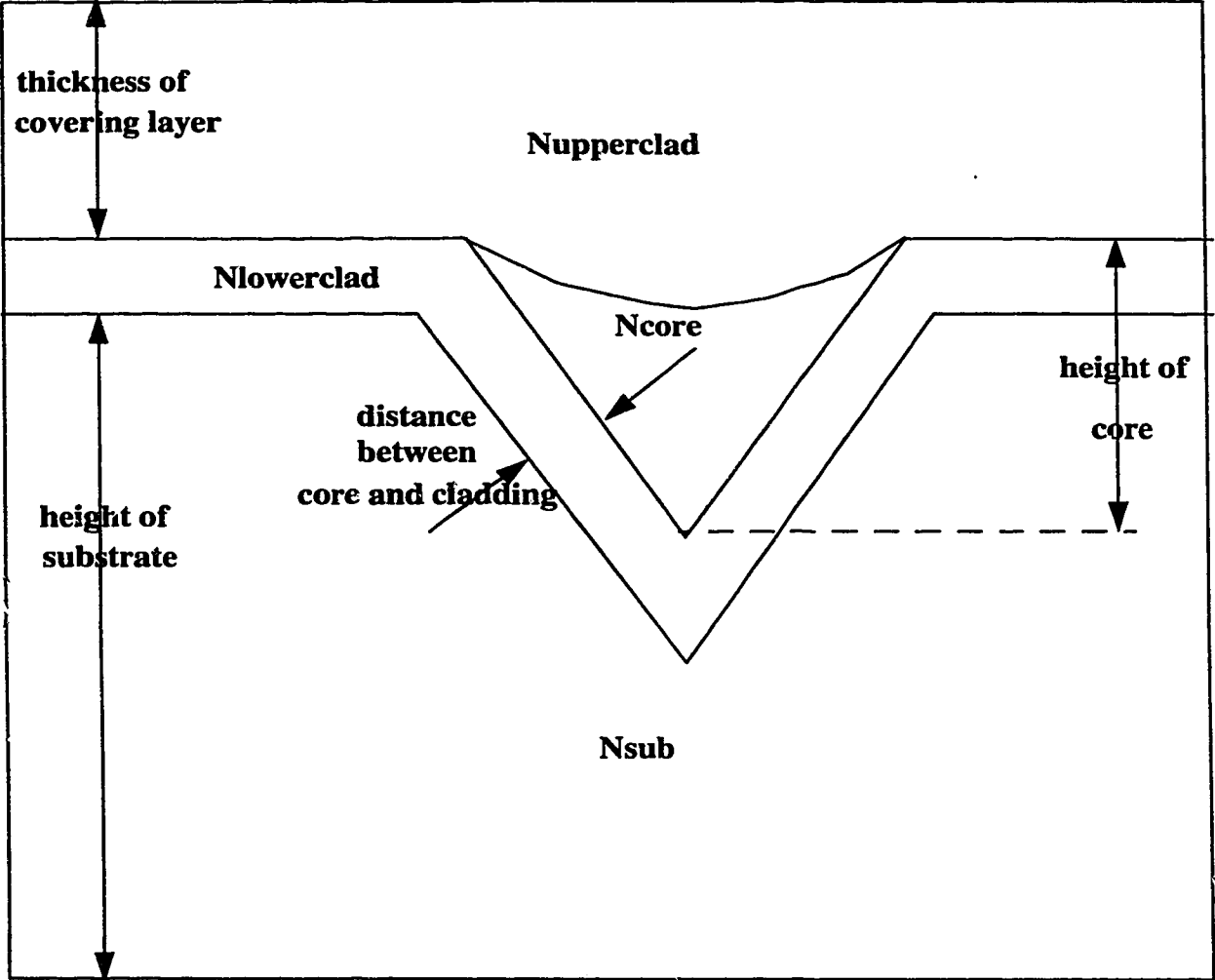


**Fig. A.1 Schematic Diagram of a V-groove Waveguide**

## APPENDIX B Amplifier Gain Simulation Program

The amplifier simulation program is called 'prop.c'. The program begins by reading in the required parameters. The parameters are stored in a file called 'Input.dat'. A sample of the file is shown below.

<b>3.0e26</b>	<b>Erbium_Concentration</b>
<b>90.0</b>	<b>A21</b>
<b>1.0e9</b>	<b>A32</b>
<b>1.0e9</b>	<b>A43</b>
<b>5.0e-23</b>	<b>Cup</b>
<b>5.0e-23</b>	<b>C3</b>
<b>3.5e-23</b>	<b>C14</b>
<b>2.58e-25</b>	<b>Sigma13</b>
<b>5.41e-25</b>	<b>Sigma21</b>
<b>5.36e-25</b>	<b>Sigma12</b>
<b>1.0e-6</b>	<b>Ps</b>
<b>100.0e-3</b>	<b>Pp</b>
<b>100.0e-6</b>	<b>deltaz</b>
<b>400</b>	<b>step</b>
<b>1.0e-6</b>	<b>posbound</b>
<b>1.0e-11</b>	<b>negbound</b>
<b>1.0e-22</b>	<b>toll</b>

The second to tenth parameters correspond to the parameters in the four-energy-level model described in Chapter 3. 'Ps' and 'Pp' are the input signal and pump power. 'deltaz' specifies the simulation step size in the propagation direction and the unit is in metre. 'step' specifies the number of step to be calculated. The length of the waveguide is thus equal to 'deltaz' multiplied by 'step'. The last three parameters are used for searching the correct  $P_{ase}$ - values, more details are discussed later.

After receiving these parameters, the program imports three matrices, 'coord', 'NI', and 'Index' generated from the modal analysis. 'coord' is used for calculating the area of each finite element. 'NI' is used for calculating the field intensity at both signal and pump wavelengths. 'Index' tells the program which elements are doped with erbium.

The input mode field at the two wavelengths are read in from two files, 'evectors' and 'evectorp'. The 'rsg' program only generates the 'evector' file; therefore the user is required to run the mode-solver program twice for both signal and pump wavelengths and copy the 'evector' file into the two files separately.

After all required information is imported, the program then calculates the area of each finite element and the normalized intensity. The intensity of the element is calculated by squaring the average of the mode field values at the three vertices. The normalized intensity of each element is obtained by dividing the power of the element by the product of the total power and the area of the element.

The simulation program calculates the output power of the signal and pump, as well as the P<sub>ase</sub> spectrum. In order to satisfy the boundary condition (3.11), the program uses the bisection method to pin-point the correct value of each P<sub>ase</sub>-(0,v<sub>j</sub>) frequency slot. The parameters, 'posbound' and 'negbound', specify the upper and lower boundaries used in the bisection method. At the first iteration, 'posbound' is assigned to each P<sub>ase</sub>-(0,v<sub>j</sub>) slot. The simulation begins by first solving the rate equations of each finite element at the input end using Newton-Raphson method. After obtaining the ion population densities in different energy levels, the program calculates the absorption and emission coefficients using (3.12)-(3.14). Then, the program calculates the signal power, pump power and P<sub>ase</sub> spectrum for the next step using the 4<sup>th</sup> order Runge-Kutta method according to (3.6)-(3.8). The program then repeats the same calculation procedures for each successive step. At the end of the first iteration, the program obtains the output signal and pump power, and the P<sub>ase</sub> spectrum. The program then examines the P<sub>ase</sub>- values at the output end. If the sum of the square of the P<sub>ase</sub>-(L,v<sub>j</sub>) is larger than 'tol1', the program proceeds to the

next iteration. The new  $P_{ase-(0,v_j)}$  values are the average of the posbound's and negbound's. These two boundary values are updated at the end of each iteration. The simulation ends when the boundary condition is satisfied.

The program outputs the final results into two files. The file 'temp' stores the propagation distance, pump power, signal power,  $\gamma_{13}$ ,  $\gamma_{12}$  and  $\gamma_{21}$  in 6 columns. The file 'Pase' stores the  $P_{ase+(L,v_j)}$  and  $P_{ase-(0,v_j)}$  in the first and second columns. The length of the columns is equal to the number of frequency slots, in this version the number of slots is equal to 64.

## **APPENDIX C Procedures for etching V-grooves**

The following steps describe the procedures for etching v-grooves in <100> oriented silicon wafers.

### **1. Thermal Oxidation**

3" bare silicon wafers are placed in a furnace. The furnace is then heated to 1100 °C. Nitrogen is bubbled through a flask of deionized water heated to 92 °C. After 75 minutes, the wafers are taken out of the furnace and are rotated 180 °C to improve the uniformity of the growth. The wafers are then inserted placed back into the furnace for another 75 minutes of oxidation. This process yields about 0.6 μm of oxide on the wafers.

### **2. Vapour Prime**

The wafers are primed with HMDS in the YES oven to improve the adhesion of the photoresist to the oxide. The step takes about 45 minutes.

### **3. Photoresist Spin-On**

The wafers are coated with Shipley HP504 positive photoresist. A sufficient amount of photoresist is poured on the wafers, then the wafers are spun for 5 seconds at 500 RPM to spread the resist, and 17 seconds at 3500 RPM to obtain a 1.5 μm resist layer.

### **4. Photoresist Softbake**

The coated wafers are softbaked for one minute on a 110 °C vacuum-applied hot plate for 50 seconds, followed by 10 seconds of nitrogen backfill.

### **5. Mask Alignment and Exposure**

The wafer is then placed in the Suss mask aligner. The alignment marks on the pho-

tomask are lined up with the wafer flat. The photoresist is then exposed for approximately 3.5 seconds to UV light shining through the mask.

## **6. Photoresist Development**

The exposed photoresist is developed using Shipley 354 developer. The entire development cycle involves a 5 second deionized water pre-wet, a 60 seconds of developer spray, a 90 second rinse and a 30 second spin-dry.

## **7. Hardbake**

The developed wafers are hardbaked on a 120 °C vacuum-applied hot plate to harden the remaining photoresist.

## **8. Oxide Etch**

The exposed silicon dioxide under the masking layer is etched away by a 10:1 BOE at room temperature. The etch rate is about 0.05  $\mu\text{m}/\text{min}$ .

## **9. KOH Etch**

The photoresist is removed using acetone. The patterned wafers are then immersed into a 76 °C KOH+IPA solution. The etch rate is about 0.6  $\mu\text{m}/\text{min}$ .

## APPENDIX D Borophosphorus Silicon Glass (BPSG)

The recipe for the growing BPSG in LPCVD is as follows

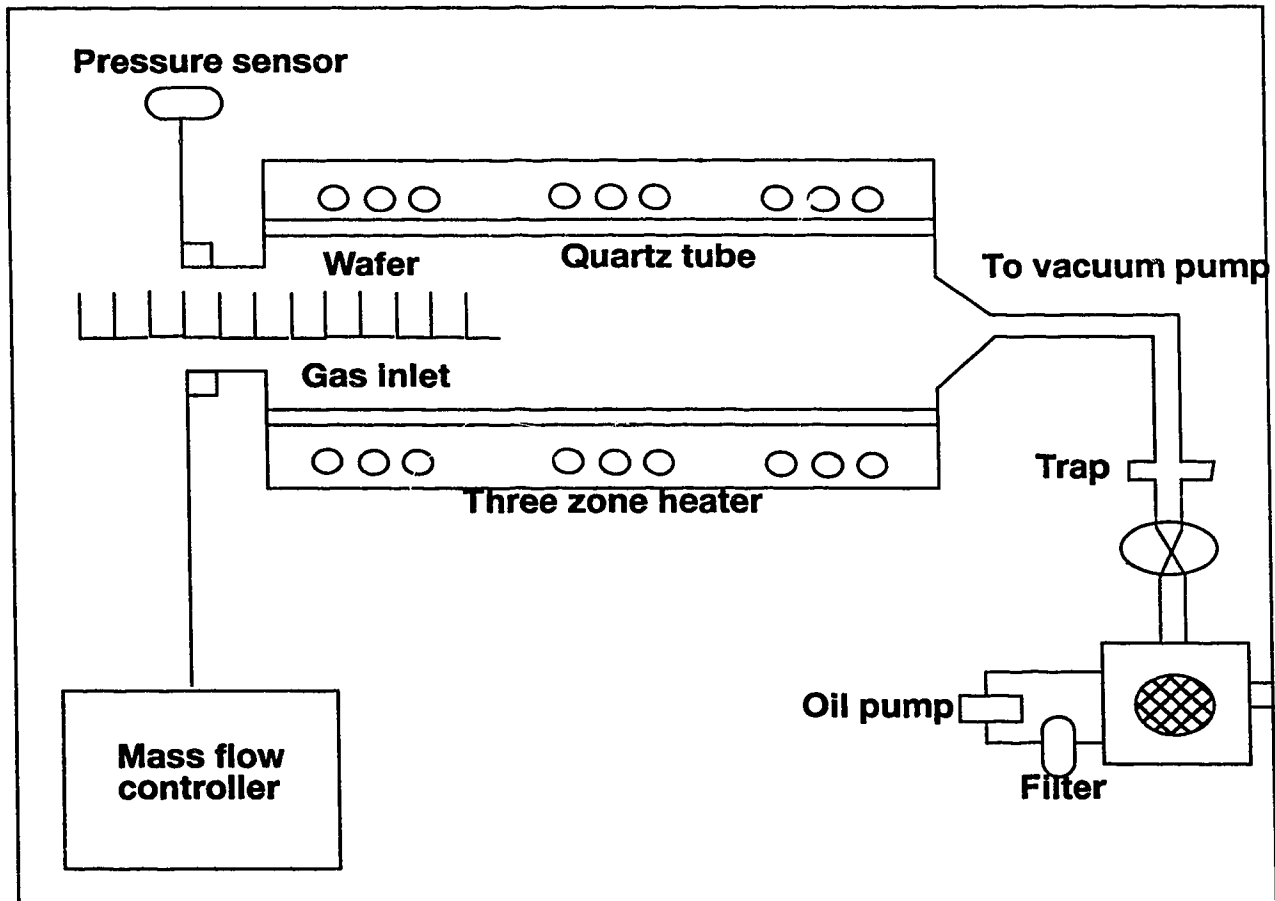
### The flow rates for BPSG:

SiH <sub>4</sub>	30 sccm
O <sub>2</sub>	45 sccm
TMP	5 sccm
TMB	5 sccm

**Pressure:** 250 mTorr

**Temperature:** 410 °C

The schematic diagram of the LPCVD device is shown below



## **APPENDIX E Procedures for Direct E-beam Writing**

1. 3" silicon wafers with a 0.1  $\mu\text{m}$  layer of thermal oxide are coated with a 0.6  $\mu\text{m}$  layer of PMMA. The PMMA is diluted with chlorobenzene in 2:1 ratio. The diluted PMMA has 5% concentration. The wafers are spun for 10 seconds at 100 RPM for spreading, and 30 seconds at 5000 RPM.
2. The wafers are hard-bake in an oven for 1 hour at 150  $^{\circ}\text{C}$
3. The wafers are soft-bake in vacuum for 1 minute at 150  $^{\circ}\text{C}$
4. The wafers are cleaved into small pieces (about 1cm x 1cm)
5. The small pieces of wafer are put inside the scanning electronic microscope (SEM) for e-beam writing. The e-beam dose is 170  $\mu\text{C}/\text{cm}^2$
6. The exposed wafer pieces are developed first in MIBK for 60 seconds, then 20 seconds in IPA, follows by 20 seconds in deionized water
7. The pieces are dry-etched in the RIE machine for 3.5 minutes. The gas composition is 80%  $\text{CHF}_3$ , 5%  $\text{O}_2$  and 15%  $\text{N}_2$ . The etch rate for PMMA and  $\text{SiO}_2$  are 1000  $\text{\AA}/\text{min}$  and 450  $\text{\AA}/\text{min}$  respectively.
8. The PMMA on the wafer pieces is stripped off using acetone
9. The pieces are etched in a 30% KOH + IPA solution for 15 min at 76  $^{\circ}\text{C}$ .
10. The thermal oxide on the pieces is stripped off using BOE